8-13-2020 11:30 AM

Galvanic Corrosion of Carbon Steel-Stainless Steel Welds

Mi Li, *The University of Western Ontario*

Supervisor: Wren, Jungsook Clara, *The University of Western Ontario*

A thesis submitted in partial fulfillment of the requirements for the Doctor of Philosophy degree in Chemistry

Recommended Citation
Li, Mi, "Galvanic Corrosion of Carbon Steel-Stainless Steel Welds" (2020). *Electronic Thesis and Dissertation Repository*. 7162.
https://ir.lib.uwo.ca/etd/7162

Abstract

A water leak in one of the Canada Deuterium Uranium (CANDU) nuclear reactors could lead to galvanic corrosion between the materials of its supporting structures: carbon steel (CS) and stainless steel (SS). This project investigates the effects of physical and chemical solution parameters on the corrosion of galvanically coupled dissimilar CS-SS welds, with the aim of developing a corrosion dynamics model that can be used to assess the long-term integrity of the CANDU reactor structural materials with confidence. The studied parameters were solution pH, temperature, the presence or absence of γ-radiation and the cathode:anode surface area ratio. Multiple electrochemical techniques were used to measure the corrosion rates of these steels, including the novel Dual-Electrochemical Cell method. These were augmented with post-test surface and solution analyses to study the oxides formed on the corroded surfaces and to determine the amount of dissolved metal ions in the solution.

This study demonstrated that CS and SS corrosion involve many elementary steps that lead to the dissolution of metal ions as well as the formation and growth of different oxides. Non-linear dynamic behaviours can develop due to the strong coupling between different elementary processes. Therefore, simple linear-dynamic rate models for the corrosion of CS or a CS-SS couple can result in erroneous evaluations and inaccurate predictions of their long-term performance.

The results also showed that the effects of galvanic coupling to SS, higher temperature, higher cathode:anode surface area ratio or γ-irradiation on the corrosion progression of CS have a strong time-dependence. Initially, they increase the corrosion rate of CS. However, these factors also lead to faster oxide formation and growth on CS, suppressing subsequent Fe dissolution over longer time periods. As a result, the increase in the CS corrosion rate due to galvanic coupling diminishes with time.

Keywords: Carbon Steel, Stainless Steel, Galvanic Corrosion, Corrosion Dynamics, Electrochemistry, Water Radiolysis

Summary for Lay Audience

A water leak in a Canada Deuterium Uranium (CANDU) nuclear reactor could lead to galvanic corrosion between the materials of its supporting structures: carbon steel (CS) and stainless steel (SS). When galvanically (electrically) connected to SS, accelerated corrosion of CS is possible, possibly affecting the long-term integrity of the reactor. Therefore, careful evaluation of potential corrosion damage to SS, and especially to CS, is needed.

In this project, the effects of solution pH, temperature, the presence or absence of γ-radiation and the cathode:anode surface area ratio on the progression of the corrosion of steels were investigated. Electrochemical techniques, augmented with post-test surface and solution analyses, were used to measure the corrosion rates of these steels, to study the oxides formed on their corroded surfaces and to determine the amount of dissolved metal ions in the solution.

The results showed that coupling to SS, higher temperatures, higher cathode:anode surface area ratio or the presence of γ-radiation increase the initial corrosion rate of CS. However, these factors also lead to much faster oxide formation and growth on CS, which suppresses subsequent corrosion over longer time periods. As a result, the increase in the CS corrosion rate caused by galvanic coupling diminishes with time.

Co-Authorship Statement

This thesis includes published data in Chapter 4, 5 and 6.

For all the chapters, Dr. J.C. Wren, G. Whitaker and Dr. J.M. Joseph helped with editing. Dr. J.M. Joseph also helped with all the post-test solution analysis presented in the thesis.

Chapter 4: Dr. M. Momeni helped with the design of the experiments and post-test surface analysis.

Chapter 5: Dr. D. Guo helped with the experimental set-up and post-test surface analysis.

Chapter 6: Dr. D. Guo helped with the experimental set-up.

Acknowledgements

There are many people to whom I would like to express my sincere gratitude for their contributions to my time in graduate school.

I would like to thank my supervisor, Dr. J. Clara Wren for her support and guidance during this project. Without her guidance and assistance, the completion of this thesis would not be possible. From her, I have also learned to be critical about science, be passionate about work, and be nice to people. It has been a great honor to be her student.

I would like to thank Dr. Jiju Joseph for all her support and encouragement throughout my time at Western. She was always there providing me with helpful advice on both work and life.

I would like to thank Giles Whitaker for assisting me in improving my writing and presentation skills, and for editing my manuscripts and thesis.

I would like to thank my labmates, the whole Wren group members who have contributed significantly to my time here at Western. I sincerely appreciate their valuable friendships and feel grateful for being one of this group.

I would like to thank my family for all their love, care and support.

I am truly grateful for being cared for by so many amazing people. Thank you everyone for making my journey enjoyable!

Table of Contents

List of Symbols

A	Surface area
b	Tafel slope
b_{a}	Anodic Tafel slope
b_{c}	Cathodic Tafel slope
E	Electrode potential
E_{appl}	Applied potential
E_{corr}	Corrosion potential
E_{cpl}	Coupling potential
E_{eq}	Equilibrium potential
E_{initial}	Initial potential
E_{switch}	Switching potential
F	Faraday constant
i	Current density
i_{a}	Anodic current density
i_{c}	Cathodic current density
i_{corr}	Corrosion current
$i_{\mathrm{corr-CS\ ind}}$	Corrosion current of CS during its independent corrosion
$i_{\mathrm{corr-CS\ cpl}}$	Corrosion current of CS during its galvanic corrosion
I_{cpl}	Coupling current
i_{cpl}	Coupling current density (normalized to CS surface area)
$i_{\mathrm{cpl-SS}}$	Coupling current density (normalized to SS surface area)
i_{meas}	Measured polarization current
i_{trans}	limiting current
i_0	Exchange current density
Q	Accumulated charge
R	Ideal gas constant
R_{p}	Charge transfer resistance
R_{s}	Solution resistance

t	Time
T	Temperature
z	Number of electrons

α	Charge transfer coefficient
ΔG	Gibbs free energy of reaction
γ	Galvanic effect
γ_{Q}	Galvanic effect calculated from charge
γ_{S}	Galvanic effect calculated from dissolved ions
η	Overpotential

List of Acronyms

AISI	American Iron and Steel Institute
BCC	Body-centred cubic
CANDU	Canada Deuterium Uranium
CE	Counter electrode
CS	Carbon steel
CS-SS	Carbon steel and stainless steel couple
CV	Cyclic voltammetry
DEC	Dual-electrochemical-cell
ESC	End Shield Cooling
FCC	Face-centred cubic
FIB	Focused ion beam
HAZ	Heat-affected zone
HER	Hydrogen evolution reaction
ICP	Inductively coupled plasma
ICP-OES	Inductively coupled plasma optical emission spectrometry
LET	Linear energy transfer
LPR	Linear polarization resistance
OPG	Ontario Power Generation
ORR	Oxygen reduction reaction
PD	Potentiodynamic polarization
PWR	Pressurized water reactor
RDS	Rate-determining step
RE	Reference electrode
SCC	Stress corrosion cracking
SCE	Saturated calomel electrode
SEM	Scanning electron microscopy
SHE	Standard hydrogen electrode
SS	Stainless steel
SS 304	Stainless steel (Type 304)

SS 309	Stainless steel (Type 309)
WE	Working electrode
ZRA	Zero resistance ammeter

List of Tables

List of Figures

This page is intentionally left blank.

Chapter 1. Introduction

1.1 Thesis Motivation

Nuclear power is part of a low-carbon-emitting energy strategy in many countries [1]. In Canada, CANDU (Canada Deuterium Uranium) reactors provide about 15% of Canada’s and nearly 60% of Ontario’s electricity supply [2].

As nuclear power reactors age and their life-times are extended, accurate assessment of the long-term integrity of the reactor structural materials is increasingly important. For example, a current investigation into a leak in the End Shield Cooling (ESC) System in the Pickering Unit 6 nuclear reactor has raised a potential issue. Moisture from the ESC system leak could possibly reach a location in the annular air gap which exists around the periphery of the Calandria tank assembly and its supporting structures. Corrosion in this region would be problematic and needs careful evaluation. In particular, the potential for accelerated (galvanic) corrosion attack on carbon steel (CS) adjacent to the dissimilar metal weld (stainless steel, type 309) between CS (SA36) and stainless steel (SS) (Type 304L) at the periphery of the annular air gap must be addressed (shown in Figure 1.1).

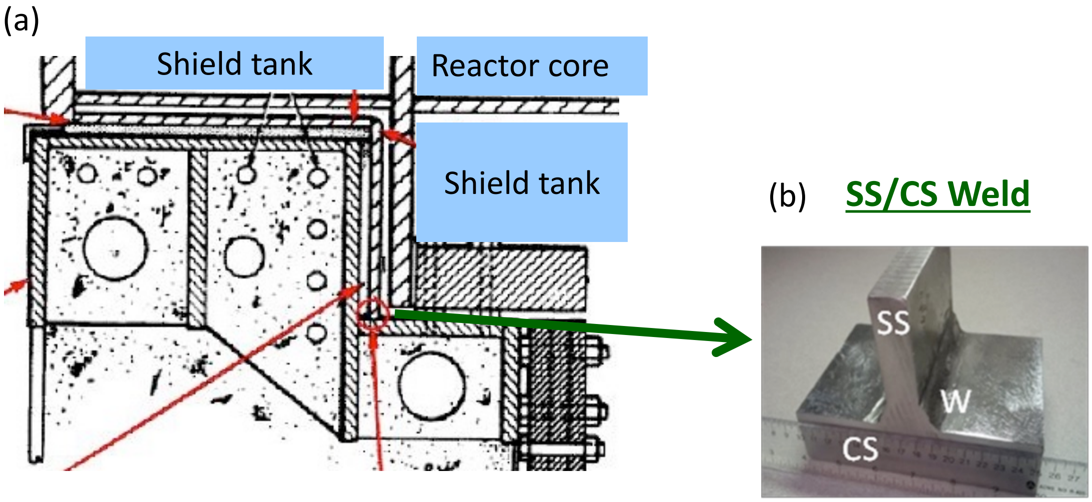

Figure 1.1 (a) Schematic of the calandria tank assembly and its supporting structures in a CANDU reactor. The red circle indicates the location of the carbon steel (CS) and stainless steel (SS) weld joint (b) a SS-CS weld block supplied by Ontario Power Generation (OPG).

The corrosion kinetics of an alloy depend not only on its metallurgical properties, but also on the redox and electrolyte properties of water in contact with the alloy. These properties can change considerably depending on the concentration of redox active species present, pH, and temperature. The annular air gap accessibility is very limited and the actual solution environment at the weld region is consequently not known. Therefore, it is necessary to make certain assumptions about the solution environment at the weld region. The pH of the ESC water is 10.4, but the pH of water condensed on the weld region could be different. The annular gap environment includes the added complication of ionizing radiation that will drive radiolysis of liquid water and humid air as shown in Figure 1.2. Radiolysis affects the redox conditions by decomposing water to create redox active species such as H_2O_2, which can significantly affect the oxidation rates of metals.

Radiolysis of humid air produces nitric oxides and nitric acid which are easily absorbed into water in contact with the humid air, lowering the pH. Since these radiolysis products can affect corrosion kinetics considerably, evaluating materials performance and the design of chemistry control systems to limit corrosion in nuclear environments must consider the effect of radiation fields that are present (particularly γ-radiation) on water chemistry.

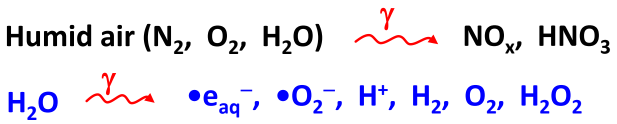

Figure 1.2 Humid air and water radiolysis reaction.

Assessing the effects of water chemistry on corrosion is difficult even in the absence of radiation. The difficulty arises primarily because corrosion kinetics is already a complicated function of the chemical and physical properties of a solution in contact with metal, and the solution properties can change considerably as corrosion progresses. CS corrosion in various environments has been studied extensively over the last few decades due to the wide range of applications of this material. However, there is no consensus on the effect of each environmental factor, and especially the effect of radiation.

Corrosion consists of many elementary processes including electrochemical oxidation of metal, solution reactions, transport of metal cations, and oxide formation and growth. These complex processes make long-term corrosion predictions challenging even in the absence of radiation. Currently, most research addresses the long-term (galvanic) corrosion rate of metals by linear extrapolation of short duration experiments such as metal weight loss and polarization tests. This is based on the assumption that the corrosion rates of metals remain constant over time. However, strong feedback between different elementary processes could occur, resulting in nonlinear changes in rate over time. Therefore, a simple linear dynamic model could lead to erroneous interpretations of experimental results and consequently incorrect long-term predicted corrosion rates. To develop a high-fidelity model, it is critical to decouple the elementary processes involved in corrosion. Therefore, systematic studies on how each parameter affects the individual elementary processes are required.

1.2 Research Objective and Approaches

The objective of this thesis project is to develop a mechanistic understanding of the aqueous corrosion of the different steels used in the shield tank assembly and supporting structures in the presence of a continuous flux of γ-radiation. The corrosion dynamics of galvanically coupled CS-SS in solution environments that are relevant to those anticipated at the annular air gap were investigated to address the possible consequences of the leak on the long-term integrity of the weld region. The results of this work will also improve the current mechanistic understanding of galvanic corrosion which will aid in the understanding and prediction of corrosion in a variety of industrial contexts. The long-term goal of this continuing project is to develop a high-fidelity corrosion dynamic model of the independent and galvanically coupled corrosion of steels. This model will allow the long-term integrity of the CANDU nuclear reactor structural materials to be assessed with confidence, and will also be able predict the extent of galvanic corrosion of CS and SS in other applications.

The solution parameters explored in this project are pH, temperature, the cathode to anode surface area ratio and the presence or absence of γ-radiation. Electrochemical techniques were used to follow the independent and galvanically coupled corrosion dynamics of CS and SS. For the independent corrosion studies, corrosion potential (E_{corr}) measurements and polarization tests were performed. Both conventional techniques and non-standard technique developed specifically for this project were used for the polarization tests. For the galvanic corrosion studies, coupling potential, coupling current measurements and the non-standard techniques were used. The electrochemical tests were augmented by post-test surface and solution analyses. The surface analysis techniques used were optical microscopy, scanning electron microscopy (SEM) and Raman spectroscopy. The solutions were analyzed for dissolved iron concentration using inductively coupled plasma optical emission spectroscopy (ICP-OES).

1.3 Thesis Outline

The first three chapters provide an introduction and background information: the motivation and objectives in Chapter 1, literature review and technical background in Chapter 2, and the experimental techniques employed in Chapter 3.

The next five chapters report the specific studies carried out.

Chapter 4: In this chapter the effect of solution properties (solution pH and temperature) on the independent corrosion of individual carbon steel (CS Type SA36), stainless steel (SS 304) and the filler material, stainless steel (SS 309) was investigated. A series of electrochemical tests (corrosion potential (E_{corr}), Linear Polarization Resistance (LPR) and Potentiodynamic Polarization (PD)) were performed. The dual-electrochemical cell (DEC) method for measuring corrosion rate was introduced. The current results were also compared with the solution and surface analyses.

Chapter 5: In this chapter the galvanic corrosion of carbon steel (CS) and stainless steel (SS 309) was investigated in different aqueous environments. The corrosion currents of CS after galvanic coupling to SS were measured using both conventional methods and the DEC method. The galvanic effect at different temperatures is addressed in this chapter.

Chapter 6: In this chapter the effect of radiation on the galvanic corrosion of carbon steel (CS) and stainless steel (SS 309) was investigated by studying the corrosion behaviors of individual alloys and galvanically coupled CS-SS in aqueous solutions. A combination of coupon immersion tests and electrochemical experiments was performed. This was augmented by post-test analyses of solution and surface.

Chapter 7: In this chapter the effect of cathode to anode surface area ratio on the galvanic corrosion of carbon steel (CS) and stainless steel (SS 309) in different aqueous environments was investigated.

Chapter 8: In this chapter the summary, overall conclusions and future work of the thesis project are presented.

1.4 References

[1] F. Cattant, D. Crusset, D. Féron, Mater. Today, 11 (2008) 32–37.

[2] The Canadian Nuclear Association, The Canadian Nuclear Factbook, 2020.

Chapter 2. Technical Background and Literature Review

2.1 Carbon Steel and Stainless Steel

2.1.1 Microstructure of carbon steel

Carbon steels are a type of Fe-based alloy, with carbon as the alloying element. Pure iron exhibits a body-centered cubic (BCC) structure at room temperature known as *ferrite*, or α-Fe. The solubility of carbon in α-Fe is less than 0.022wt%. Therefore, only a small amount of carbon can form a solid solution with α-Fe. In carbon steels the carbon is predominantly in the form of the intermetallic compound iron carbide (Fe_3C), also known as *cementite*. The carbon content in cementite is 6.70 wt%. Ferrite and cementite form a eutectoid structure called *pearlite*, which consists of alternating ferrite and cementite layers. The carbon content in pearlite is 0.76 wt%. The Fe- Fe_3C phase diagram is shown in Figure 2.1. The metallurgical structure of CS consists of a pure α-Fe phase and a pearlite phase. An example of the surface morphology of CS after etching, obtained using scanning electron microscopy (SEM), is shown in Figure 2.2.

Some other alloying elements such as nickel, chromium and molybdenum can be added to the steels to optimize their mechanical properties and reduce their corrosion rates under certain service conditions [1]. These types of steels are known as alloy steels. Whether a steel is categorized as carbon steel or alloy steel is determined by the amounts of alloying elements other than carbon. According to the American Iron and Steel Institute (AISI) definition, steel is considered to be carbon steel if no minimum content is specified or required for chromium, cobalt, niobium, molybdenum, nickel, titanium, tungsten, vanadium or zirconium, or any other element, when the specified minimum for copper is below 0.40 wt%, or when the amounts of added manganese, silicon and copper are limited to 1.65 wt%, 0.60 wt% and 0.60 wt%, respectively.

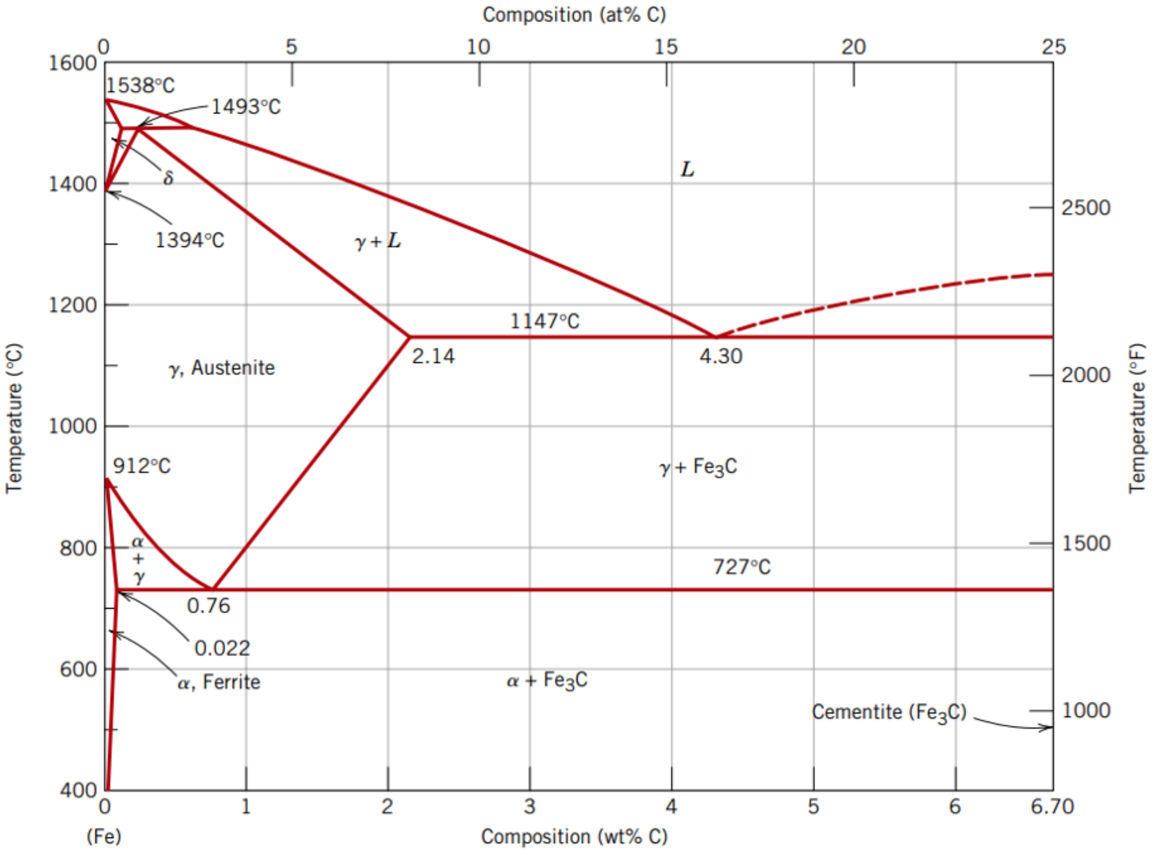

Figure 2.1 The Fe–Fe_3C phase diagram [2].

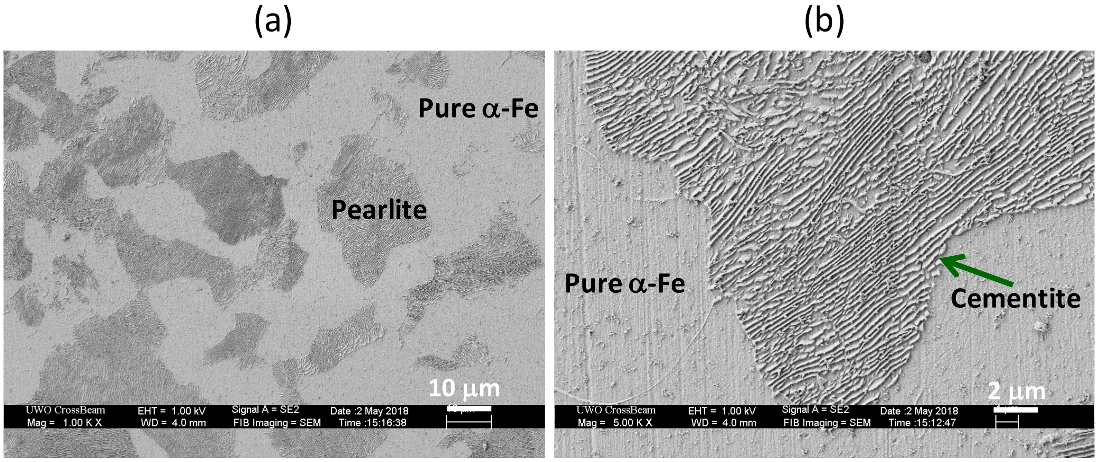

Figure 2.2 An illustration of the microstructure of CS with relatively (a) low and (b) high magnification using SEM.

2.1.2 Microstructure of stainless steel

Stainless steels are a type of Fe-based alloy with high corrosion resistance. The predominant alloying element is Cr (> 11 wt%). The corrosion resistance of stainless steel is due to the presence of a protective Cr_2O_3 layer on the surface. Additions of alloying elements with high concentrations leads to a dramatic alteration in the Fe–Fe_3C phase diagram shown in Figure 2.1. Therefore, stainless steel can have various microstructures depending on its composition. Based on the phase constituents, stainless steels are categorized into three classes: austenitic, ferritic and martensitic [2].

For austenitic stainless steel, austenite is the primary crystalline structure (face-centered cubic (FCC)) at room temperature. The austenitic phase is produced by adding elements such as Ni, Mn and N. These elements are known as austenite stabilizing elements. Austenitic stainless steels can be easily recognized as they are not magnetic. Austenitic stainless steel has excellent formability and weldability [3].

Ferritic stainless steel contains very little or no Ni and exhibits the ferrite crystal structure (BCC) at room temperature. Ferritic stainless steels are much less costly than austenitic stainless steels. Normally the Cr content ranges from 14 to 27 wt%. The addition of Cr contracts the austenitic region in the phase diagram. Hence, austenitic transformation occurs at a much higher temperature than for plain carbon steel. Ferritic stainless steel has good ductility and formability but poor high-temperature strength compared to austenitic stainless steel [4].

The microstructure of martensitic stainless steel is called martensite, which is a metastable phase formed via quenching from the high-temperature austenitic phase. It is a hard and brittle phase, so martensitic stainless steel is used mainly when high strength is required. The manufacture of martensitic stainless steel involves heat treatment of austenitic steel. Therefore, the Cr content is often lower than in ferritic stainless steel. Due to the low Cr content, the corrosion resistance of martensitic stainless steel is inferior to that of austenitic and ferritic stainless steels [3].

The most common stainless steel is 304 stainless steel. It is an austenitic stainless steel with Ni content of ~ 8 wt% and Cr content of ~ 18 wt%. With the addition of Ni, the austenitic phase field is extended to room temperature. 304 stainless steel is widely used in various household and industrial applications due to its high ductility, resulting in excellent drawing, forming, and spinning properties [5].

2.2 Principles of Aqueous Corrosion

2.2.1 Thermodynamics of corrosion

Metal corrosion in aqueous environments involves the oxidation of metal (anodic reaction) and reduction of solution species (cathodic reaction):

Oxidation:

$$\mathrm{M} \rightarrow \mathrm{M}^{z+} + z\mathrm{e}^{-} \tag{2.1}$$

Reduction:

$$\mathrm{Ox} + z\mathrm{e}^{-} \rightarrow \mathrm{Red} \tag{2.2}$$

Overall:

$$\mathrm{M} + \mathrm{Ox} \rightarrow \mathrm{M}^{z+} + \mathrm{Red} \tag{2.3}$$

Most corrosion reactions occur at constant pressure and temperature. Therefore, the spontaneity of a corrosion reaction can be determined from the Gibbs free energy of reaction (ΔG). A reduction of G as the reaction proceeds, i.e. $\Delta G < 0$, indicates the reaction is thermodynamically spontaneous.

Since aqueous corrosion of metal is an electrochemical process, the spontaneity of metal corrosion reactions can also be determined from the equilibrium potentials (E_{eq}) of reactions 2.1 and 2.2. The E_{eq} of anodic reactions (E_{a}) and cathodic reactions (E_{c}) relate to ΔG according to the following equation:

$$\Delta G = -zF(E_{\mathrm{c}} - E_{\mathrm{a}}) \tag{2.4}$$

where F is the Faraday constant (96,585 C·mol^{-1}). Therefore, a corrosion reaction is thermodynamically favoured only when E_{c} is higher than E_{a}, i.e.:

$$\Delta E_{\mathrm{eq}} = E_{\mathrm{c}} - E_{\mathrm{a}} > 0 \tag{2.5}$$

where ΔE_{eq} is the difference between E_{c} and E_{a}.

It should be also pointed out that the value of ΔG or ΔE_{eq} only indicates the thermodynamic favourability of a corrosion reaction but does not indicate anything about the reaction rate. The kinetics of corrosion reactions will be introduced in the next two sections.

2.2.2 Kinetics of electrochemical half reactions

The rate of an electrochemical half reaction is indicated by its current density (i). By convention, an oxidation reaction has a positive i and a reduction reaction has a negative i. When the electrode potential is equal to the E_{eq} of a half reaction, the half reaction is at equilibrium and the rates of the forward and reverse reactions are equal, giving a net current of 0 ($i = 0$). This equalized reaction rate is referred to as the exchange current density (i_0). When the electrode potential deviates from E_{eq}, the half reaction is displaced from equilibrium and will proceed at a certain rate. The deviation of the electrode potential from E_{eq} is called the overpotential (η). The relationship between i and η can be expressed using the Butler–Volmer equation:

$$i = i_0 \left\{ \exp\left(\frac{\alpha z F \eta}{RT}\right) - \exp\left[-\frac{(1-\alpha) z F \eta}{RT}\right] \right\} \tag{2.6}$$

where α is the charge transfer coefficient, z is the number of electrons involved in the reaction, R is the ideal gas constant (8.314 $\mathrm{J \cdot mol^{-1} \cdot K^{-1}}$) and T is the temperature (in K).

When the value of $|\eta|$ is high enough, the term $\exp\left(\frac{\alpha z F \eta}{RT}\right)$ or $\exp\left[-\frac{(1-\alpha) z F \eta}{RT}\right]$ in Eq. 2.6 can be neglected. For instance, at a higher η, Eq. 2.6 becomes:

$$i = i_0 \exp\left(\frac{\alpha z F \eta}{RT}\right) \tag{2.7}$$

which can be rearranged and gives the following equation (Tafel equation):

$$\eta = \frac{2.303RT}{\alpha zF}(\log i - \log i_0) \tag{2.8}$$

The Tafel equation implies a linear relationship between η and $\log i$ with a slope of $\frac{2.303RT}{\alpha zF}$, which is often referred to as the Tafel slope.

2.2.3 Mixed potential theory

A complete electrochemical reaction consists of at least two half reactions. For a naturally corroding system, the sum of the anodic currents must be equal to the sum of the cathodic currents due to charge balance:

$$\sum i_{\mathrm{a}} = \sum |i_{\mathrm{c}}| \tag{2.9}$$

where i_{a} and i_{c} represent the net anodic current of an oxidation half reaction and the net cathodic current of a reduction half reaction, respectively.

The values of i_{a} and $|i_{\mathrm{c}}|$ are dependent on the electrode potential. According to mixed potential theory, any electrochemical corrosion process will reach a mixed potential where Eq. 2.9 is satisfied. This electrode potential is called the corrosion potential (E_{corr}). In a simple and naturally corroding system involving two half reactions, at E_{corr}, the net anodic current of the oxidation half reaction and the net cathodic current of the reduction half reaction must be equal. The equalized current value is the corrosion current (i_{corr}):

$$i_{\mathrm{a}} = |i_{\mathrm{c}}| = i_{\mathrm{corr}} \tag{2.10}$$

Hence, the net current at E_{corr} is zero. When the system is polarized away from its naturally corroding state (the electrode potential is not at E_{corr}), the polarization current (net current) will be:

$$i = i_{\mathrm{a}} - |i_{\mathrm{c}}| \tag{2.11}$$

If both anodic and cathodic half reactions follow the Tafel equation, the net current *i* as a function of electrode potential *E* can be expressed as:

$$i = i_{\mathrm{corr}} \left\{ \exp\left[\frac{\alpha_{\mathrm{a}} zF(E - E_{\mathrm{corr}})}{RT} \right] - \exp\left[-\frac{\alpha_{\mathrm{c}} zF(E - E_{\mathrm{corr}})}{RT} \right] \right\} \tag{2.12}$$

where α_{a} and α_{c} are the charge transfer coefficients of the anodic and cathodic reactions, respectively. Eq. 2.12 is known as the Wagner–Traud equation [6]. When the electrode potential is not far from E_{corr} (normally < 10 mV), Eq. 2.12 can be approximated by a linear function:

$$i = i_{\mathrm{corr}} \left(\frac{\alpha_{\mathrm{a}} zF}{RT} + \frac{\alpha_{\mathrm{c}} zF}{RT} \right) (E - E_{\mathrm{corr}}) \tag{2.13}$$

The terms $\frac{\alpha_{\mathrm{a}} zF}{RT}$ and $\frac{\alpha_{\mathrm{c}} zF}{RT}$ are associated with the Tafel slope $\frac{2.303RT}{\alpha zF}$. Therefore, Eq. 2.13 can be further expressed as:

$$i = 2.303 i_{\mathrm{corr}} \left(\frac{1}{b_{\mathrm{a}}} + \frac{1}{b_{\mathrm{c}}} \right) (E - E_{\mathrm{corr}}) \tag{2.14}$$

where b_{a} and b_{c} are the Tafel slopes of the anodic and cathodic reactions, respectively. The slope of *E* versus *i* is referred to as the linear polarization resistance (R_{p}):

$$R_{\mathrm{p}} = \left. \frac{\mathrm{d}E}{\mathrm{d}i} \right|_{E = E_{\mathrm{corr}}} = \frac{b_{\mathrm{a}} b_{\mathrm{c}}}{2.303(b_{\mathrm{a}} + b_{\mathrm{c}}) i_{\mathrm{corr}}} \tag{2.15}$$

Eq. 2.15 was firstly proposed by Stern and Geary in 1957 [7] and hence is known as the Stern–Geary equation. It shows the inversely proportional relationship between R_{p} and i_{corr}. However, it should be noted that this relationship is only valid when both the anodic and cathodic reactions follow the Tafel equation.

One method for analyzing the kinetics of anodic and cathodic half reactions in a corroding system is a graphical representation, known as the Evans diagram. An example involving Fe corrosion in an acidic environment is shown in Figure 2.3 [8]. In the figure, the electrode potential is plotted as a function of $\log i$. Each half reaction consists of two lines, representing the forward and reverse reactions, respectively. The coordinates of their intersection point are the i_0 and E_{eq} of that half reaction. Assuming the Tafel equation applies, the intersection of the anodic and cathodic lines will give the i_{corr} and E_{corr}.

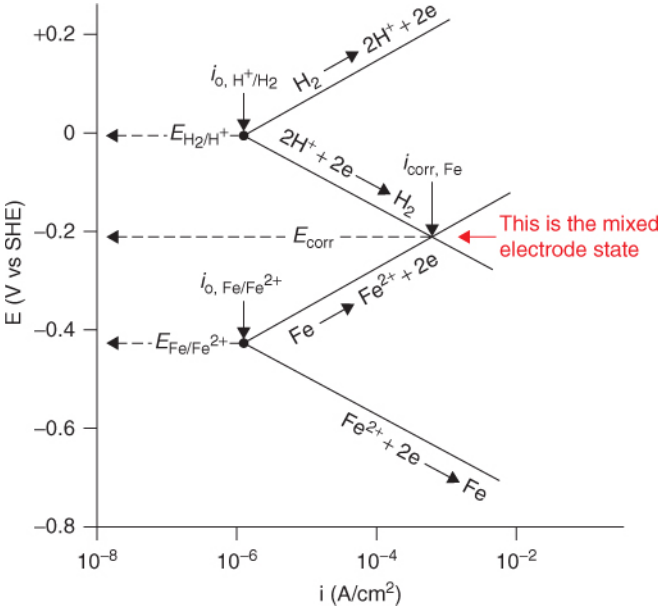

Figure 2.3 Evans diagram for a mixed electrode state of iron corrosion in acid [8].

2.2.4 Principles of galvanic corrosion

When two different alloys A and B are corroding independently in a given electrolyte, their E_{corr} values are usually different. Once they are electrically connected, current will flow between these two alloys due to the difference in their respective E_{corr} values. This current is known as the galvanic coupling current (I_{cpl}). At the same time, both alloys will be polarized to the same (new) electrode potential, known as the galvanic coupling potential (E_{cpl}). Charge balance for each individual alloy is no longer met due to the flow of current; however, it is still valid for the whole galvanic system:

$$I_{\mathrm{a,A}} + I_{\mathrm{a,B}} = |I_{\mathrm{c,A}}| + |I_{\mathrm{c,B}}| \tag{2.16}$$

In this equation, the total current rather than the current density is used because the surface areas of the two alloys could be different.

The E_{cpl} value is between the E_{corr} values of the two alloys. The alloy with a lower E_{corr} value is polarized more positively and referred to as the anode. Likewise, the one with a higher E_{corr} value is polarized more negatively and referred to as the cathode. After galvanic coupling, there will be a net oxidizing current at the anode and a net reducing current at the cathode. The two net currents are equal to the I_{cpl}. If alloy A is the anode ($E_{\mathrm{corr,A}} < E_{\mathrm{corr,B}}$), there will be:

$$I_{\mathrm{cpl}} = I_{\mathrm{a,A}} - |I_{\mathrm{c,A}}| = |I_{\mathrm{c,B}}| - I_{\mathrm{a,B}} \tag{2.17}$$

In addition, since after coupling the electrode potential of alloy A increases, and that of alloy B decreases, it is very likely that the metal oxidation rate on A will increase and that on B will decrease. Due to the possible acceleration of the corrosion rate at the anode, the anodic current at the anode after coupling ($I_{\mathrm{a,A}}$) is usually dealt with more carefully. To quantify the effect of galvanic coupling, also known as the galvanic effect (γ), the ratio of anode oxidation rate after coupling to its independent corrosion rate is often used.

$$\gamma = \frac{I_{\mathrm{a,A}}}{I_{\mathrm{corr,A}}} \tag{2.18}$$

The I_{cpl}, as the net current on each electrode in a galvanic couple, can be easily measured by experiment using a zero resistance ammeter (ZRA). However, the $I_{\mathrm{a,A}}$ cannot be directly measured due to the contribution of $I_{\mathrm{c,A}}$ to the net current. There is no general method to correlate $I_{\mathrm{a,A}}$ and I_{cpl}. Usually, two main approximations have been adopted:

(1) One type of approximation considers that at large polarizations ($E_{\mathrm{cpl}} - E_{\mathrm{corr,A}}$ is large), the contribution of $I_{\mathrm{c,A}}$ is negligible, i.e., $I_{\mathrm{a,A}} \gg |I_{\mathrm{c,A}}|$. Then $I_{\mathrm{a,A}}$ and I_{cpl} can be considered equal:

$$I_{\mathrm{a,A}} = I_{\mathrm{cpl}} \tag{2.19}$$

(2) The other type of approximation considers that at small polarizations ($E_{\mathrm{cpl}} - E_{\mathrm{corr,A}} \approx 0$), the contribution of $I_{\mathrm{c,A}}$ is no longer negligible. Assuming $I_{\mathrm{c,A}}$ follows the Tafel equation:

$$I_{\mathrm{c,A}} = -I_{\mathrm{corr,A}} \exp\left[-\frac{\alpha_{\mathrm{c}} zF\left(E_{\mathrm{cpl}} - E_{\mathrm{corr,A}}\right)}{RT}\right] \tag{2.20}$$

Combination of equations 2.17 and 2.20 gives:

$$I_{\mathrm{cpl}} = I_{\mathrm{a,A}} - I_{\mathrm{corr,A}} \exp\left[-\frac{\alpha_{\mathrm{c}} zF\left(E_{\mathrm{cpl}} - E_{\mathrm{corr,A}}\right)}{RT}\right] \tag{2.21}$$

When $E_{\mathrm{cpl}} \approx E_{\mathrm{corr,A}}$, equation 2.21 can be reduced to:

$$I_{\mathrm{cpl}} = I_{\mathrm{a,A}} - I_{\mathrm{corr,A}} \tag{2.22}$$

In this case, I_{cpl} is the increase in corrosion rate on A after galvanic coupling.

The relationship between the I_{cpl} and the corrosion kinetics of each coupling alloy has been further derived by Mansfeld [9]. This derivation is based on the first approximation introduced above, which assumes that $I_{\mathrm{a,A}} \gg |I_{\mathrm{c,A}}|$ and $I_{\mathrm{a,B}} \ll |I_{\mathrm{c,B}}|$, and both $I_{\mathrm{a,A}}$ and $I_{\mathrm{c,B}}$ follow the Tafel equation,

$$I_{\mathrm{cpl}} = I_{\mathrm{corr,A}} \exp\left[\frac{2.303\left(E_{\mathrm{cpl}} - E_{\mathrm{corr,A}}\right)}{b_{\mathrm{a}}}\right] = I_{\mathrm{corr,B}} \exp\left[\frac{2.303\left(E_{\mathrm{corr,B}} - E_{\mathrm{cpl}}\right)}{b_{\mathrm{c}}}\right] \tag{2.23}$$

After eliminating E_{cpl} in equation 2.23, we obtain:

$$\log I_{\mathrm{cpl}} = \frac{E_{\mathrm{corr,B}} - E_{\mathrm{corr,A}}}{b_{\mathrm{a}} + b_{\mathrm{c}}} + \frac{b_{\mathrm{a}}}{b_{\mathrm{a}} + b_{\mathrm{c}}} \log I_{\mathrm{corr,A}} + \frac{b_{\mathrm{c}}}{b_{\mathrm{a}} + b_{\mathrm{c}}} \log I_{\mathrm{corr,B}} \tag{2.24}$$

Because the anode is often of greater interest in galvanic corrosion studies, the coupling current density (i_{cpl}) used is usually obtained by normalizing the I_{cpl} to the anode surface area. $I_{\mathrm{corr,A}}$ and $I_{\mathrm{corr,B}}$ in equation 2.24 can also be expressed using their respective corrosion current densities and surface areas and therefore:

$$\log i_{\mathrm{cpl}} = \frac{E_{\mathrm{corr,B}} - E_{\mathrm{corr,A}}}{b_{\mathrm{a}} + b_{\mathrm{c}}} + \frac{b_{\mathrm{a}}}{b_{\mathrm{a}} + b_{\mathrm{c}}} \log i_{\mathrm{corr,A}} + \frac{b_{\mathrm{c}}}{b_{\mathrm{a}} + b_{\mathrm{c}}} \log\left(\frac{A_{\mathrm{B}}}{A_{\mathrm{A}}} i_{\mathrm{corr,B}}\right) \qquad (2.25)$$

where A_{A} and A_{B} are the surface areas of alloy A and B, respectively. The equation clearly shows how i_{cpl} (normalized to the surface area of alloy A) is affected by the surface area ratio between the cathode and anode. There is a linear relationship between $\log i_{\mathrm{cpl}}$ and $\log\left(\frac{A_{\mathrm{B}}}{A_{\mathrm{A}}}\right)$.

In many corrosion systems, the reduction reaction is the oxygen reduction reaction (ORR). When ORR is under diffusion control,

$$i_{\mathrm{corr,B}} = i_{\mathrm{L}} \qquad (2.26)$$

where i_{L} is the diffusion limiting current density. Also, the value of b_{c} approaches infinity ($b_{\mathrm{c}} \to \infty$) under diffusion control. Then, equation 2.25 becomes:

$$i_{\mathrm{cpl}} = \frac{A_{\mathrm{B}}}{A_{\mathrm{A}}} i_{\mathrm{L}} \qquad (2.27)$$

2.3 Principles of Water Radiolysis

2.3.1 Interaction of ionizing radiation with matter

The decay of radionuclides generates ionizing radiation. In the nuclear decay process, an α-particle or a β-particle is usually emitted, which are referred to as α-decay and β-decay, respectively. An α-particle is a high-energy helium nucleus (${}^{4}_{2}\mathrm{He}^{2+}$) and a β-particle is a fast electron. The nuclear decay of most radionuclides is accompanied by the emission of high-energy photons (X-ray or γ-ray). Particles emitted via nuclear decay do not have sufficient energies to induce further nuclear reactions, but the energy is much higher than that required to ionize atoms and molecules (typically several tens of eV). Therefore, the high-energy charged particles (e.g., α and β particles) and photons (X-rays and γ-rays) are often referred to as ionizing radiation. Ionizing radiation transfers its energy to an interacting medium mainly by colliding non-discriminately with the electrons bound to atoms and molecules in the medium. Due to its high kinetic energy each radiation particle undergoes a series of collisions before it loses most of its kinetic energy.

The α-particles interact with electrons within a medium, primarily through inelastic collisions, along the radiation path. Due to their large size in comparison with the electrons they perturb, only small amounts of energy are lost with each collision, and the large α-particles are not easily deflected from their paths. However, the large collision cross section with electrons prevents these particles from penetrating deeply into the medium, resulting in a very dense collection of excited and ionized particles along a short stretch of the radiation track.

Beta-particles share the same mass as the electrons with which they interact. The particles can lose up to half of their energy with each collision and can be deflected through a large angle. β-particles can interact with additional electrons to lose their remaining energy. Also, the electrons with which the β-particles interacted can continue to propagate the electron ejection process, but with reduced efficiency through each cascade. Therefore, these particles create a low-density collection of ions or excited molecules along their radiation tracks.

Gamma-rays transfer most of their energy by Compton scattering if their energy exceeds 0.01 MeV. In Compton scattering, the interaction of a γ-ray with matter causes electron ejection and the γ-ray photon emerges with a reduced energy. Due to the low probability of Compton scattering, the penetration depth of γ-radiation is large relative to all other radiation forms. The ejected electron (a 'hot' primary electron) is very much like a β-particle (fast electron) and therefore the chemical effects induced by β and γ-radiation in water are essentially the same for the same absorbed energy. Because γ-rays must first interact with atoms and molecules to create a primary fast electron, they have a much greater penetration depth than β-particles.

The rate of energy transfer per unit of penetration depth through a medium is known as the linear energy transfer (LET) rate. The LET rate depends on the type of radiation and the interacting medium. For a given medium, it is highest for α-particles, lower for β-particles, and lowest for γ-photons.

2.3.2 Water radiolysis by γ-radiation

The interaction between ionizing radiation and a water molecule leads to the ionization or excitation of the water molecule. The result is creation of ion pairs ($H_2O^{\bullet +}$ and e^-_{hot}) or electronically excited water molecules (H_2O^*) along the radiation track. The electron of this ion pair is labelled as 'hot' because it has a kinetic energy that is sufficiently high to excite or ionize one or more neighbouring water molecules. Secondary (or tertiary) ionization caused by this 'hot' electron will occur near the previous ionization, resulting in a cluster of 2-3 ion pairs (or excited water molecules) near the radiation track. This cluster is referred to as a "spur" [10]. The spur density along the track depends mainly on the collision rate of the radiation particle with the bound electrons in the water molecules. For low LET β- and γ-radiation, the inelastic collision mean free path of the radiation (the primary electron) in liquid water at 25 °C is about 1 μm, while the spur size is about 20 nm. The large distance between the spurs on a radiation track means that interactions between spurs will be negligible. However, this is not the case for high LET α-radiation, where the spurs overlap considerably [10].

Once the spurs are formed, the electrons, ions and radicals within the spur undergo various energy transfer processes including energy relaxation to vibrational and rotational motions, dissociation, ion-molecule reaction and geminate recombination (Figure 2.4). These processes occur in spurs or solvent cages, while the spurs continue to expand. The spurs overlap and the radiolysis products along the ionizing radiation track become uniformly distributed. The time to reach this homogeneous out-of spur distribution stage is 100 ns in water at 25 °C [10]. The species present at this stage are normally referred to as primary radiolysis products and their concentrations per unit absorbed energy are called primary radiolysis yields (G value). The generation of primary γ-radiolysis products can be expressed as:

$$\mathrm{H_2O} \rightarrow \bullet\,\mathrm{OH},\ \bullet\,\mathrm{e_{aq}^-}, \bullet\,\mathrm{H}, \mathrm{H_2}, \mathrm{H_2O_2}, \mathrm{H^+} \qquad (2.28)$$

and the G values of the primary γ-radiolysis products are summarized in Table 2.1

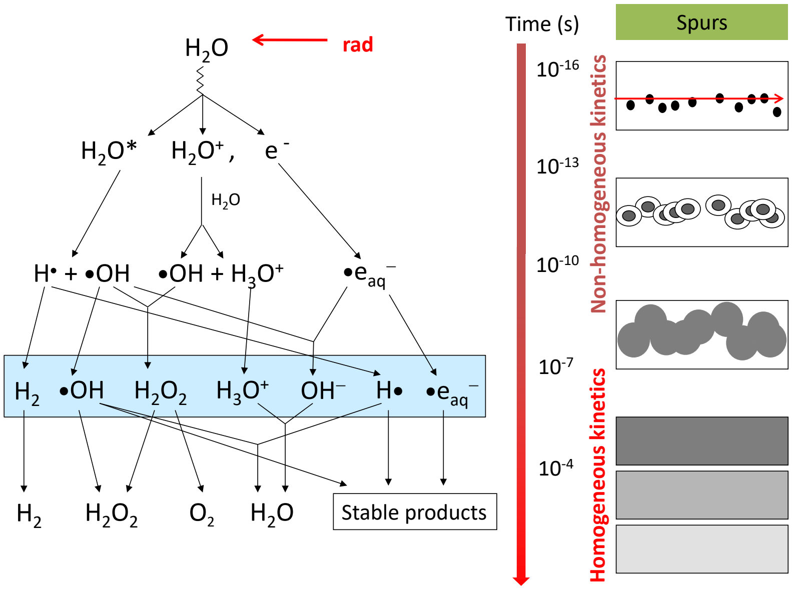

Figure 2.4 Schematic of water radiolysis as a function of time after absorption of radiation. The expansion of spurs with time is shown in the right-hand panel.

Table 2.1 The primary γ-radiolysis yields (G value ($\mu mol \cdot J^{-1}$)) for liquid water.

Species	**G value ($\mu mol \cdot J^{-1}$)**
H_2O	−0.41
•OH	0.27
$\bullet e_{aq}^{-}$	0.26
•H	0.06
H_2	0.04
H_2O_2	0.07
H^+	0.26

When exposed to a continuous source of γ-radiation, the primary radiolysis products form continuously and undergo a series of chemical reactions, reaching steady state on a time scale of seconds. The steady state concentration of each species is affected by various solution parameters including pH and chemical additives. Generally, the radical species have high reactivity and therefore short lifetimes and so their steady state concentrations are orders of magnitude lower than those of the molecular species (H_2O_2, H_2, and O_2).

Reactions between metal and solution species require the diffusion of reactive species to the metal surface. The diffusion rate is strongly dependent on the steady state concentration in the bulk solution. Therefore, the molecular species are expected to participate in interfacial reactions to a much more significant extent than radical species. Among the molecular species, the radiolytic oxidants H_2O_2 and O_2 are expected to have a much larger influence than the reductant H_2, as the reactivity of H_2 is low at room temperature.

2.4 Corrosion of Carbon Steel in Reactor Environments

Carbon steel is extensively used in nuclear reactors due to its excellent mechanical properties and low cost [11]. Typical examples are the feeder pipes of the CANDU primary coolant loop and the reactor pressure vessel of pressurized water reactors. To mimic these service environments, most tests have been performed in high-temperature (up to 300 °C) borate or LiOH solutions with low O_2 content. Some tests were conducted in the presence of radiation. Under these conditions, corrosion results in the formation of a compact and uniform magnetite layer on the surface [12]. Various mechanisms have been proposed [13–15].

Bojinov and coworkers developed a customized photoelectrochemical measurement apparatus and performed *in-situ* characterization of the oxide on pure iron in 0.05 M $Na_2B_4O_7$ solution in the temperature range 100 to 200 °C [16]. Their results showed that the nature of the photoactive phase in the passive film formed on pure iron is independent of temperature, but that the oxide growth rate increases with temperature. In another study [17], the same researchers characterized the oxide formed on carbon steel in pH 10.2 LiOH solution at 250 °C. The oxide formed was magnetite, which behaves as an n-type semiconductor. The oxide growth kinetics were quantitatively described using the mixed-conduction model [18].

Cheng and Steward studied the corrosion of A106B steel in pH 10.6 LiOH solutions using a high-temperature water loop system [19]. The magnetite film had a bi-layer structure, with an compact inner layer and a loose outer layer. A mechanistic model was proposed to explain the magnetite formation process during corrosion. According to the model, the inner layer grows via the Schikorr reaction [20,21], while the outer layer grows via solution precipitation after saturation of the solution phase.

Xiao et al. studied the effect of temperature, solution composition and dissolved O_2 on the corrosion behaviour of A508III steel in boric acid solution [22]. They found that in deaerated solutions the corrosion rate increases with temperature, while in aerated solutions, due to a combination of the increased diffusion coefficient and reduced solubility of O_2 at higher temperatures, the corrosion rate initially increases and then decreases with temperature, reaching a peak at ~75 °C.

Kumar and coworkers investigated oxide formation on an A333 steel surface in pH 10.2 LiOH solutions at 250 °C [23]. The results showed that the defect density of the magnetite layer is initially high but gradually decreases and stabilizes after ~ 35 h exposure. The defect density level was determined to be ~ 3×10^{21} cm^{-3}. In another work, the effect of carbon steel microstructure on oxide formation was investigated [24]. It was found that carbon steel with higher carbon content initially oxidizes faster, but over long time periods this difference decreases.

Daub et al. performed a comprehensive program of study on carbon steel corrosion in CANDU reactor coolant environments. For instance, they investigated the effect of γ-radiation on carbon steel corrosion in mildly basic solutions (pH 10.6) and compared it with that of chemically added H_2O_2, which is considered to be the key radiolytically produced oxidant at room temperature. The results confirmed that H_2O_2 is the key radiolysis product that controls carbon steel corrosion and indicated that the rate of carbon steel corrosion in a γ-radiation environment can be predicted if the concentration of radiolytically produced H_2O_2 can be measured or determined in advance [25]. Fu and Zhang et.al looked further into the decomposition mechanism of H_2O_2 and the kinetics of H_2O_2 reactions with oxide films on carbon steel [26,27].

Daub et al. also investigated the kinetics of carbon steel corrosion in a γ-radiation field, but at a higher temperature (150 °C). It was found that the oxide from carbon steel corrosion under γ-radiation was non-porous and uniform, and no localized corrosion was observed. The oxides formed on the surface were a mixture of Fe_3O_4 and γ-Fe_2O_3. They also concluded that water radiolysis limits carbon steel corrosion under the studied conditions due to the formation of a film on the steel surface that is more passive in the presence of ionizing radiation [28].

The concentrations of soluble corrosion products (metal ions) are expected to be near the saturation limit in the circulating coolant of a nuclear reactor, which makes the prediction of the net effect of radiation on steel corrosion in the presence of dissolved metal ions difficult. Hence, Wang et al. investigated the effect of the presence of dissolved ferrous ion (Fe^{2+}) on surface oxide film growth and conversion on carbon steel, and how it could affect subsequent metal oxidation. The results showed that the presence of Fe^{2+} in the solution reduced the metal oxidation rate at potentials < -0.4 V_{SCE} while it increased the formation of γ-FeOOH on the carbon steel surface at potentials > -0.4 V_{SCE} [29].

Morco et al. studied the effect of γ-radiation on the corrosion behaviour of carbon steel in a non-aqueous electrolyte ($[P_{14666}][Br]$ionic liquid). They found that substantial corrosion was seen in the absence of γ-radiation whereas less corrosion occurred in the presence of radiation due to the formation of protective oxides on the carbon steel surface [30].

Guo conducted a systematic study of carbon steel corrosion in which the effects of solution volume to surface area ratio, pH, dissolved O_2 and γ-radiation were investigated [31]. Although this work was specifically addressing the potential corrosion of the carbon steel vessel used in the proposed Canadian used fuel container [32,33], it still can provide some general insight on the corrosion dynamics of carbon steel used in reactor environments. The results of this study demonstrated that carbon steel corrosion involves many oxidation steps that lead to the formation and growth of different oxides on the surface, and the dissolution of metal cations. The dynamics of carbon steel corrosion may not approach and reach a single steady state, but continue to evolve with time, and reach different steady states depending on the solution parameters. A mechanism that can explain the carbon steel corrosion dynamics under different solution conditions was proposed.

2.5 Corrosion of Stainless Steel in Reactor Environments

Stainless steel is an ideal material for many applications that require high corrosion resistance and mechanical strength. In the nuclear industry, stress corrosion cracking (SCC) of austenitic stainless steel is the subject of intense research efforts. SCC is a type of localized corrosion which requires both tensile stress and an aggressive environment to promote initiation and propagation [34]. There are many existing studies on the effects of various environmental parameters on crack initiation and crack growth on 304 and 316L stainless steels. The aggressive conditions include high temperatures (300 °C-400 °C) [35–40], oxygen [37,41,42], aggressive anions [40,43–46], and the presence of neutron radiation [47,48]. Typically, the chemical environments that can cause SCC in stainless steel involve chloride, sulfides, caustic solutions and hydrogen [49]. For the work presented here, given that the solution environment surrounding the weld region does not satisfy these requirements for the promotion of SCC, only literature on the general corrosion of stainless steels is reviewed below.

Stainless steel is a common structural material in nuclear power plants. To minimize the degradation (via corrosion) of structural materials and maximize their service lifetimes, the water chemistry in contact with these materials must be strictly controlled. A number of studies have been conducted to investigate the effects of different water chemistry on the corrosion behaviour of stainless steel. These have involved parameters such as pH [50–55], dissolved oxygen [56–65], and dissolved hydrogen [63,65–69]. Wang et al. studied the influence of pH on the corrosion behaviour of Type-316L stainless steel in hydrogenated high temperature (300 °C) water. They found that the stability of the oxide films formed is lower at higher pHs and therefore recommended maintaining a lower pH in hydrogenated high temperature water to mitigate the corrosion of structural materials [55]. Duan et al. investigated the effect of dissolved oxygen on the electrochemical behaviour and oxide film formation on Type-304L and 316L stainless steel. The results revealed that the passivity of the oxide films formed on both steels diminished with increasing temperatures and that the films consist of an inner layer of Cr oxides with an outer layer of Fe oxide and Ni-Fe spinel. The oxide films formed on type 316L steel have higher Cr content making it more passive than 304L [70].

Stainless steel is also widely used in pipe materials for the secondary circuit of nuclear power plants where the alloy surface is in contact with high-temperature water. To ensure the long-term integrity of nuclear reactors, the corrosion degradation of stainless steel at high temperatures has been extensively studied [55,58,73,74,59,63,65,66,69–72]. For instance, Xu et al. studied the evolution of the electrochemical behaviour and oxide film properties of Type-304L stainless steel in high-temperature (250 °C) lithium borate buffer solutions to simulate the pressurized water reactor (PWR) primary water environment. The results indicated that the corrosion resistance of the steel increased with immersion time. They proposed that the metal oxidation current is controlled by the type of oxide film formed at the early stage of immersion and by the diffusion process of metal cations in the oxide film [71]. Sun et al. and Wang et al. further investigated the effect of temperature (varying from 25 °C-300 °C) on the corrosion behaviour of 304L stainless steel in the same solutions. Both reached the same conclusion that the stainless steel behaviour changed from passivity to active dissolution as the temperature increased. They attributed this to a change in the characteristics of the film on the surface: evolution from a protective single-layer to a less protective double-layer [72–74].

In the nuclear industry, the exposure of materials to ionizing radiation is inevitable. Radiation induces radiolysis products in the water in contact with these materials, thus altering their corrosion behaviour. Understanding the effects of radiation on corrosion under an array of conditions is critical. Knapp et al. identified different potential regions for oxide formation on Type-316L stainless steel under mildly basic solutions and probed the effect of γ-radiation on its corrosion behaviour. The results indicated that ionizing radiation affects the types of oxide formed on the stainless steel surface [75]. Similar results were also observed for a Ni-Fe-Cr alloy (Inconel 600) over a range of pHs (pH 6.0-10.6) by Musa et al. [76,77]. Raiman studied the effects of proton radiation on the corrosion of 316L stainless steel in simulated PWR primary water coolant and found that irradiation led to the formation of hematite on the outer layer of the sample surface and the dissolution of the Cr-rich inner layer. The effect of radiation on the corrosion of 316L was found to occur via the water radiolysis mechanism [78].

2.6 Galvanic Corrosion Studies of Carbon Steel

Galvanic corrosion between carbon steel and passive alloys has been extensively studied. Most of these studies have focused on chloride- or sulfide-containing environments. Common methodologies include the measurement of E_{cpl} and I_{cpl}, combined with weight loss measurements and surface analysis. The parameters that have been previously studied are: cathode/anode surface area ratio, electrolyte composition, temperature and flow rate.

Varela et al. studied the galvanic corrosion between SS400 carbon steel and 304 stainless steel in CO_2 + NaCl solutions [79]. They used experimentally measured polarization curves as boundary conditions and calculated the current and potential distribution across the interface of the galvanic couple. $FeCO_3$ was determined as the corrosion product of carbon steel, while the corrosion of stainless steel was negligible.

Abreu et al. performed a galvanic corrosion study between 1023 carbon steel and 304L stainless steel in 0.01 M NaOH solution [80]. Under the studied conditions, passive layers were formed on both steels. Although the passive layer formed on carbon steel was less resistive than that on stainless steel, no significant galvanic corrosion occurred. Similar conclusions were reached in the later study of Qian et al. which involved steel embedded in concrete and $Ca(OH)_2$ matrices [81,82].

Yin et al. studied the effects of temperature and surface area ratio on the galvanic corrosion between SM 80SS carbon steel and the Ni-based alloy G3 in NaCl solution [83]. They found that increasing temperature or surface area ratio increased I_{cpl}. The most significant temperature effect was observed between 30 and 60 ºC. A quadratic equation was used to describe the relationship between I_{cpl} and the surface area ratio.

Dong et al. performed studies of galvanic corrosion between 1020 carbon steel and 304L stainless steel in chloride and sulfide solutions [84,85]. The anodic reaction on carbon steel was found to be under activation control, with the cathodic reaction being controlled by the oxygen reduction reaction. In the presence of sulfide, the galvanic effect decreased with $[S^{2-}]$ due to the formation of a protective sulfide film on the carbon steel.

Feng et al. performed galvanic corrosion tests on carbon steel and 304 stainless steel in chloride-contaminated mortars [86]. They found that carbon steel did present a high risk of galvanic corrosion when initially coupled to the stainless steel as at this point the value of i_{cpl} was of the order of 10^{-4} A·cm^{-2}. However, after 238 d of immersion, the i_{cpl} decreased to ~ 10^{-8} A·cm^{-2}, indicating that over extended times there was no actual risk of significant galvanic corrosion.

Fushimi et al. probed the current distribution during the galvanic corrosion of carbon steel-Type-309 stainless steel welds in NaCl solution using a newly developed multi-channel electrode technique. They found that the weldment and base steel acted as cathode and anode, respectively, and that the difference between the anodic and cathodic participating currents was larger at the earlier stages (< 40 ks) of the immersion tests. The anodic participating current decreased as the base steel became covered with rust [87].

Ren et al. studied galvanic corrosion between C110 carbon steel and the Ni-based alloy G3 in H_2S + CO_2 solution and humid vapour [88]. The corrosion product on the carbon steel was composed of FeS_y, $FeCO_3$, Fe_2O_3 and FeOOH, the formation of which supressed the galvanic effect.

Wang et al. studied the galvanic corrosion between the low alloy steel A508 and the Ni-based alloy 52M in NaCl solution [89]. Their results showed that MnS inclusions were the initiation sites for pitting corrosion in A508. When pitting occurred, the remaining part of the interface region acted as the cathode, and galvanic corrosion between the two substrates did not occur. However, when H_3BO_3 was added to the electrolyte, A508 degraded via general corrosion and galvanic coupling occurred between A508 and Alloy 52M.

Standish et al. investigated the effect of O_2 and the anode/cathode surface area ratio on the galvanic corrosion of a carbon steel-copper couple in NaCl solutions. By monitoring the changes in the galvanic current, galvanic potential, corrosion products and surface damage, they concluded that galvanic corrosion of steel exposed to aerated solutions was most severe with the largest Cu:Steel area ratio [90].

Wu and coworkers studied the effects of different exposure environments (temperature, aeration, irradiation) on the galvanic coupling between a bold surface and a crevice surface of carbon steel. They observed greater corrosion attack on the bold surface of the carbon steel crevice coupon. A higher metal oxidation rate on the bold surface was observed, concurrent with an increase in the solution reduction rate on the crevice surface. They also developed a carbon steel corrosion mechanism that can be used to explain the corrosion evolution of the two surfaces when they are galvanically coupled [91].

2.7 References

[1] Ramesh Singh, Applied Welding Engineering, 2nd ed., Elsevier Inc., 2015.

[2] W.D. Callister, Jr., D.G. Rethwisch, Materials Science and Engineering: An Introduction, 8th ed., John Wiley & Sons, Inc., New York, 2009.

[3] J.R. Davis, Alloy Digest Sourcebook: Stainless Steels, ASM International, 2000.

[4] M.K. Banerjee, Comprehensive Materials Finishing, Elsevier, 2017.

[5] A. Kamble, V. Kulkarni, A Text Book of Metallurgy: Properties and Applications of Ferrous and Non-ferrous Materials, Harshal Publications, 2017.

[6] G.S. Frankel, Wagner–Traud to Stern–Geary: Development of corrosion kinetics, in: G.S. Frankel, R.P. Frankenthal (Eds.), Corrosion Science: A Retrospective and

Current Status, In Honor of Robert P. Frankenthal, Electrochemical Society, 2003, pp. 33–41.

[7] M. Stern, A.L. Geary, J. Electrochem. Soc., 104 (1957) 56–63.

[8] Y. Tan, Heterogeneous Electrode Processes and Localized Corrosion, John Wiley & Sons, Inc., Hoboken, 2013.

[9] F. Mansfeld, CORROSION, 27 (1971) 436–442.

[10] J.W.T. Spinks, R.J. Woods, An Introduction to Radiation Chemistry, John Wiley & Sons, Inc., New York, 1990.

[11] F. Cattant, D. Crusset, D. Féron, Mater. Today, 11 (2008) 32–37.

[12] V. Malinovschi, C. Ducu, N. Aldea, M. Fulger, J. Nucl. Mater., 352 (2006) 107–115.

[13] J.E. Castle, G.M.W. Mann, Corros. Sci., 6 (1966) 253–262.

[14] L. Tomlinson, CORROSION, 37 (1981) 591–596.

[15] J. Robertson, Corros. Sci., 29 (1989) 1275–1291.

[16] M. Bojinov, P. Kinnunen, T. Laitinen, K. Mäkelä, T. Saario, P. Sirkiä, Electrochem. Commun., 4 (2002) 222–226.

[17] M. Bojinov, K. Gaonkar, S. Ghosh, V. Kain, K. Kumar, T. Saario, Corros. Sci., 51 (2009) 1146–1156.

[18] B. Beverskog, M. Bojinov, P. Kinnunen, T. Laitinen, K. Mäkelä, T. Saario, Corros. Sci., 44 (2002) 1923–1940.

[19] Y.F. Cheng, F.R. Steward, Corros. Sci., 46 (2004) 2405–2420.

[20] M. Booy, T.W. Swaddle, Can. J. Chem., 56 (1978) 402–403.

[21] R.O. Rihan, S. Nešić, Corros. Sci., 48 (2006) 2633–2659.

[22] Q. Xiao, Z. Lu, J. Chen, M. Yao, Z. Chen, A. Ejaz, J. Nucl. Mater., 480 (2016) 88–99.

[23] M.K. Kumar, K. Gaonkar, S. Ghosh, V. Kain, M. Bojinov, T. Saario, J. Nucl. Mater., 401 (2010) 46–54.

[24] P.K. Sinha, M.K. Kumar, V. Kain, J. Nucl. Mater., 464 (2015) 20–27.

[25] K. Daub, X. Zhang, J.J. Noël, J.C. Wren, Electrochim. Acta, 55 (2010) 2767–2776.

[26] D. Fu, X. Zhang, P.G. Keech, D.W. Shoesmith, J.C. Wren, Electrochim. Acta, 55 (2010) 3787–3796.

[27] X. Zhang, W. Xu, D.W. Shoesmith, J.C. Wren, Corros. Sci., 49 (2007) 4553–4567.

[28] K. Daub, X. Zhang, J.J. Noël, J.C. Wren, Corros. Sci., 53 (2011) 11–16.

[29] L. Wang, K. Daub, Z. Qin, J.C. Wren, Electrochim. Acta, (2012).

[30] R.P. Morco, A.Y. Musa, M. Momeni, J.C. Wren, Corros. Sci., 102 (2016) 1–15.

[31] D. Guo, Corrosion Dynamics of Carbon Steel in Used Fuel Container Environments, The University of Western Ontario, London, ON, 2018.

[32] D.S. Hall, P.G. Keech, Corros. Eng. Sci. Technol., 52 (2017) 2–5.

[33] P.G. Keech, P. Vo, S. Ramamurthy, J. Chen, R. Jacklin, D.W. Shoesmith, Corros. Eng. Sci. Technol., 49 (2014) 425–430.

[34] J.. Davis, Corrosion of Weldments, ASM International, 2006.

[35] W. Yang, G. Li, C. Huang, J. Zhou, Z. Lü, Chinese J. Mech. Eng. (English Ed., 23 (2010) 677–683.

[36] J. Congleton, R.A. Berrisford, W. Yang, Corrosion, 51 (1995) 901–910.

[37] D. Peng, S. Hu, P. Zhang, H. Wang, Xiyou Jinshu Cailiao Yu Gongcheng/Rare Met. Mater. Eng., 43 (2014) 178–183.

[38] Y. Guan, Y. Li, C. Dong, F. Liu, X. Li, A. Ren, X. Cheng, Beijing Keji Daxue Xuebao/Journal Univ. Sci. Technol. Beijing, 31 (2009) 1122–1126.
[39] T. Fujii, K. Tohgo, A. Kenmochi, Y. Shimamura, Corros. Sci., 97 (2015) 139–149.
[40] L.F. Lin, G. Cragnolino, Z. Szklarska-Smialowska, D.D. Macdonald, CORROSION, 37 (1981) 616–627.
[41] L. Zhang, J. Wang, J. Nucl. Mater., 446 (2014) 15–26.
[42] H. Hirano, N. Aoki, T. Kurosawa, CORROSION, 39 (1983) 313–322.
[43] D. Peng, S. Hu, P. Zhang, H. Wang, Wuhan Ligong Daxue Xuebao/Journal Wuhan Univ. Technol., 36 (2014) 32–39 and 51.
[44] M. Gomez-Duran, D.D. Macdonald, Corros. Sci., 48 (2006) 1608–1622.
[45] M. Gomez-Duran, D.D. Macdonald, Corros. Sci., 45 (2003) 1455–1471.
[46] S. Roychowdhury, S.K. Ghosal, P.K. De, J. Mater. Eng. Perform., 13 (2004) 575–582.
[47] M. Mayuzumi, K. Hide, T. Arai, Corrosion, 57 (2001) 214–220.
[48] Y. Kaji, H. Ugachi, T. Tsukada, J. Nakano, Y. Matsui, K. Kawamata, A. Shibata, M. Ohmi, N. Nagata, K. Dozaki, H. Takiguchi, J. Nucl. Sci. Technol., 45 (2008) 725–734.
[49] R. Francis, The Corrosion of Duplex Stainless Steels: A Practical Guide for Engineers, NACE International, 2018.
[50] H.. Leckie, CORROSION, 24 (1968) 70–74.
[51] S. Atashin, M. Pakshir, A. Yazdani, Mater. Des., 32 (2011) 1315–1324.
[52] A.U. Malik, P.C. Mayan Kutty, N.A. Siddiqi, I.N. Andijani, S. Ahmed, Corros. Sci., 33 (1992) 1809–1827.

[53] J.L. Guiñon, J. Garcia-Anton, V. Pérez-Herranz, G. Lacoste, CORROSION, 50 (1994) 240–246.

[54] L. Freire, M.J. Carmezim, M.G.S. Ferreira, M.F. Montemor, Electrochim. Acta, 56 (2011) 5280–5289.

[55] J. Wang, J. Wang, H. Ming, Z. Zhang, E.-H. Han, Mater. Corros., 69 (2018) 580–589.

[56] Y.X. Qiao, Y.G. Zheng, P.C. Okafor, W. Ke, Electrochim. Acta, 54 (2009) 2298–2304.

[57] M. Oyaidzu, K. Isobe, T. Hayashi, T. Yamanishi, J. Nucl. Sci. Technol., 48 (2011) 880–884.

[58] X. Tang, S. Wang, L. Qian, Y. Li, Z. Lin, D. Xu, Y. zhang, Chem. Eng. Res. Des., 100 (2015) 530–541.

[59] W. Kuang, X. Wu, E.-H. Han, Corros. Sci., 63 (2012) 259–266.

[60] Z. Feng, X. Cheng, C. Dong, L. Xu, X. Li, J. Nucl. Mater., 407 (2010) 171–177.

[61] K.S. Raja, D.A. Jones, Corros. Sci., 48 (2006) 1623–1638.

[62] J.H. Zheng, W.F. Bogaerts, K. Phlippo, Fusion Eng. Des., 24 (1994) 299–307.

[63] Y.J. Kim, CORROSION, 55 (1999) 81–88.

[64] M. Kodama, S. Nishimura, J. Morisawa, S. Shima, S. Suzuki, M. Yamamoto, Effects of fluence and dissolved oxygen on IASCC in austenitic stainless steels, American Nuclear Society, Inc, United States, 1992.

[65] L.W. Niedrach, W.H. Stoddard, CORROSION, 42 (1986) 696–699.

[66] Y.J. Kim, CORROSION, 51 (1995) 849–860.

[67] L. Dong, Q. Peng, Z. Zhang, T. Shoji, E.-H. Han, W. Ke, L. Wang, Nucl. Eng. Des.,

295 (2015) 403–414.

[68] M.Z. Yang, J. Electrochem. Soc., 146 (1999) 2107.

[69] T. Terachi, T. Yamada, T. Miyamoto, K. Arioka, K. Fukuya, J. Nucl. Sci. Technol., 45 (2008) 975–984.

[70] Z. Duan, F. Arjmand, L. Zhang, H. Abe, J. Nucl. Sci. Technol., 53 (2016) 1435–1446.

[71] J. Xu, X. Wu, E.-H. Han, Electrochim. Acta, 71 (2012) 219–226.

[72] H. Sun, X. Wu, E.-H. Han, Y. Wei, Corros. Sci., 59 (2012) 334–342.

[73] H. Sun, X. Wu, E.-H. Han, Corros. Sci., 51 (2009) 2840–2847.

[74] K. Wang, J. Wang, W. Hu, Mater. Des., 82 (2015) 155–163.

[75] Q.W. Knapp, J.C. Wren, Electrochim. Acta, 80 (2012) 90–99.

[76] A.Y. Musa, J.C. Wren, Corros. Sci., 109 (2016) 1–12.

[77] A.Y. Musa, M. Behazin, J.C. Wren, Electrochim. Acta, 162 (2015) 185–197.

[78] S.S. Raiman, Irradiation accelerated corrosion of 316L stainless steel in simulated primary water, The Univeristy of Michigan, 2016.

[79] F.E. Varela, Y. Kurata, N. Sanada, Corros. Sci., 39 (1997) 775–788.

[80] C.M. Abreu, M.J. Cristóbal, M.F. Montemor, X.R. Nóvoa, G. Pena, M.C. Pérez, Electrochim. Acta, 47 (2002) 2271–2279.

[81] S. Qian, D. Qu, G. Coates, Can. Metall. Q., 45 (2006) 475–483.

[82] S. Qian, D. Qu, J. Appl. Electrochem., 40 (2010) 247–256.

[83] Z.F. Yin, M.L. Yan, Z.Q. Bai, W.Z. Zhao, W.J. Zhou, Electrochim. Acta, 53 (2008) 6285–6292.

[84] C.F. Dong, K. Xiao, X.G. Li, Y.F. Cheng, Wear, 270 (2010) 39–45.

[85] C.F. Dong, K. Xiao, X.G. Li, Y.F. Cheng, J. Mater. Eng. Perform., 20 (2011) 1631–1637.

[86] X. Feng, J. Liu, C. Hang, Z. Lu, Y. Jiang, Y. Xu, D. Chen, Int. J. Electrochem. Sci., 11 (2016) 5226–5233.

[87] K. Fushimi, A. Naganuma, K. Azumi, Y. Kawahara, Corros. Sci., 50 (2008) 903–911.

[88] C. Ren, D. Zeng, J. Lin, T. Shi, W. Chen, Ind. Eng. Chem. Res., 51 (2012) 4894–4904.

[89] S. Wang, H. Ming, J. Ding, Z. Zhang, J. Wang, E.-H. Han, A. Atrens, Corros. Sci., 102 (2016) 469–483.

[90] T.E. Standish, L.J. Braithwaite, D.W. Shoesmith, J.J. Noël, J. Electrochem. Soc., 166 (2019) C3448–C3455.

[91] L. Wu, D. Guo, M. Li, J.M. Joseph, J.J. Noël, P.G. Keech, J.C. Wren, J. Electrochem. Soc., 164 (2017) C539–C553.

Chapter 3. Experimental Techniques

This chapter describes the electrochemical methods and surface and solution analysis techniques used in this thesis. The experimental procedures specific to each chapter are described in the experimental sections of those chapters.

3.1 Electrochemical Tests

3.1.1 Electrochemical cell set-up

The electrochemical tests were performed in a typical three-electrode electrochemical cell which consists of a working electrode (WE), a counter electrode (CE) made of platinum mesh (Alfa Aesar, 99.9% purity) and a reference electrode (RE). The WE was either a CS/SS 304/SS 309 electrode or an electrically connected CS-SS couple. Three types of RE were used in this study: a saturated calomel electrode (SCE) for room temperature experiments, a Ag/AgCl electrode for higher temperatures and a Hg|HgO electrode for irradiation tests. A schematic of the electrochemical cell is shown in Figure 3.1. During electrochemical tests, the cell was connected to a potentiostat so that potential and current passing through the cell could be controlled or monitored. The potential measured is the potential difference between WE and RE. A high impedance voltmeter is contained within the potentiostat circuit connecting the WE and RE to ensure negligible current flow through this external measurement circuit [1]. The current measured is the current flow between WE and CE.

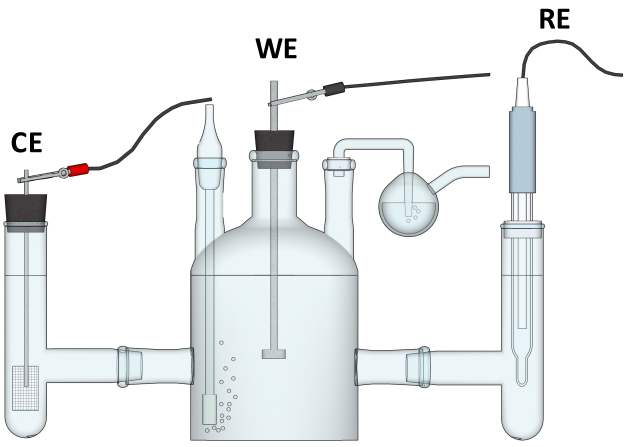

Figure 3.1 Schematic of the three-electrode electrochemical cell.

3.1.2 Potentiodynamic polarization analysis

Potentiodynamic polarization (PD) analysis is widely used to determine the corrosion rate of metals in solutions of interest. It involves polarizing the metal electrode over a potential range around from its E_{corr} (at least ±30 mV), which is often referred to as the Tafel region [2]. The corrosion rate is obtained by extrapolating both the anodic and cathodic regions to E_{corr}.

3.1.3 Linear polarization resistance

Linear polarization resistance (LPR) is often considered a non-destructive technique which involves small potential perturbations near E_{corr}. It is commonly used for the measurement of the charge transfer resistance (R_{P}) of the system. Over a small potential range, the current/applied potential relationship can be approximated as linear. Hence, the observed current and applied potential relationship is analyzed using Ohm's law for LPR [3]. The R_{P} determined by the LPR is assumed to be inversely related to the corrosion rate.

Further derivation of the corrosion rate from R_P requires knowledge of both the anodic and cathodic Tafel slopes based on the Stern–Geary equation.

3.1.4 Cyclic voltammetry

Cyclic voltammetry (CV) is an electrochemical technique that is commonly used to study the redox reactions that occur on the electrode surface as a function of applied potential. In a CV experiment, the potential of the WE is scanned linearly with time from an initial potential (E_initial) to a desired switching potential (E_switch) and then back to the initial potential (E_initial) and the corresponding current response is measured [4]. A typical CV potential waveform is shown in Figure 3.2.

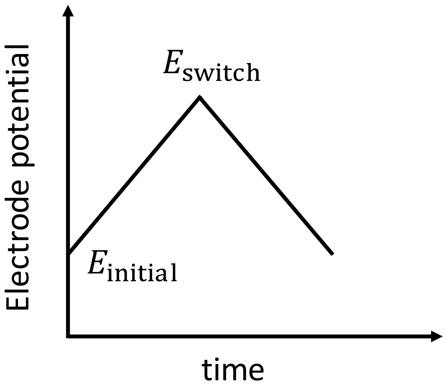

Figure 3.2 Illustration of a triangular potential waveform in a CV experiment.

3.1.5 Coupling potential and coupling current measurements

Coupling potential is the open circuit potential of a galvanic couple and is measured when two metals are electrically connected. Coupling current is the current flow between the two metals when they are electrically connected, which can be measured continuously using a zero resistance ammeter.

3.1.6 Dual-electrochemical cell measurement

A dual-electrochemical cell (DEC) set-up consisting of two identical three-compartment electrochemical cells was also used for the corrosion rate measurement of steels in this thesis. The principle of this DEC set-up is to measure the polarization current continuously when the working electrode in deaerated solutions is polarized to its corrosion potential (E_{corr}) or coupling potential (E_{cpl}) value obtained in aerated solutions [5]. If the contribution of water reduction to the measured polarization current is not significant, the obtained polarization current can then be regarded as the corrosion current of the electrode under aerated conditions.

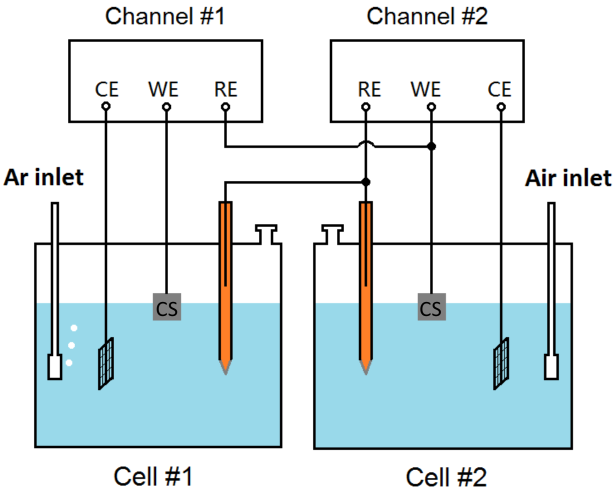

(a)

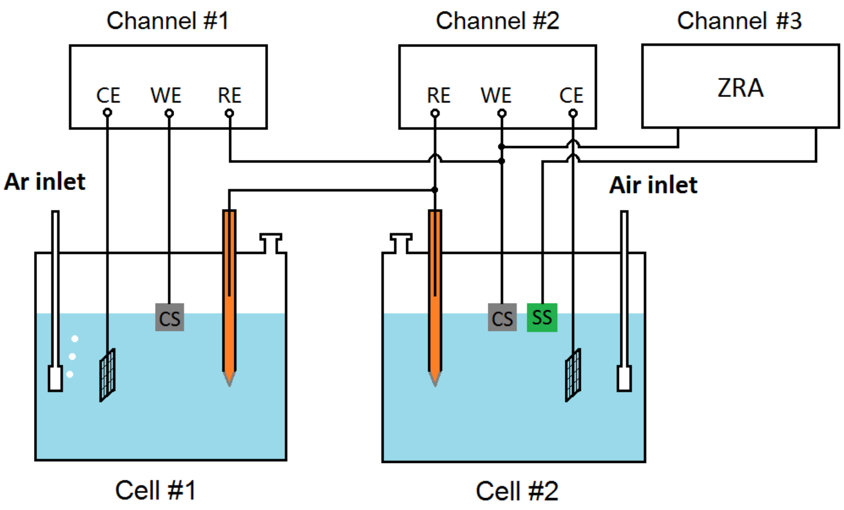

(b)

Figure 3.3 Schematic illustration of the DEC set-up (a) for independent CS/SS corrosion [5] and (b) galvanic corrosion of the CS-SS couple [6].

The schematic illustrations of the set-up for the independent corrosion system and the galvanic corrosion system are shown in Figure 3.3 (a) and (b), respectively. The details of the working, counter and reference electrodes and solutions used are the same as those stated earlier for the traditional three-electrode electrochemical cell.

For an independent corrosion system, two channels of the potentiostat are used. Channel #2 is used to measure the E_{corr} of CS in Cell #2 in air. Simultaneously, the polarization current of an identical CS in Cell #1 is measured using Channel #1 when it is polarized to the E_{corr} of CS in Cell #2. For a galvanically coupled system, the CS in Cell #2 shown in Figure 3.3 (a) is replaced with an electrically connected CS-SS couple and three channels of the potentiostat equipment are used. In this case, the CS in deaerated solutions (Cell #1) is polarized to the E_{cpl} of CS-SS (Cell #2). Channel #2 and Channel #3 are used to measure the E_{cpl} and i_{cpl} of CS-SS couple, respectively, whereas Channel #1 is used for the measurement of the polarization current of CS after coupling. Cell #2 in the DEC set-up functions as a continuous input of E_{corr} or E_{cpl}. This set-up was later simplified to a standard single cell (Cell #1) with a customized input of the electrode potential profile (shown in Figure 3.4), since E_{corr}, E_{cpl} profiles have been recorded previously using conventional electrochemical techniques. This was achieved by directly applying the electrode potential using a step function to approximate the actual potential profiles.

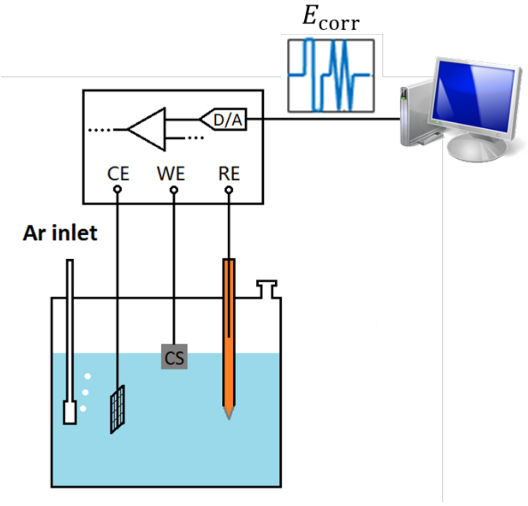

Figure 3.4 Schematic illustration of the simplified DEC set-up.

3.2 Surface Analysis and Solution Analysis Techniques

3.2.1 Comparison of surface analysis techniques

Surface analysis techniques can be divided into two categories: microscopic techniques and spectroscopic techniques. Microscopic techniques are mainly used for characterizing the surface morphology while spectroscopic techniques are mainly used for analyzing the composition of materials. Both techniques have been extensively applied in corrosion studies. Common microscopic techniques include optical microscopy, scanning electron microscopy (SEM), transmission electron microscopy (TEM), scanning tunneling microscopy (STM), and atomic force microscopy (AFM). Common spectroscopic techniques include Raman spectroscopy, energy-dispersive X-ray spectroscopy (EDX), X-ray photoelectron spectroscopy (XPS), Auger electron spectroscopy (AES), and secondary ion mass spectroscopy (SIMS).

In this study, microscopic techniques (optical microscopy and SEM) and spectroscopic techniques (Raman spectroscopy) were used together for the characterization of the morphologies of the metal surface and the composition of the metal oxides formed on the surface after electrochemical tests or corrosion tests.

3.2.1.1 Scanning electron microscopy (SEM)

Scanning electron microscopy (SEM) was used to provide post-test imaging of the sample surfaces. In this technique a high resolution beam of electrons (incident electrons) is directed onto the sample surface. These incident electrons can interact with the atoms in the top few nanometers of the sample surface and eject further electrons, which are referred to as secondary electrons. The intensity of these secondary electrons is measured using a detector to produce an image [7]. SEM is usually used when a higher resolution image is required. However, it is expensive and has strict requirements for the size of the solid sample due to the relatively small size of the vacuum chamber.

3.2.1.2 Optical microscopy

Optical microscopy is used for the examination and analysis of surface morphologies, using reflected visible light magnified using glass optics. The resolution of images taken by optical microscopes cannot compete with SEM. However, the colours of the oxides on the electrode surface, which often indicate their compositions, can be captured by the optical microscope. Optical microscopes do not need to be operated in a vacuum environment, and therefore this technique is less destructive to samples with loose oxides on the surfaces. Optical microscopes are also much cheaper and easier to operate and maintain than scanning electron microscopes. Therefore, when a higher magnification is not required, it is more convenient and cost-effective to examine the electrode surface using an optical microscope.

3.2.1.3 Raman spectroscopy

Raman spectroscopy is a qualitative surface characterization tool. Raman spectra are acquired by irradiating a sample with a powerful laser source of visible or near-infrared monochromatic light. Once irradiated, molecules can scatter the light elastically or inelastically [8]. Most of the radiation is scattered elastically while a small portion is inelastically scattered. With inelastic scattering, the energy of the incident light will lose energy to molecular vibrations resulting in a shift in wavenumber which is called Raman shift. The shift contains information about the vibrational modes of the system. Each molecule has characteristic Raman shifts. Therefore, Raman spectroscopy is commonly used to analyze the chemical composition of oxides in corrosion studies. The penetration depth of Raman spectroscopy is usually a few microns [9].

3.2.2 Inductively coupled plasma optical emission spectrometry

Inductively coupled plasma optical emission spectrometry (ICP-OES) is an analytical technique used for the detection of chemical elements, particularly in aqueous samples. In this technique, an inductively coupled plasma (ICP) works as the ionization source and produces excited atoms or ions that emit electromagnetic radiation at wavenumbers characteristic of a particular element. Typically, argon gas is used to create the plasma. The photons emitted at different wavelengths are then detected and identified using a spectrometer. With calibration curves from standard samples, the collected photon intensity can be converted into a concentration unit [10]. A simplified schematic diagram of a typical ICP-OES is shown in Figure 3.5 [11]. The detection limit of the ICP-OES (Perkin Elmer) used in our lab is 1ppb (µg/L).

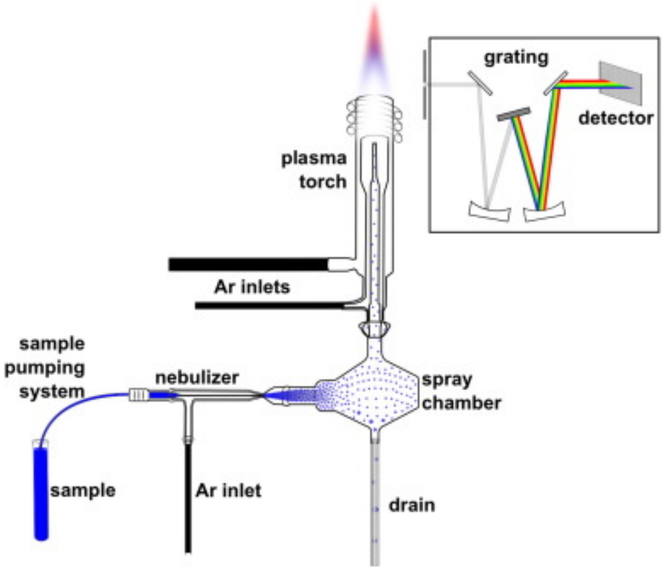

Figure 3.5 A simplified schematic diagram of an ICP-OES instrument.

3.3 References

[1] R.G. Kelly, J.R. Scully, D.W. Shoesmith, R.G. Buchheit, Electrochemical Techniques in Corrosion Science and Engineering, CRC Press, 2002.

[2] A.J. Bard, L.R. Faulkner, Electrochemical Methods Fundamentals and Applications, 2nd ed., John Wiley & Sons, Inc., 2001.

[3] F. Mansfeld, The Polarization Resistance Technique for Measuring Corrosion Currents, in: M.G. Fontana, Roger W. Steale (Eds.), Advances in Corrosion Science and Technnology Volume 6, Plenum Press, New York and London, 1976, pp. 163–262.

[4] P.T. Kissinger, W.R. Heineman, J. Chem. Educ., 60 (1983) 702–706.

[5] D. Guo, Corrosion Dynamics of Carbon Steel in Used Fuel Container Environments, The University of Western Ontario, London, ON, 2018.

[6] M. Li, D. Guo, J.M. Joseph, O. Yong, J.C. Wren, Galvanic Corrosion of Carbon Steel and Stainless Steel Couples: Effects of γ-Radiation and Solution Environment, in: WM2020 Conference, Phoenix, AZ, 2020.

[7] V. Kazmiruk, Scanning Electron Microscopy, IntechOpen, 2012.

[8] D.A. Long, Raman spectroscopy, McGraw-Hill, New York, 1977.

[9] L. Opilik, T. Schmid, R. Zenobi, Annu. Rev. Anal. Chem., 6 (2013) 379–398.

[10] C.B. Boss, K.J. Fredeen, Concepts, Instrumentation and Techniques in Inductively Coupled Plasma Optical Emission Spectrometry, 3rd ed., PerkinElmer, Inc., 2004.

[11] F. Caruso, S. Mantellato, M. Palacios, R.J. Flatt, Cem. Concr. Res., 91 (2017) 52–60.

Chapter 4. Effect of Solution Properties on the Independent Corrosion of Individual Carbon Steel and Stainless Steel

4.1 Introduction

As described in Chapter 1, the weld region consists of three types of metals: carbon steel (CS), stainless steel (type 304L, SS 304) and the stainless steel filler material (type 309, SS 309). Due to their direct electrical contact, galvanic corrosion of both the CS-SS 309 couple and the SS 304-SS 309 couple can occur. To study how significant the galvanic effect is, a solid understanding of the corrosion dynamics of the metals when they corrode independently and while galvanically coupled is needed. Access to the annular air gap in the end shield cooling system (ESC) is limited and the actual solution environment at the local weld region is not known. The pH of the ESC water is 10.4±0.2, but the pH at the weld region could be lower due to the presence of HNO_3 produced by humid air radiolysis. This would in turn alter the dissolution rates of the metals involved. This factor, as well as possible changes in the temperature, can affect the rate of corrosion. The objective of this chapter is to determine the effect of solution properties (pH and temperature) on the corrosion dynamics of the individual alloys involved. A series of electrochemical tests were carried out, including corrosion potential (E_{corr}), linear polarization resistance (LPR) and potentiodynamic polarization (PD) measurements. The dual-electrochemical cell (DEC) method for corrosion rate measurement is introduced. The rate measured using the DEC method was compared with those obtained using the LPR and PD methods. The corrosion current results were also compared with the solution and surface analyses data.

4.2 Experimental

4.2.1 Electrode and solution preparation

Three types of steel specimen were supplied by Ontario Power Generation, and the detailed chemical compositions are listed in Table 4.1. A three-electrode cell, consisting of a reference electrode (RE), a Pt mesh counter electrode (CE) and a metal working electrode (WE), was used for the electrochemical studies. The exposed surface areas of the CS/SS 304 and SS 309 metal working electrodes were limited to 0.455 cm^2 and 1.267 cm^2 respectively by covering the surrounding areas with Teflon tape. Prior to each test, the coupon was abraded successively with 1200 and 2500 grit SiC paper followed by polishing on a Texmet microcloth (Buehler) with a 1 μm MetaDi Supreme diamond paste suspension (Buehler) to obtain a mirror-like surface. All exposed surfaces of coupons were immersed in 0.01 M aerated borate buffer solutions prepared using reagent grade $Na_2B_4O_7 \cdot 10\ H_2O$ (EMD Millipore Corporation). Solution pHs were adjusted to 6.0 or 10.6 either by adding reagent grade H_3BO_3 or 2 M NaOH solution (Caledon Laboratories Ltd.) to the borate solutions. Solutions were prepared with water purified using a NANOpure Diamond UV ultra-pure water system (Barnstead International) to give a resistivity of 18.2 MΩ·cm. The solution volume used in all tests was 0.5 L.

A saturated calomel electrode (SCE) (Fisher Scientific) was used for experiments carried out at 21 °C and 50 °C, whereas an Ag/AgCl electrode was employed for experiments conducted at 80 °C due to its stability at high temperatures. The temperature of the test solution was maintained at 50 °C or 80 °C by circulation of heated water through the dual-walled cell body of the electrochemical cell. A water bath with thermostat control (Fisher Scientific) was used to control the temperature.

Table 4.1. Chemical compositions in wt.% of alloys in this study.

Material	**Cr**	**Ni**	**C**	**Mn**	**Mo**	**Si**	**S**	**P**	**Fe**
CS SA36	0.16	0.23	0.15	0.84	0.03	0.24	0.03	0.02	Bal.
SS 304L	18.8	8.2	0.02	2.0	-	0.35	0.003	0.02	Bal.
Weld metal SS 309	24	14	0.03	1.2	0.10	0.63	0.005	0.02	Bal.

4.2.2 Electrochemical tests

The electrochemical tests were conducted using a BioLogic VMP-300 multichannel potentiostat. Two sets of measurements were performed. In the first set, E_{corr} was monitored for 0.5, 2, 20 or 72 h and this was followed by a PD measurement from (E_{corr} – 0.3 V) to 0.5 V_{SCE} at a scan rate of 1 mV/s. Prior to the E_{corr} measurement, the electrode was subjected to 5-min cathodic cleaning at −1.1 V_{SCE}. In the second set, the E_{corr} measurement was interrupted periodically (every 2 h) to perform linear polarization resistance measurements. The potential for each measurement was scanned from E_{corr} to ($E_{\text{corr}} - 10$ mV), to ($E_{\text{corr}} + 10$ mV) and then back to E_{corr} at a scan rate of 0.167 mV/s. Each LPR measurement took ~ 4 min.

4.2.3 The dual-electrochemical cell method

As the name suggests, the DEC method uses two electrochemical cells. The DEC set-up is schematically illustrated in Figure 4.1. Cell#1 and Cell#2 are standard three-electrode electrochemical cells of the type commonly used in corrosion studies. The electrodes were the WE made of the alloy of interest (CS in this work). The RE is either an SCE or an Ag/AgCl electrode while the CE is a Pt mesh. The electrolyte was the solution of interest (aerated pH 6.0 borate buffer in this work). Electrical connection of the three electrodes was made through channel #2 of a multichannel potentiostat. The CS in Cell#2 was left at open circuit and its corrosion potential ($E_{\mathrm{corr\#2}}$) was measured.

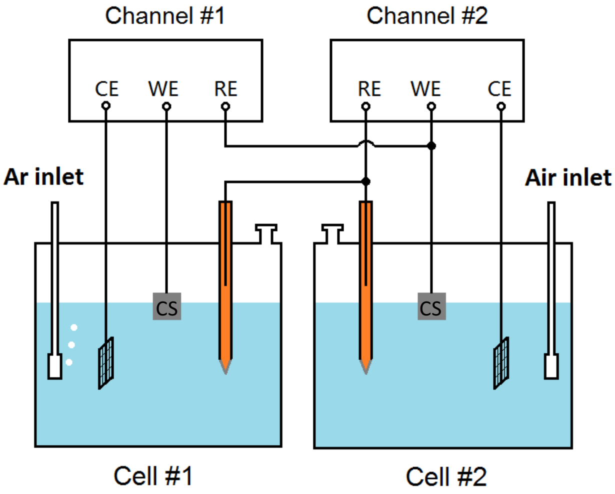

Figure 4.1 Schematic of the dual-electrochemical cell (DEC) set-up [1].

The electrolyte solution in Cell#1 was the same as that of Cell#2, except that it was free of the oxidant of interest (dissolved O_2 in this work). Cell#1 was electrically configured slightly differently from Cell#2. The RE in Cell#1 was connected to the RE in Cell#2. The RE lead of Channel #1 of the potentiostat was connected to the CS in Cell#2, and the electrode potential of CS in Cell#1 was maintained at 0 V with respect to $E_{\mathrm{corr\#2}}$. With this configuration the applied potential (E_{appl}) of the CS in Cell#1 exactly followed $E_{\mathrm{corr\#2}}$, and the polarization current of Cell#1 (i_{meas}) was recorded simultaneously. The electrical connections used a floating ground to avoid ground loops.

With the DEC set-up, the i_{meas} represents ($i_{\mathrm{ox}} - |i_{\mathrm{red\#1}}|$) at $E_{\mathrm{corr\#2}}$. The reduction current in Cell#1 ($|i_{\mathrm{red\#1}}|$) arises from the reduction of H^+, while the reduction current in Cell#2 ($|i_{\mathrm{red\#2}}|$) is mainly due to the reduction of O_2, as the O_2 reduction current is typically much larger than the proton reduction current; $|\mathrm{i}_{\mathrm{red\#2}}| \gg |i_{\mathrm{red\#1}}|$ at $E_{\mathrm{corr\#2}}$. Hence, the current measured in Cell#1 is approximately equal to the metal oxidation current or corrosion current for CS in aerated solution:

$$i_{\mathrm{meas}}|_{E=E_{\mathrm{corr\#2}}} = i_{\mathrm{ox}} - \left|i_{\mathrm{H^+/H_2}}\right| \approx i_{\mathrm{ox}} = i_{\mathrm{corr}} \qquad (4.1)$$

In equating i_{meas} to i_{corr} it is assumed that the rate of the metal oxidation half-reaction in Cell#1 is the same as that in Cell#2 at any given time.

4.2.4 Corrosion tests

The set-up of the corrosion tests was the same as for the electrochemical tests. After 5-min cathodic cleaning at −1.1 V_{SCE}, coupons were left at open circuit conditions. In this work, corrosion tests were conducted at three temperatures: 21 °C, 50 °C and 80 °C.

4.2.5 Surface characterization and solution analysis

After individual CS, SS 304 and SS 309 electrodes had corroded for different durations, their surfaces were dried with Ar. The surfaces were then analyzed by scanning electron microscopy (SEM). The dissolved iron concentration in the solution after each test was analyzed using a Perkin Elmer Avio 200 inductively coupled plasma optical emission spectrometer (ICP-OES). Prior to the solution analysis the samples were digested using nitric acid (trace analytical grade, Fisher Scientific) to dissolve any colloidal particles in solution. Therefore, the measured dissolved iron concentration may include any colloid particles, if present.

4.3 Results and Discussion

4.3.1 Effect of pH and temperature on the corrosion of individual alloys

The time-dependent behaviours of E_{corr} monitored during the independent corrosion of the CS, SS 304 and SS 309 electrodes are presented in Figure 4.2. The E_{corr} profiles all show three distinct stages: an initial sharp transient increase from the initial potential of −1.1 V_{SCE} (applied for cathodic cleaning) to a value that depends on the alloy and corrosion environment (pH and temperature), followed by a slower increase or decrease with time, and finally the reaching of a steady state. Upon removal of the applied potential at −1.1 V_{SCE}, metal oxidation (coupled with solution reduction) will begin. The E_{corr} reached within a short time (< 1 h) is determined by the rate of metal oxidation on the original alloy surface. The slow change in E_{corr} that follows is due to a slow change of the surface, and the rate of change of E_{corr} and the final E_{corr} reached depend on the solution temperature and pH.

The solution pH affects the E_{corr} of CS more than that of SS. The final E_{corr} value at pH 6.0 ranges from –0.7 to –0.6 V_{SCE} depending on temperature. At pH 10.6, it is about 0.6 V higher, ranging from –0.2 to 0.0 V_{SCE}. The effect of pH on SS 304 and SS 309 is less pronounced. On these alloys, the final E_{corr} values at pH 10.6 are lower than those at pH

6.0. This observation is consistent with the expectation of a lower E_{corr} at a higher pH because of E_{eq} dependence on pH (assuming that mass transport is not rate determining); see discussion further below.

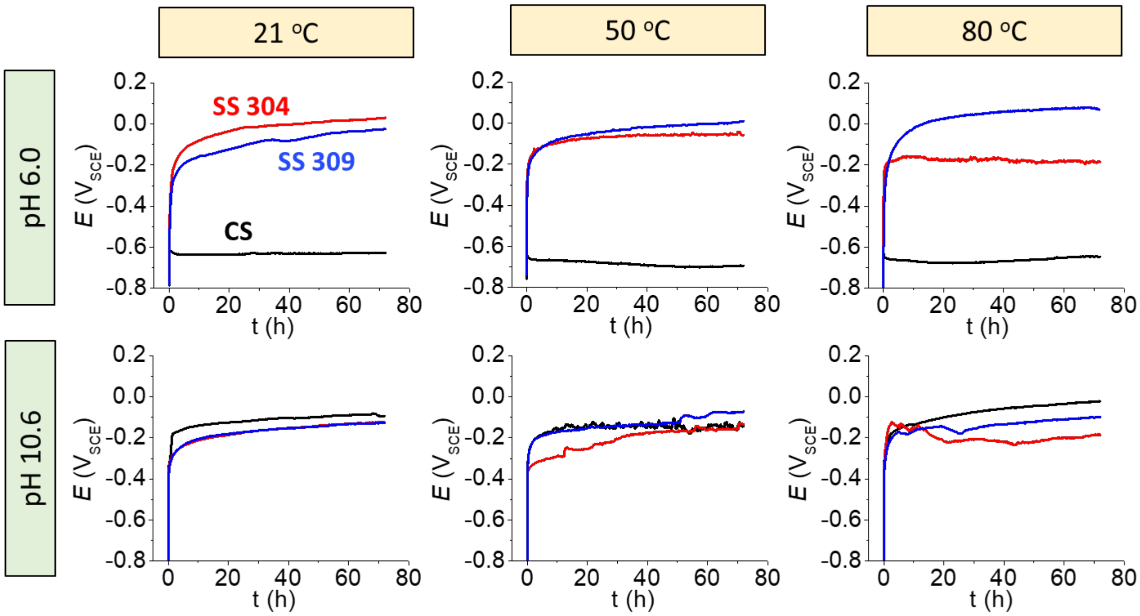

Figure 4.2 E_{corr} measured as a function of time during the independent corrosion of CS, SS 304 and SS 309 in aerated solutions at pH 6.0 and 10.6 and at 21 °C, 50 °C and 80 ºC.

Temperature has the opposite effect on SS 309 corrosion to that on SS 304 corrosion. At pH 6.0, the initial rate of increase of E_{corr} on SS 309 is higher at a higher temperature. The final steady-state E_{corr} increases the most when temperature increases from 50 °C to 80 °C. As observed for CS, temperature has a negligible effect on E_{corr} at pH 10.6. For SS 304 corrosion at pH 6.0, temperature has a negligible effect on the initial E_{corr} but increasing temperature lowers the rate of increase of E_{corr} and hence the final E_{corr}. On the other hand, temperature affects the initial E_{corr} on SS 304 at pH 10.6. The initial E_{corr}

at 50 °C is lower than at 21 °C but the initial E_{corr} at 80 °C is higher. At 50 °C E_{corr} continues to increase over 72 h whereas at 80 °C E_{corr} decreases for a while before it reaches steady state.

The change in the corrosion rate can be monitored using linear polarization resistance measurements. This can help understand the corrosion (or oxide formation) evolution in more depth.

Polarization resistance (R_{P}) is defined as the current response to a potential change.

$$R_{\text{P}} = \frac{\mathrm{d}E}{\mathrm{d}i} \tag{4.2}$$

The polarization resistance was determined from the slopes of the linear region of the current-potential plot during the forward and reverse scans. The reciprocal of R_{P} ($\mathrm{d}i/\mathrm{d}E$) is proportional to the corrosion rate according to the Stern-Geary equation [2].

$$i_{\text{corr}} = \frac{b_{\text{a}} b_{\text{c}}}{2.303(b_{\text{a}} + b_{\text{c}})R_{\text{P}}} = \frac{B}{R_{\text{P}}} \tag{4.3}$$

where b_{a} and b_{c} are the Tafel slopes of the anodic and cathodic reactions, respectively. However, it should be noted that this relationship is only valid when both the anodic and cathodic reactions follow the Tafel equation.

For individual alloys under all conditions of pH and temperature, no significant difference could be observed between the forward and backward scans of the polarization resistance over 72 h (Figure 4.3). At both pHs, $1/R_{\text{P}}$ of each individual alloy increases with increasing temperature. This result indicates a faster corrosion rate at higher temperatures assuming that both the anodic and cathodic reactions follow the Tafel equation and that the value of B remains unchanged over time. For CS, $1/R_{\text{P}}$ differs significantly between pH

6.0 and pH 10.6. However, for both SS 304 and SS 309, $1/R_P$ shows no pH dependence at all temperatures.

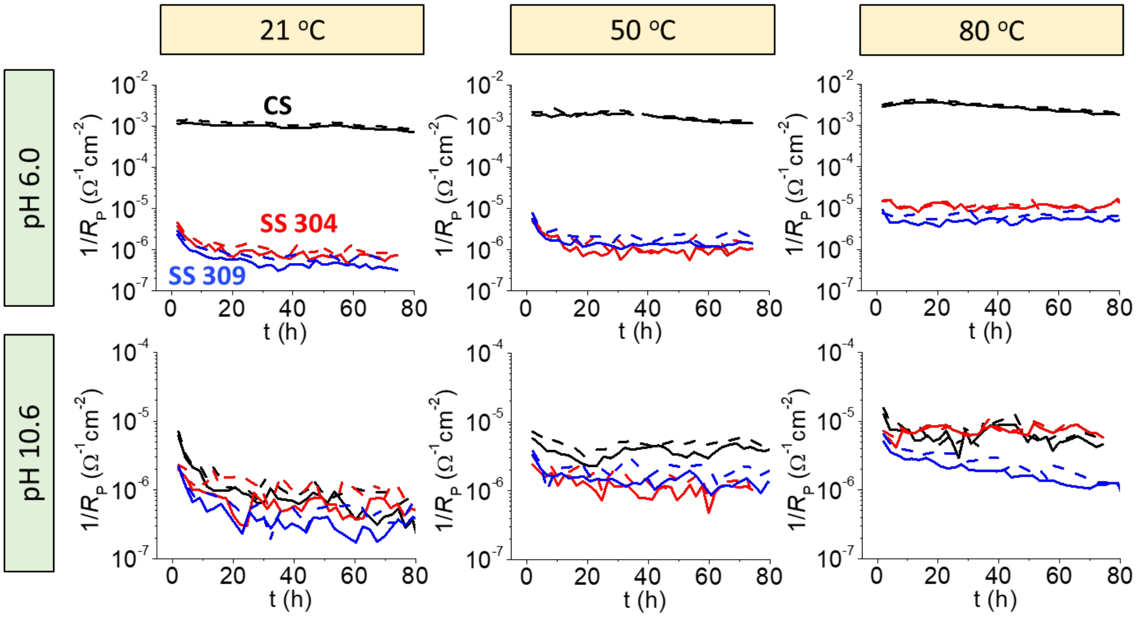

Figure 4.3 $1/R_P$ as a function of time obtained at E_{corr} ± 10 mV for three alloys. The values of $1/R_P$ obtained during the forward and backward scans are indicated by the solid lines and dashed lines, respectively.

Corrosion is an interfacial mass and charge transfer process, involving metal oxidation coupled with the reduction of solution species, interfacial transfer of ions and electrons, mass transport of metal cations from the metal surface to the bulk solution and mass transport of dissolved oxidants from the bulk solution to the metal surface. The thermodynamic driving force for corrosion is the difference between the equilibrium potentials (E_{eq}) of solution reduction half-reaction(s) (E_{eq}^{red}) and metal oxidation half-reaction(s) (E_{eq}^{ox}) [3]. Corrosion potential is the potential of a naturally corroding system.

Because mass and charge must be conserved during corrosion (or any chemical reaction), the rate of metal oxidation (or anodic current) equals the rate of solution reduction (or cathodic current) at E_{corr}:

$$\sum i_{\mathrm{a}} = -\sum i_{\mathrm{c}} \quad \text{at } E_{\mathrm{corr}} \tag{4.4}$$

The thermodynamic driving force for oxidation and reduction half-reactions are the differences between E_{corr} and their E_{eq}, known as overpotential (η):

$$\eta_{\mathrm{ox}} = E_{\mathrm{corr}} - E_{\mathrm{eq}}^{\mathrm{ox}} \tag{4.5}$$

$$\eta_{\mathrm{ox}} = E_{\mathrm{corr}} - E_{\mathrm{eq}}^{\mathrm{ox}} \tag{4.6}$$

$$\eta_{\mathrm{red}} = E_{\mathrm{eq}}^{\mathrm{red}} - E_{\mathrm{corr}} \tag{4.7}$$

Generally, a more oxidizing solution environment results in a higher E_{corr} value. Additionally, an oxide layer present on the surface can also cause an increase in E_{corr} since it is a potential barrier for interfacial transfer of ions and electrons [4,5]. Oxide present on the surface has a stronger effect on the transfer of massive ions than on electron transfer. Thus, as an oxide layer forms and grows a higher overpotential is required for metal oxidation than for solution reduction. Thus, in the presence of an oxide layer the metal oxidation rate may slow down but the E_{corr} increases. The oxide layer may be pre-formed or formed during corrosion. The magnitude of the potential barrier depends on the charge transfer properties and the thickness of the oxide.

There is more than one reduction reaction and more than one metal oxidation reaction that can occur during corrosion of the steel alloys in aerated solutions. The solution reduction reaction could involve both H_2O and dissolved O_2. For alloys containing Fe, Cr and Ni, each metal can undergo multiple oxidation reactions, forming different oxides on the surface. This is well demonstrated by the corrosion mechanism of CS [1] shown in

Figure 4.4. As shown in the figure, CS corrosion evolves through different dynamic stages: Stage 1, Stage 2 and Stage 3. In Stage 1, the metal surface is not covered with oxide deposits and the corrosion dynamics are determined mainly by the electrochemical reaction of base metal Fe with oxidants to produce $Fe^{II}_{(aq)}$ at the metal surface, followed by transport of $Fe^{II}_{(aq)}$ from the metal surface to the bulk solution. The main corrosion product is the dissolved Fe^{II} and its dissolution rate is nearly independent of pH. As corrosion progresses, the concentration of $Fe^{II}_{(aq)}$ increases and approaches its saturation limit near the metal surface. The volume of the $Fe^{II}_{(aq)}$-saturated solution also expands and the hydrolysis of $Fe^{II}_{(aq)}$ occurs at an increased rate. The Fe^{II} in the form of $Fe(OH)_2$ can be further oxidized to ferric species, leading to the formation and growth of a mixed Fe^{II}/Fe^{III} hydroxide gel near the metal surface. The hydroxide gel is viscous and can significantly affect the further transport of $Fe^{II}_{(aq)}$ produced at the metal surface to the bulk solution and the transport of O_2 in the opposite direction. In Stage 2, the amount of mixed Fe^{II}/Fe^{III} hydroxide gel and the ratio of $Fe^{II}_{(gel)}$ to $Fe^{III}_{(gel)}$ in the gel layer reach steady state. Depending on the ratio of Fe^{II}/Fe^{III} in the mixed hydroxide gel, the formation of thermodynamically stable ferric oxyhydroxides and oxides (Fe_3O_4 and γ-Fe_2O_3) that are less soluble than the initially produced $Fe(OH)_2$ can occur on the surface. The production rates of oxides and hydroxides are strongly influenced by solution parameters and transport dynamics. In Stage 3, the net metal oxidation is negligible but the oxide phase transformation continues.

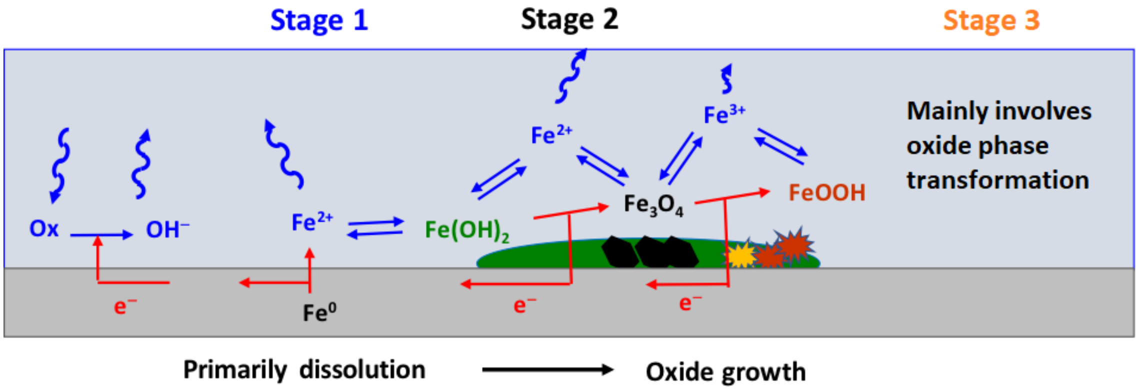

Figure 4.4 Schematic of the reaction mechanism for oxide layer evolution in aerated solution [1].

The corrosion mechanism for SS is similar to that for CS except that additional oxidation reactions of Cr and Ni are involved. For example, the corrosion mechanism for Alloy 800 [6], which is a type of Fe-Cr-Ni alloy, is given in Figure 4.5. Depending on the competition kinetics of different oxidation reactions, solution reactions and transport dynamics, the corrosion pathway can vary.

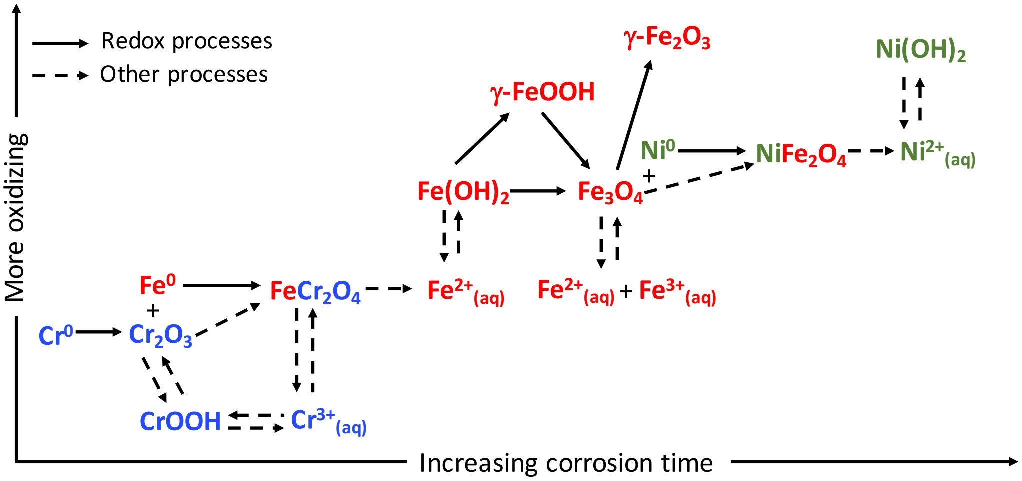

Figure 4.5 Proposed mechanism for Alloy 800 corrosion [6].

For oxidation of a particular metal to occur, the E_{corr} of the corroding system must be higher than the E_{eq} of the metal's oxidation reaction (Equation 6). Therefore, in Figure 4.6, we compared the observed E_{corr} values with the E_{eq} values in order to identify the possible oxidation reactions that could occur on steel alloys. The E_{eq} values for different metal oxidation reactions on steels at 21 °C were calculated from the known standard redox potentials ($E°$) [7]. The values of E_{eq} at both pH 6.0 and pH 10.6 are listed in Table 4.2 since they are pH dependent. Temperature is expected to have no significant effect on E_{eq} within the studied range. The values of $E_{\mathrm{eq}}(\mathrm{Fe}^0 \rightleftharpoons \mathrm{Fe}^{2+}{}_{(aq)})$, $E_{\mathrm{eq}}(\mathrm{Ni}^0 \rightleftharpoons \mathrm{Ni}^{2+}{}_{(aq)})$ and $E_{\mathrm{eq}}(\mathrm{Cr}^0 \rightleftharpoons \mathrm{Cr}^{3+}{}_{(aq)})$ are not indicated in the E_{eq} diagram as they depend on the concentration of the metal cations at the metal-solution interface and the concentration changes with time. That is, the oxidation of Cr^0, Ni^0, and Fe^0 can occur at a much lower electrode potentials than those indicated in the E_{eq} diagram.

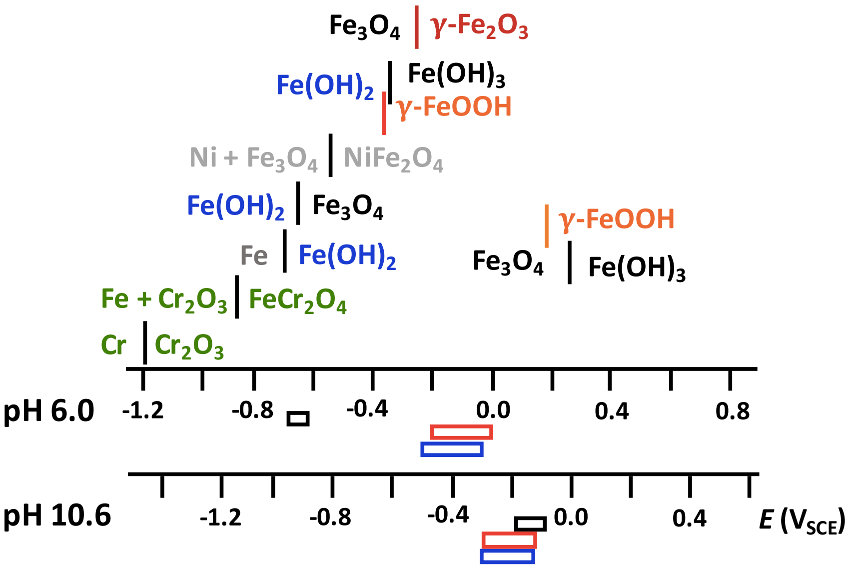

Figure 4.6 Redox reactions of metals and metal oxides that can occur on the steel alloys, and their E_{eq} values at 21 °C. The positions of E_{eq} are indicated using bars with the corresponding redox pairs listed on either side of these bars. Two scales for the potential axis are shown at the bottom, one for pH 6.0 and the other for pH 10.6, since the E_{eq} at different pHs differ by –59 mV/pH. The thick black, red and blue boxes next to the potential scales represent the ranges of E_{corr} observed during 72-h corrosion of CS, SS 304 and SS 309 at corresponding pHs.

Table 4.2. Standard potentials [7] and the equilibrium potentials for redox reactions of Fe, Ni and Cr metals and oxides at pH 6.0 and pH 10.6.

Redox Reaction	**Standard potential (V_{SHE})**	**E_{eq} at pH 6.0 (V_{SCE})**	**E_{eq} at pH 10.6 (V_{SCE})**
$Cr_2O_3 + 6H^+ + 6e^- \rightleftharpoons 2Cr + 3H_2O$	-0.59	-1.19	-1.46
$FeCr_2O_4 + 2H^+ + 2e^- \rightleftharpoons Fe + Cr_2O_3 + H_2O$	-0.29	-0.88	-1.16
$Fe(OH)_2 + 2H^+ + 2e^- \rightleftharpoons Fe + 2H_2O$	-0.092	-0.687	-0.959
$Fe_3O_4 + 2H^+ + 2e^- \rightleftharpoons Fe(OH)_2 + H_2O$	-0.064	-0.659	-0.931
$3NiFe_2O_4 + 8H^+ + 8e^- \rightleftharpoons 3\,Ni + 2Fe_3O_4 + 4\,H_2O$	0.074	-0.52	-0.79
$\gamma\text{-}FeOOH + H^+ + e^- \rightleftharpoons Fe(OH)_2 + H_2O$	0.22	-0.375	-0.647
$Fe(OH)_3 + H^+ + e^- \rightleftharpoons Fe(OH)_2 + H_2O$	0.247	-0.348	-0.62
$3\gamma\text{-}Fe_2O_3 + 2H^+ + 2e^- \rightleftharpoons 2Fe_3O_4 + H_2O$	0.374	-0.221	-0.493
$3\gamma\text{-}FeOOH + H^+ + e^- \rightleftharpoons Fe_3O_4 + 2H_2O$	0.789	0.194	-0.078
$3Fe(OH)_3 + H^+ + e^- \rightleftharpoons Fe_3O_4 + 5H_2O$	0.867	0.272	0

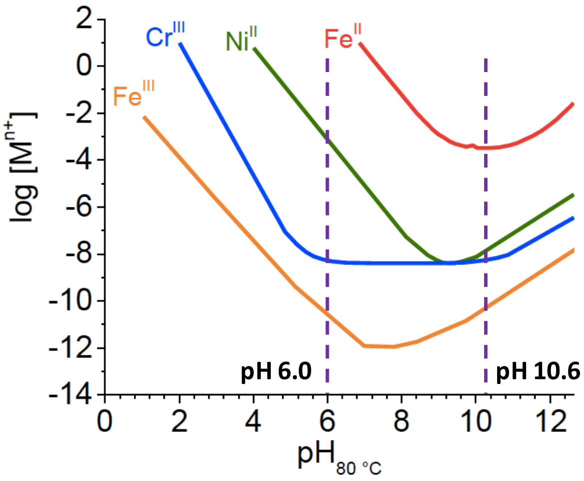

Figure 4.7 The solubility of Fe^{II}, Fe^{III}, Cr^{III} and Ni^{II} species as a function of pH at 80 °C [6,8].

For CS, the E_{corr} at pH 6.0 is low (–0.6 V_{SCE}), and it changes slightly with time. The value of E_{corr} lies not far above $E_{\mathrm{eq}}(\mathrm{Fe^0} \rightleftharpoons \mathrm{Fe(OH)_2})$ and $E_{\mathrm{eq}}(\mathrm{Fe(OH)_2} \rightleftharpoons \mathrm{Fe_3O_4})$. As presented in Figure 4.7, the solubility of $\mathrm{Fe^{II}}$ is much higher at pH 6.0 than at pH 10.6. The transport of $\mathrm{Fe^{II}}$ from the surface to the bulk solution is also faster at pH 6.0 due to a larger concentration gradient. As a result, it takes longer for $\mathrm{Fe^{II}}$ species to reach their saturation limit near the metal surface at pH 6.0, resulting in a longer duration for Stage 1. As a result, the subsequent formation of $\mathrm{Fe^{II}}$ and/or mixed $\mathrm{Fe^{II}}/\mathrm{Fe^{III}}$ oxide/hydroxide occur at a much later time at this pH. As mentioned earlier, the $\mathrm{Fe^{II}}/\mathrm{Fe^{III}}$ hydroxide gel has a strong influence on the transport of $\mathrm{Fe^{II}}_{(aq)}$ produced at the metal surface to the bulk solution. Therefore, the rate-determining step (RDS) for further metal oxidation switches from electron transfer to mass transport of $\mathrm{Fe^{II}}_{(aq)}$. This is consistent with the observation that E_{corr} remains close to $E_{\mathrm{eq}}(\mathrm{Fe^0} \rightleftharpoons \mathrm{Fe(OH)_2})$ and $E_{\mathrm{eq}}(\mathrm{Fe(OH)_2} \rightleftharpoons \mathrm{Fe_3O_4})$. At pH 6.0. the E_{corr} of CS decreases initially and increases at later times and this change in E_{corr} accelerates with increasing temperature. The $1/R_{\mathrm{P}}$ also decreases earlier at a higher temperature (Figure 4.3). These observations indicate that CS corrosion progresses to Stage 2 faster at a higher temperature. This can be attributed to the effect of temperature on the dissolution and transfer rate of $\mathrm{Fe^{2+}}$ and on magnetite ($\mathrm{Fe_3O_4}$) growth.

At pH 10.6, the E_{corr} of CS is almost 0.5 V higher than that at pH 6.0. Due to a much lower solubility of $\mathrm{Fe^{II}}$ and slower transport of $\mathrm{Fe^{II}}$ from the surface to the bulk solution at pH 10.6 than pH 6.0, Stage 2 and Stage 3 are quickly reached. The values of E_{corr} during CS corrosion at pH 10.6 are above $E_{\mathrm{eq}}(\mathrm{Fe_3O_4} \rightleftharpoons \gamma\text{-}\mathrm{Fe_2O_3})$ but near $E_{\mathrm{eq}}(\mathrm{Fe_3O_4} \rightleftharpoons \gamma\text{-}\mathrm{FeOOH})$ and $E_{\mathrm{eq}}(\mathrm{Fe_3O_4} \rightleftharpoons \mathrm{Fe(OH)_3})$. These E_{corr} values are slightly higher than those observed for SS 304 and SS 309. Figure 4.3 shows that the $1/R_{\mathrm{P}}$ values as a function of time for CS at pH 10.6 are three orders of magnitude lower than at pH 6.0. These results indicate that corrosion of CS at pH 10.6 leads to the formation of more protective oxides (e.g. γ-Fe_2O_3), which is consistent with previous studies [9–11].

The E_{corr} observed at pH 6.0 is significantly higher for SS 304 and SS 309 than for CS (Figure 4.2). This difference can be attributed to the presence of a preformed Cr_2O_3 layer on SS 304 and SS 309. The presence of Cr_2O_3 is a huge potential barrier and it can significantly lower the interfacial metal oxidation rate (e.g. $Fe^0 \rightleftharpoons Fe^{2+}$ and $Ni^0 \rightleftharpoons Ni^{2+}$). Although the oxidation rate of Fe^0 to Fe^{2+} is low, as Fe^{2+} is continuously produced, it can react with Cr_2O_3 forming $FeCr_2O_4$. When the electrode potential increases, the oxidation of Ni^0 to Ni^{2+} can occur, but also at a low rate due to the potential barriers of Cr_2O_3 and $FeCr_2O_4$. Once the Fe^{II} and Ni^{II} species are produced at the metal surface they can continuously dissolve out and be transported away to the bulk solution. As shown in Figure 4.7, the solubility of Fe^{II} and Ni^{II} is much higher at pH 6.0 than at pH 10.6. Therefore, similar to CS corrosion at pH 6.0, metal dissolution (Fe^{II} and Ni^{II}) from SS 304 and SS 309 at this pH occurs readily for a long time before the saturation limit of these species is reached and hydroxide and oxide formation becomes dominant. In comparison, the saturation limits of Fe^{II} and Ni^{II} are quickly reached at pH 10.6 and this leads to faster formation of their hydrolysis and oxide products. By comparing the obtained E_{corr} values with the E_{eq} diagram, the oxide layer on SS 304 and SS 309 at pH 10.6 could be a mixed Cr_2O_3 / $FeCr_2O_4$ / Fe_3O_4 / $NiFe_2O_4$ / $Ni(OH)_2$ / γ-Fe_2O_3 layer. This is similar to our previous observations for the Fe-Ni-Cr alloys [7].

The corrosion pathways for SS 304 and SS 309 discussed above are consistent with the polarization resistance results (Figure 4.3) which show that the $1/R_{\mathrm{P}}$ values of SS 304 and SS 309 are two or three orders of magnitude lower than that of CS at pH 6.0, and are as low as that of CS at pH 10.6. This is further supported by the solution analysis results (not presented) which show that the dissolved amounts of Fe^{II} and Ni^{II} from SS 304/SS 309 after 72-h corrosion at pH 6.0 are two or three orders of magnitude lower than the dissolved Fe^{II} amount from CS. The dissolved amounts of Fe^{II} and Ni^{II} from SS 304/SS 309 are also higher at pH 6.0 than at pH 10.6 and this difference ranges from a factor of 2 to 10 depending on the alloy and the temperature.

The potentiodynamic polarization curves for all alloys after the 72-h E_{corr} measurement are shown in Figure 4.8. Conventionally, corrosion current (i_{corr}) can be obtained by extrapolating both the anodic and cathodic Tafel regions to the E_{corr} [12]. The polarization potential at which the net current is zero ($E_{i=0}$) should be the E_{corr}. However, except for CS at pH 6.0, the $E_{i=0}$ observed during the potentiodynamic polarization deviates from its E_{corr} prior to the polarization scan (or the final E_{corr} at 72 h shown in Figure 4.2). In most cases, the $E_{i=0}$ values are below the final E_{corr} values at 72 h before the polarization scan. For example, at pH 6.0 and 21 °C, the $E_{i=0}$ observed on SS 309 in the potentiodynamic polarization curve is –0.2 V_{SCE}, while the E_{corr} value prior to the polarization scan is –0.05 V_{SCE}. The shift could be attributed to the reduction of oxide on the surface during the cathodic scan, resulting in a new E_{corr} being observed. For CS at pH 6.0, however, the major corrosion pathway is Fe dissolution, so there are minimal amounts of oxides on its surface, or the oxides that are present are not huge potential barriers. Therefore, its E_{corr} is not affected significantly during the potentiodynamic polarization. In this work, i_{corr} is obtained by extrapolation of both the anodic and cathodic Tafel regions or only the cathodic Tafel region to $E_{i=0}$. The i_{corr} values of SS 304 and SS 309 at both pHs and the i_{corr} of CS at pH 10.6 and all temperatures are in the order of 10^{-8} to 10^{-7} A/cm^2 whereas the i_{corr} of CS at pH 6.0 is in the order of 10^{-5} A/cm^2. The two to three orders of magnitude higher i_{corr} of CS than that of other cases at pH 6.0 is consistent with the linear polarization resistance results presented earlier in Figure 4.3.

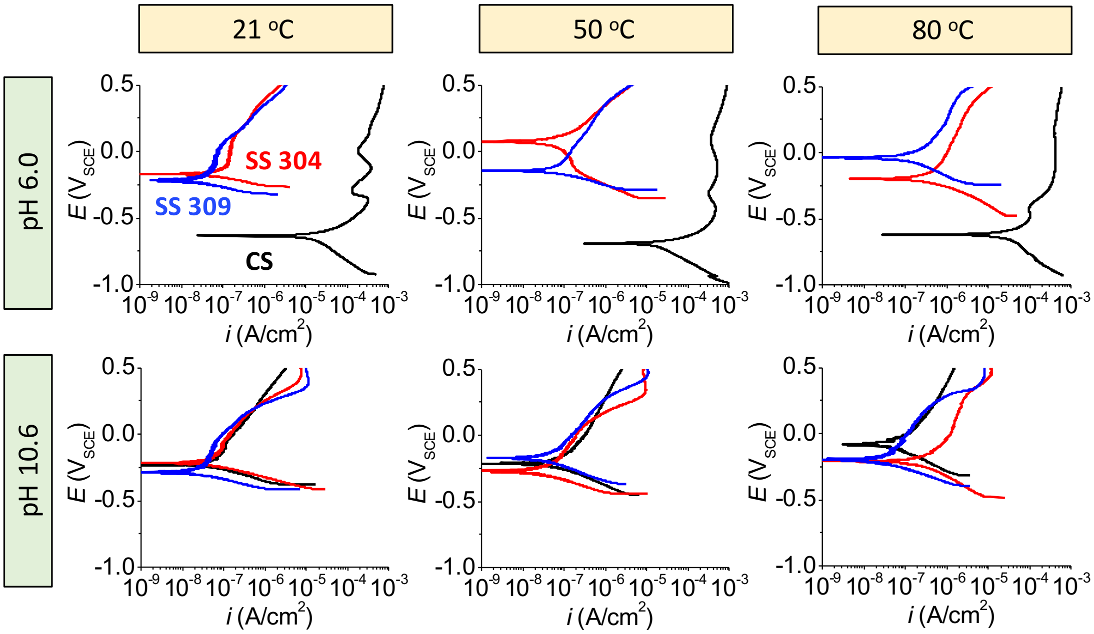

Figure 4.8 Potentiodynamic polarization curves obtained for CS, SS 304 and SS 309 after 72-h corrosion at varying pHs and temperatures.

For CS at pH 6.0 the further potential scan also shows two small anodic peaks. At 21 °C, the two peaks are at potential –0.4 and –0.2 V$_{\text{SCE}}$ respectively, which shift to more negative values at a higher temperature. Note that the potential values presented here are the potentials at the peaks, since the onset potentials of the peaks are not that easy to determine. That is, the oxidation reactions corresponding to these peaks could start at a lower potential than the potentials at the peaks. By making reference to the E_{eq} diagram

(Figure 4.6), the first peak at −0.4 V_{SCE} is assigned to the oxidation of $Fe(OH)_2$ to Fe_3O_4 while the second peak at −0.2 V_{SCE} is assigned to the oxidation of Fe_3O_4 to γ-Fe_2O_3. The second peak broadens with temperature because magnetite formation increases with temperature [13,14] which in turn promotes the oxidation of Fe_3O_4 to γ-Fe_2O_3. Above this potential the anodic current increases only slightly with potential, which indicates that the oxidation rate in this potential range is limited not by interfacial electron transfer but by mass transport of charged species from the metal surface to the bulk solution.

To confirm these electrochemical studies and better understand the corrosion behaviours of the individual alloys, corrosion tests under the same solution conditions were performed. After each test, the corroded surfaces were characterized by scanning electron microscopy (SEM). Note that no visual differences between the surface morphologies of SS 304 and SS 309 can be observed. Therefore, only the results for SS 309 are presented.

As shown in Figure 4.9, two types of surface morphologies can be observed. The surfaces of SS 309 at both pHs, and CS at pH 10.6 and all temperatures remain relatively clean, with no significant granular oxides present. Polishing scratches can be observed, indicating minimal extent of corrosion. This is consistent with the low $1/R_P$ obtained in electrochemical tests which suggests that the rate of metal oxidation is low. Small oxide particles are observed on SS 309 at pH 10.6 and they grow bigger at a higher temperature. This can be explained by faster metal dissolution and precipitation processes at a higher temperature. As discussed earlier, the oxides that can form on SS 309 are a mixture of Cr_2O_3 / $FeCr_2O_4$ / Fe_3O_4 / $NiFe_2O_4$ / $Ni(OH)_2$/ γ-Fe_2O_3. Due to the much lower solubility of Ni^{II} and Fe^{II} species at pH 10.6 than at pH 6.0, the observed small oxide particles should mainly consist of mixed Ni^{II} and Fe^{II} oxides. Similar small oxide particles are also observed on the surface of SS 309 at pH 6.0 but at a much higher temperature (80 °C). In contrast, CS at pH 6.0 shows a totally different morphology. The metallurgical structure of carbon steel consists of a pure α-Fe phase and a pearlite phase made of alternating cementite and α-Fe layers, and metal dissolution occurs from the α-Fe phase. At 21 °C and 50 °C, the cementite skeleton and different grains can be observed indicating that rapid Fe dissolution is taking place. As the temperature increases from 21 °C to 50 °C, the gaps between the cementite layers are filled with more granular oxides. When the temperature increases to 80 °C, the cementite structures are not as obvious as those at lower temperatures since they are covered by different oxide particles. The oxides on the surface in this case are loose and non-compact indicating that the subsequent metal oxidation rate will not be significantly reduced. It can also be inferred from the surface morphologies that these oxides are formed through the metal dissolution-precipitation process. The corrosion tests again show that the corrosion dynamics of CS evolve through different dynamic stages and that the progression of CS corrosion is accelerated at higher temperatures. This is consistent with our observation of an earlier decrease of $1/R_P$ at higher temperatures.

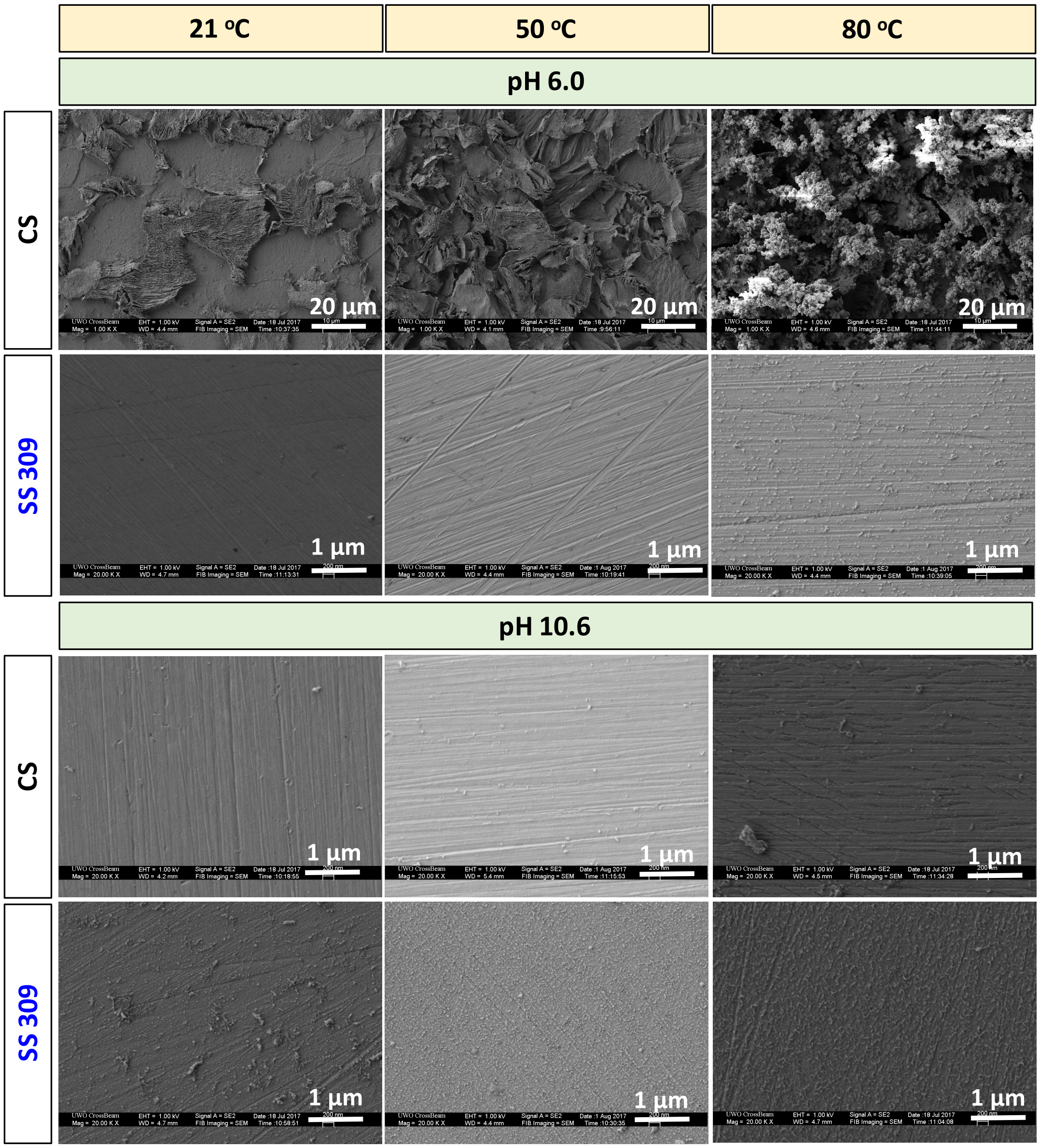

Figure 4.9 SEM micrographs of CS and SS 309 surfaces after 72-h corrosion in pH 6.0 and 10.6 borate buffer solutions at 21 °C, 50 °C and 80 °C in the absence of radiation.

4.3.2 Corrosion currents obtained by different methods

The i_{corr} measurement of CS using a newly-developed dual-electrochemical cell set-up (DEC) was also conducted. The current measured using this method was then compared with those obtained using the conventional electrochemical polarization techniques (PD and LPR). In this section, the results obtained at pH 6.0 and 21 °C are shown. The E_{corr} and i_{corr} monitored in real time using the DEC method are presented in Figure 4.10. The results from four separate tests over different durations are presented together to illustrate their reproducibility. The data are plotted on two different time scales. The variation in the time-dependent behaviours of E_{corr} and i_{corr} between tests conducted using the DEC method was small. In all tests, E_{corr} approached a near steady-state value very quickly and remained close to this value over the test duration (0.5 h to 72 h). The main variation was in the steady-state E_{corr} value, which was either –0.630±0.005 V_{SCE} or –0.615±0.005 V_{SCE}. The i_{corr} measured by the DEC method initially increased to a maximum value of ~80 μA/cm^2 within 10 min. This was followed by a slow decrease for about 20 h to a minimum value of 50–60 μA/cm^2 and a slow increase for another 20 h before approaching a steady-state value of about 70 μA/cm^2.

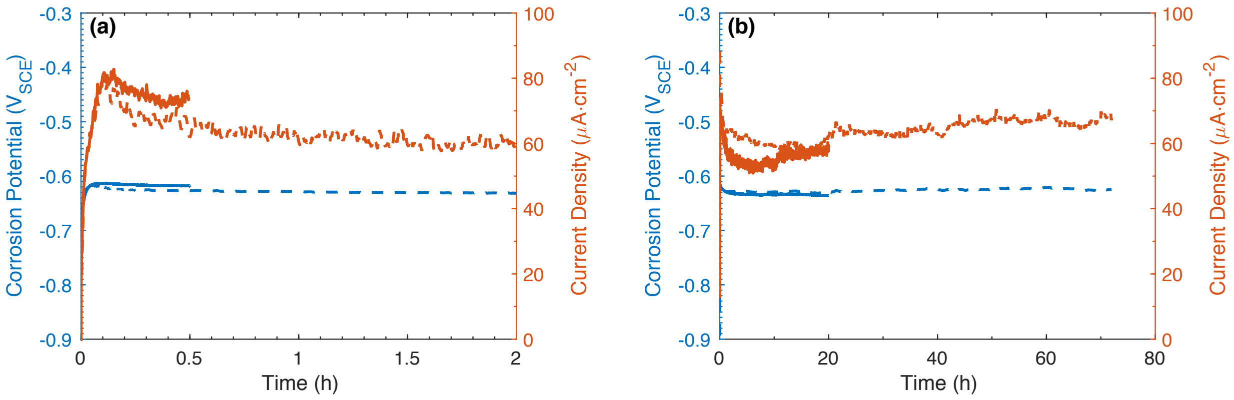

Figure 4.10 The E_{corr} and i_{corr} monitored in real time by the DEC method for carbon steel corrosion in aerated borate buffer solution at pH 6.0 for various durations: (a) 0.5 h and 2 h; (b) 20 h and 72 h.

The results from the PD scan and LPR methods are presented in Figure 4.11. Each PD scan was conducted on a different carbon steel electrode that had been corroded for a different duration. The E_{corr} values recorded over time, prior to the PD scans after 20-h and 72-h corrosion are shown. Those from the 0.5-h and 2-h tests were the same as those obtained for the longer duration. The variation in E_{corr} between tests was similar to that observed in the DEC analysis with the main variation being the steady-state E_{corr} value, which was either –0.630±0.005 $\mathrm{V_{SCE}}$ or –0.615±0.005 $\mathrm{V_{SCE}}$.

The PD scans obtained after different corrosion times all show a wide cathodic potential range exhibiting a linear dependence of $\log|i_{\mathrm{meas}}|$ on E_{appl}. Interestingly, the cathodic Tafel region starts at about 100 mV below E_{corr} for the 0.5-h corroded carbon steel. However, this starting potential value gradually increases with corrosion time, and after 72-h corrosion the cathodic Tafel region starts at about 30 mV below the E_{corr} value. The Tafel slope also changes with corrosion time, decreasing from –620 mV/dec at 0.5 h to –216 mV/dec at 72 h. The PD scans show no clear anodic potential range with a linear dependence of $\log|i_{\mathrm{meas}}|$ on E_{appl}. Hence, the i_{corr} value was obtained via extrapolation from the cathodic Tafel region. The anodic Tafel slope value was then determined by least square fitting: the b_{a} value that gave the best fitting result for the polarization curve in the potential region from E_{corr} to E_{corr}+60 mV was chosen. The anodic and cathodic Tafel lines are indicated with red lines in Figure 4.11 (a). Also shown in Figure 4.11 (a) is the fitted polarization curve using the two Tafel slopes (green lines). The b_{a} value thus obtained fluctuated from 107 to 165 mV/dec with no clear time dependence. Because only on the cathodic branches of the PD scans exhibited a clear Tafel relationship, the i_{corr}

values were obtained by extrapolating the cathodic Tafel slopes to $E_{\mathrm{elec}} = E_{\mathrm{corr}}$, and these values are presented along with the E_{corr} data in Figure 4.11 (a).

The LPR measurements were conducted every 2 h. Only a few examples of the linear polarization curves are shown in Figure 4.11 (b). Presented below the polarization curves are the $1/R_{\mathrm{P}}$ values determined from the polarization curves conducted every 2 h. The polarization curves over the small potential range ($E_{\mathrm{corr}} \pm 10$ mV) show a small degree of hysteresis. Because the polarization curves obtained from the PD scan tests were also asymmetric (Figure 4.11 (a)), we applied the Stern-Geary equation (4.3) to convert the R_{P} to the i_{corr} values. The b_{a} and b_{c} values were determined from the PD scans presented in Figure 4.11 (a). As discussed above, the b_{a} and b_{c} values ranged from 107 to 165 mV/dec and from −620 to −216 mV/dec, respectively. Because of the wide ranges and uncertainties in the Tafel slopes, the proportionality constant, B, in the Stern-Geary equation that is required to convert R_{p} to i_{corr}, ranged from 31 to 56 mV. The i_{corr} values converted from the R_{P} using the minimum and maximum constants are presented along with the E_{corr} data in Figure 4.11 (b).

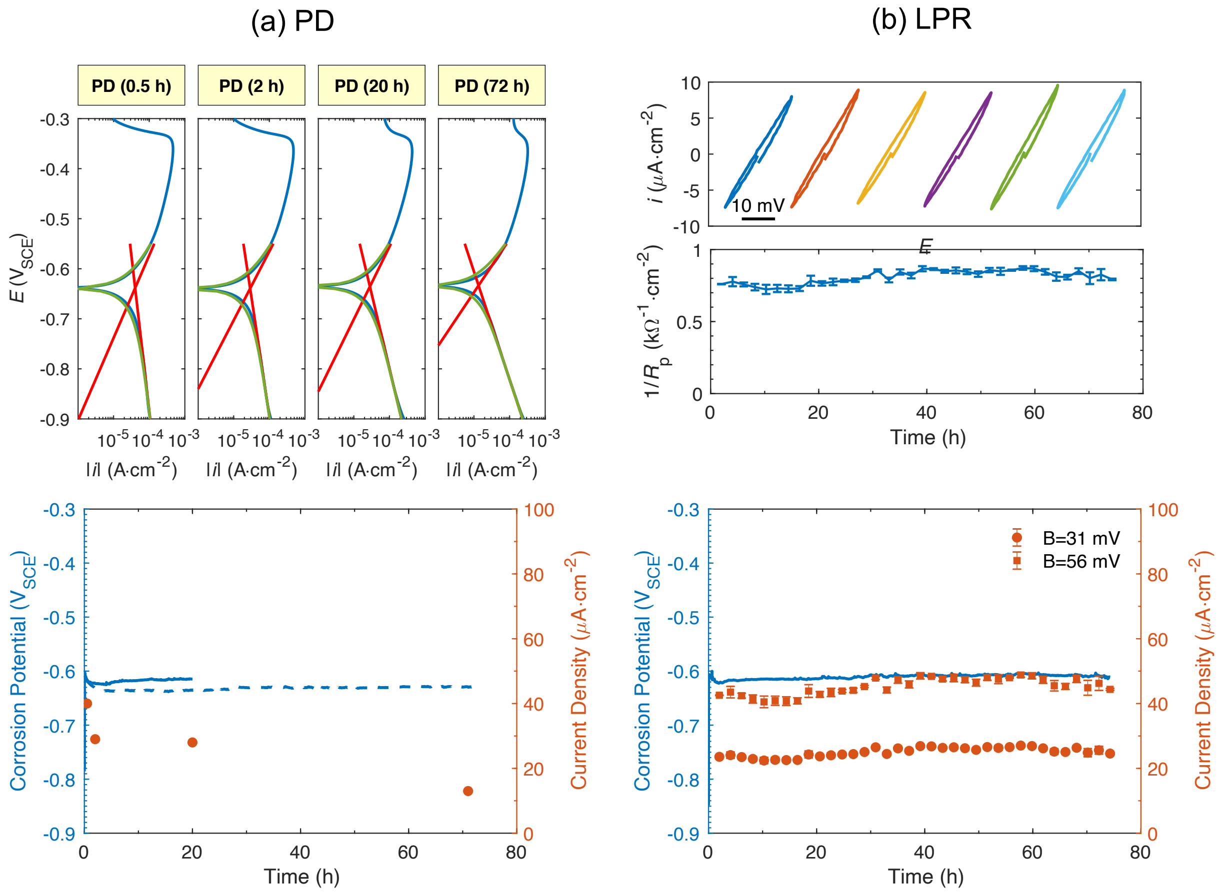

Figure 4.11 E_{corr} and i_{corr} values obtained from (a) PD scan analysis and (b) LPR analysis for carbon steel in aerated borate buffer solution at pH 6.0. Also shown are the polarization curves from the PD scans, and the R_{p} results and some of the polarization curves from the LPR data.

The E_{corr} and the i_{corr} obtained from the different polarization methods are compared with those from the DEC method in Figure 4.12. In this figure, only one set of data from each method is shown. The variations in the time-dependent behaviours of E_{corr} and i_{corr} between tests conducted with each method can be seen in Figure 4.10 and Figure 4.11. As observed in individual analyses, the variation in E_{corr} between tests conducted using different methods was small. In all tests, E_{corr} approached a near steady-state value very quickly and remained near this value over the test duration (72 h). At the studied pH 6.0, the i_{corr} values determined by different methods are also all within a factor of 3 of each other, with the i_{corr} monitored by the DEC method being highest.

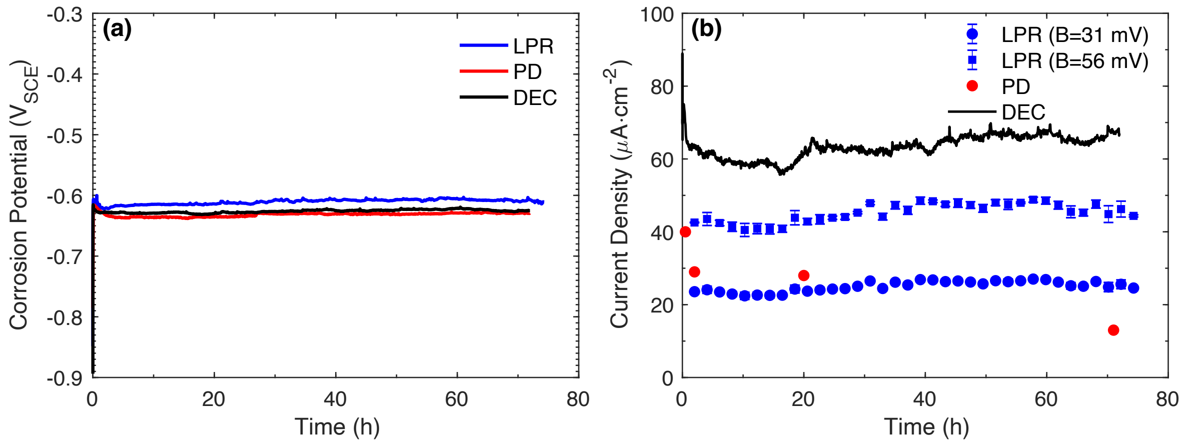

Figure 4.12 Comparison of (a) the E_{corr} and (b) the i_{corr} values obtained using different methods.

4.3.3 Comparison of the electrochemical analyses with dissolved metal analysis

In order to assess the accuracy of the different electrochemical methods in determining the metal oxidation (or corrosion) rate in the studied system (CS corrosion in aerated solution at pH 6.0), the results were analyzed in relation to the post-test solution and surface analyses. The amounts of dissolved metal in solution (detected by ICP-OES) are presented in Figure 4.13. Also presented in Figure 4.13 are the amounts of oxidized metal calculated from the i_{corr} obtained using different methods. For the amount of oxidized metal, the total accumulated charge ($Q = \int i_{\text{corr}}\, \mathrm{d}t$) was converted to the oxidized mass using Faraday's law [15], assuming all metal oxidation resulted in Fe^{2+}. The surface morphologies of the CS surfaces observed by SEM and optical microscopy are presented in Figure 4.14.

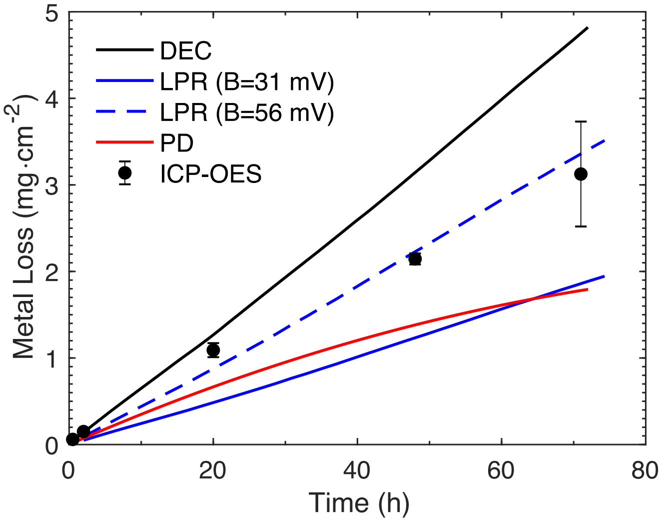

Figure 4.13 Comparison of the dissolved metal amount detected by ICP-OES (symbols) and the amounts of oxidized metal calculated from the i_{corr} values obtained by the different electrochemical methods.

The amounts of oxidized metal calculated from the i_{corr} values obtained by different electrochemical methods are all within a factor of 3 of the measured amounts dissolved in solution. The DEC method gave an oxidized amount close to the dissolved amount at corrosion times less than 20 h, but higher than the dissolved amount at longer times. All the other methods gave oxidized amounts equal to or less than the dissolved amounts, for all time points.

The metal oxidation products include metal hydroxide/oxide precipitates as well as metal cations and their hydrolysis products that are dissolved or dispersed in solution. Hence, the oxidized amount should be always greater than or equal to the amount detected in solution. The oxidized amount obtained from the DEC method is greater than or equal to the dissolved/dispersed amount at all measured times, but those determined using the other electrochemical methods are lower. The DEC method also shows an increase over time in the difference between the oxidized and the dissolved/dispersed amounts, suggesting that the fraction of oxidized metal resulting in oxide formation increases with time. The SEM and optical images shown in Figure 4.14 support this hypothesis.

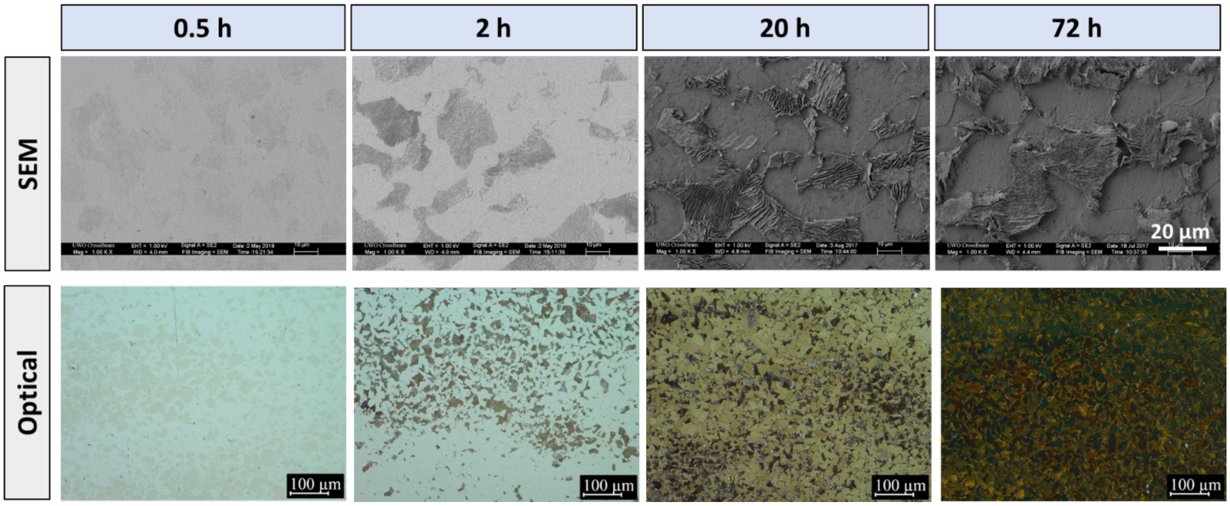

Figure 4.14 SEM and optical micrographs of CS surfaces corroded in aerated solutions at pH 6.0 for different durations.

Because metal dissolution occurs from the surface of α-Fe, over the short duration (≤ 2 h) in which dissolution is the main corrosion reaction, the lamellar structure of the pearlite phase consisting of alternating layers of cementite (Fe_3C) and α-Fe becomes more clearly defined in the SEM image with time. The bluish and black areas in the optical images correspond to the surfaces of the pure α-Fe phase and the pearlite phase, respectively. After 20 h corrosion, the amount of oxidized metal determined using the DEC method starts deviating from the amount of dissolved metal detected by ICP-OES. At this time, the SEM image clearly shows the cementite layers in the pearlite phase (due to dissolution of the intervening α-Fe layer), indicating more extensive Fe dissolution over longer periods of corrosion. The optical image shows that the surface of the α-Fe phase is covered by a thin uniform layer of brownish-yellow hydroxide, with the SEM image indicating that no significant quantities of granular oxide are present. At 20 h the gaps between the cementite layers are partially filled with granular oxides. After 72 h corrosion, the gaps between the cementite layers are filled with granular oxides and the α-Fe phase is covered by a yellow/orange oxide layer.

The DEC method yields corrosion currents that are more consistent with the sum of metal dissolved in solution and precipitated as metal hydroxides/oxides. Thus, it can be concluded that the i_{corr} measured by the DEC method is a more accurate representation of the actual corrosion rate. The i_{corr} values determined by the conventional polarization methods have larger uncertainties, and in general, underestimate the corrosion rate. The corrosion current results using the DEC measurements at higher temperatures will be presented and discussed in the next chapter.

4.4 Conclusions

In this chapter the effect of solution properties (pH and temperature) on the independent corrosion behaviour of CS, SS 304 and SS 309 was studied using a combination of electrochemical techniques and immersion tests. This work provides a qualitative understanding of the individual corrosion behaviours of CS, SS 304 and SS 309. SS 304 and SS 309 show similar corrosion behaviours and their corrosion rates remain low at both pH 6.0 and 10.6 due to the presence of protective oxide layers on the surface. Within the test duration, the major corrosion pathway for CS at pH 6.0 is metal dissolution, whereas for pH 10.6 it is oxide formation, due to the much lower solubility of Fe^{II} at this pH.

The corrosion rates of CS at pH 6.0 obtained using conventional electrochemical methods and a DEC method were analyzed. It was demonstrated that in contrast with conventional electrochemical techniques (LPR and PD), the DEC method allows continuous measurement of corrosion rate, and provides more accurate corrosion rate information.

In summary, after studying the independent corrosion behaviours of the individual alloys, it can be concluded that galvanic corrosion will be negligible for the SS 304-SS 309 couple under all studied conditions and the CS-SS 309 couple at pH 10.6. As a result, the subsequent studies on galvanic corrosion (to be discussed in Chapter 5) focus on the CS-SS 309 couple at pH 6.0 due to the great variation in the independent corrosion behaviours between these two alloys at this pH.

4.5 References

[1] D. Guo, Corrosion Dynamics of Carbon Steel in Used Fuel Container Environments, The University of Western Ontario, London, ON, 2018.

[2] M. Stern, A.L. Geary, J. Electrochem. Soc., 104 (1957) 56–63.

[3] E. Stansbury, R. Buchanan, Fundamentals of Electrochemical Corrosion, ASM International, 2000.

[4] A. Seyeux, V. Maurice, P. Marcus, J. Electrochem. Soc., 160 (2013) C189–C196.

[5] M. Momeni, J.C. Wren, Faraday Discuss., 180 (2015) 113–135.

[6] M. Momeni, Gamma-Radiation Induced Corrosion of Alloy 800, The University of Western Ontario, London, ON, 2017.

[7] A.Y. Musa, J.C. Wren, Corros. Sci., 109 (2016) 1–12.

[8] T. Misawa, Corros. Sci., 13 (1973) 659–676.

[9] W. Xu, K. Daub, X. Zhang, J.J. Noel, D.W. Shoesmith, J.C. Wren, Electrochim. Acta, 54 (2009) 5727–5738.

[10] K. Daub, X. Zhang, J.J. Noël, J.C. Wren, Electrochim. Acta, 55 (2010) 2767–2776.

[11] K. Daub, X. Zhang, J.J. Noël, J.C. Wren, Corros. Sci., 53 (2011) 11–16.

[12] F. Mansfeld, Corros. Sci., 47 (2005) 3178–3186.

[13] M. Booy, T.W. Swaddle, Can. J. Chem., 56 (1978) 402–403.

[14] R.O. Rihan, S. Nešić, Corros. Sci., 48 (2006) 2633–2659.

[15] A.J. Bard, L.R. Faulkner, Electrochemical Methods Fundamentals and Applications, 2nd ed., John Wiley & Sons, Inc., 2001.

Chapter 5. Effect of Solution Properties on the Galvanic Corrosion of a Carbon Steel-Stainless Steel Couple

5.1 Introduction

The independent corrosion behaviours of carbon steel (CS), stainless steel (type 304, SS 304) and the stainless steel filler material (type 309, SS 309) under different solution conditions were discussed in Chapter 4. Due to the significantly different behaviours of CS and SS 309 (simply referred to as SS hereafter) at pH 6.0, this chapter focuses on the corrosion dynamics of galvanically coupled CS-SS at this pH.

Galvanic corrosion occurs when two different metals are in electrical contact and exposed to a corrosive environment. It is generally accepted that, under these conditions, the corrosion rate of the more active metal is increased while that of the more noble metal is reduced [1]. The more active metal is often referred to as the anode while the more noble metal is referred to as the cathode. In our case, CS is the anode while SS is the cathode. As discussed in Chapter 4, the corrosion rate of SS is much lower than that of CS when they corrode independently. Therefore, after it was galvanically coupled to SS, more attention was paid to the corrosion rate of CS than that of SS.

As described in Chapter 2, researchers usually correlate the corrosion rate of the more active metal in a galvanic couple with the measured coupling current (I_{cpl}). Two assumptions are typically used for such correlations. In most cases, researchers ignore the contribution of the reduction current on the more active metal and regard I_{cpl} as the corrosion rate of the more active metal after coupling [2–7]. In a few other cases, researchers noticed that the reduction current on the more active metal was not actually negligible. However, the reduction current on the metal after coupling cannot be measured separately so it is assumed that the reduction current is the same as when it corrodes independently [8,9]. As a result, the corrosion rate of the more active metal after coupling is considered to be the sum of I_{cpl} and its independent corrosion rate. With this assumption, the measured I_{cpl} is the increased amount of corrosion of the anode after galvanic coupling. In this chapter, the corrosion rates of CS after galvanic coupling to SS were obtained by using these two assumptions. The corrosion rates of CS and SS with/without galvanic coupling to each other were also measured using the dual-electrochemical cell (DEC) method. The corrosion current results were then compared with the solution analyses and surface analyses for validity testing. Based on the DEC results, the galvanic effect as a function of time was calculated. The effect of temperature on the galvanic corrosion of CS-SS is also discussed in this chapter.

5.2 Experimental

5.2.1 Electrode and electrolyte preparation

A three-electrode cell, consisting of a reference electrode, a Pt mesh counter electrode and a metal working electrode was used for the electrochemical studies. The working electrode was either CS (type SA36), SS (type 309) or an electrically connected CS-SS couple. A saturated calomel electrode (SCE) (Fisher Scientific) was used for experiments carried out at room temperature (21 °C) and 50 °C, whereas an Ag/AgCl electrode was employed for experiments conducted at 80 °C due to its stability at elevated temperatures. For high-temperature tests, the electrochemical cell was heated by the circulation of heated water maintained at the desired temperature through the dual-walled cell body.

The CS rod was cut into cubes and the SS weld material was cut into discs. The exposed surface areas of the CS and SS coupons were limited to 0.455 cm^2 and 1.267 cm^2 respectively by coating the surrounding areas with Teflon. Prior to each test the coupon was abraded successively with 1200 and 2500 grit SiC paper followed by polishing on a Texmet microcloth (Buehler) with a 1 μm MetaDi Supreme diamond paste suspension (Buehler), to reach a mirror-like surface. All exposed surfaces of coupons were immersed in 0.01 M Borate buffer solutions using reagent grade $Na_2B_4O_7 \cdot 10H_2O$ (EMD Millipore Corporation) in air. The solution pH was adjusted to 6.0 by adding reagent grade H_3BO_3 (Caledon Laboratories Ltd.) to the borate solutions. Solutions were prepared with purified water using a NANOpure Diamond UV ultra-pure water system (Barnstead International) to give a resistivity of 18.2 MΩ·cm. The solution volume was 0.5 L.

5.2.2 Coupling potential and coupling current measurements

The coupling potential (E_{cpl}) and coupling current (i_{cpl}) of the CS-SS couple exposed to a given environment were measured using the set-up shown in Figure 5.1. This set-up consists of two channels of a potentiostat, which makes simultaneous measurement of the E_{cpl} and i_{cpl} possible. Channel 1 was used to perform cathodic cleaning in the first 5 min followed by the measurement of E_{cpl}. Channel 2 mainly functions as a zero-resistance ammeter. It ensures that the SS is electrically connected to the CS by applying a potentiostatic polarization (0 vs. Reference) and measures the i_{cpl}. The i_{cpl} presented here is normalized to the surface area of CS. All electrochemical measurements were carried out for 72 h.

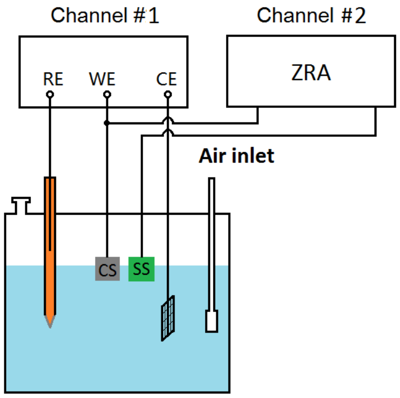

Figure 5.1 Schematic illustration of the set-up used for the E_{cpl} and i_{cpl} measurements of the CS-SS couple.

5.2.3 Dual-electrochemical cell measurement

A dual-electrochemical cell (DEC) set-up consisting of two identical three-compartment electrochemical cells was used for the determination of corrosion rates. The set-up for an independent corrosion system was introduced in Chapter 4 and the set-up for a galvanic corrosion system is illustrated in Figure 5.2. The principle of the DEC measurement is to measure the polarization current continuously when the working electrode in a deaerated solution is polarized to the E_{cpl} value obtained in an aerated solution. If the contribution of water reduction to the measured polarization current is not significant, the obtained polarization current can then be regarded as the corrosion current of the electrode under aerated conditions.

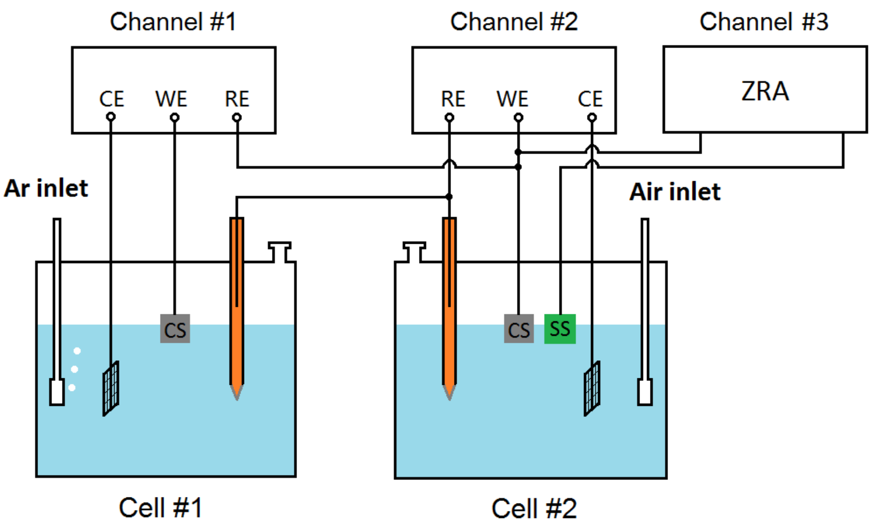

Figure 5.2 Schematic illustration of the DEC set-up for the galvanic corrosion of the CS-SS couple [10].

Cell #2 shown in Figure 5.2 is the same as that in Figure 5.1. Channel #2 and Channel #3 are used to measure E_{cpl} and i_{cpl} of the CS-SS couple, respectively, whereas Channel #1 is used for the measurement of the polarization current of CS after coupling. Cell #2 in the DEC set-up functions as a continuous input of E_{corr} or E_{cpl}. This set-up was later simplified to a standard single cell (Cell #1) with a customized input of the electrode potential profile since the E_{corr}, E_{cpl} profiles have been recorded previously using conventional electrochemical techniques (to be discussed in Chapter 6).

The details of the working, counter and reference electrodes and solutions used are the same as those stated earlier for a traditional three-electrode electrochemical cell.

5.2.4 Surface characterization and solution analysis

After the individual CS, SS electrodes and the galvanically coupled CS-SS had corroded for different durations, they were dried with Ar. The surfaces were then analyzed by scanning electron microscopy (SEM). The oxides on the CS surface were also characterized using the Raman spectroscopy. Raman spectroscopy was performed using a Renishaw model 2000 spectrometer equipped with a Melles Griot 35mW 633 nm HeNe laser with a focused beam diameter of ~2 µm. The dissolved iron concentration in the solution after each test was analyzed using a Perkin Elmer Avio 200 inductively coupled plasma optical emission spectrometer (ICP-OES). Prior to the solution analysis the samples were digested using nitric acid (Trace analytical grade, Fisher Scientific) to dissolve any colloidal particles in the test solution. Therefore, the measured dissolved iron concentration may include any colloid particles, if present.

5.3 Results and Discussion

5.3.1 Galvanic corrosion of the CS-SS couple

The coupling potential (E_{cpl}) and coupling current (i_{cpl}) of the electrically coupled CS-SS were measured continuously over 72 h. The results together with the dissolved metal analysis results are presented in Figure 5.3. The total amount of dissolved Fe over 72 h from SS is negligible compared to that from CS. Hence, the total dissolved Fe for the CS-SS couple was normalized to the surface area of CS.

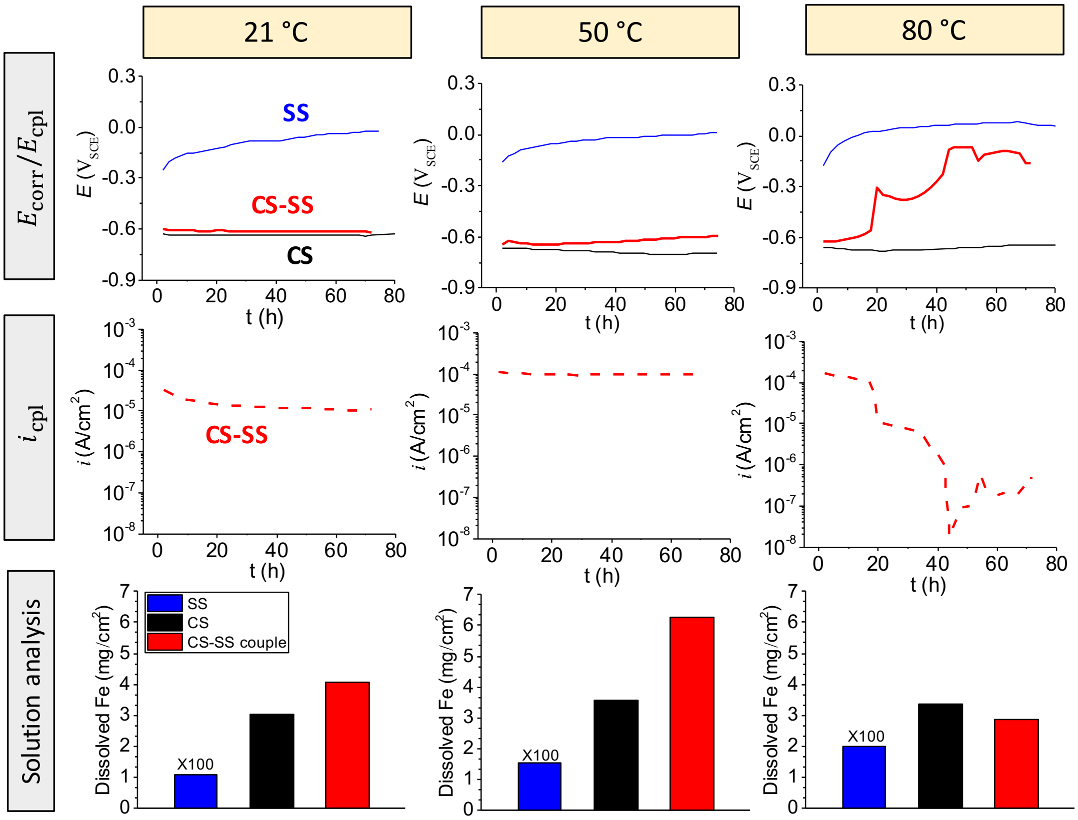

Figure 5.3 Evolution of E_{corr}, E_{cpl} and i_{cpl} with time during 72-h independent corrosion of CS, SS and galvanic corrosion of a CS-SS couple, and the corresponding dissolved Fe in solutions. The dissolved Fe amounts for SS corrosion shown here are magnified 100 times.

At 21 °C, the E_{cpl} value of the CS-SS couple is close to the E_{corr} value of CS indicating that CS was not polarized far from its natural corroding state upon galvanic coupling. The difference between the E_{cpl} and E_{corr} of CS at 50 °C remains as low as at 21 °C in the first 20 h, but gradually becomes larger with time. In Chapter 4 we showed that the E_{corr} of CS changes with time, decreasing initially and increasing at later times, and this change in E_{corr} accelerates with increasing temperature. The galvanic coupling further accelerates the progression of E_{cpl}. At 21 °C and 50 °C, the E_{cpl} still remains below –0.6 V_{SCE} over 72 h. At 80 °C, the E_{cpl} changes at a much faster rate, reaching –0.6 V_{SCE} within 20 h. This is followed by a rapid increase in E_{cpl} over a short duration to a second pseudo steady-state value, and another rapid increase at around 40 h to a third pseudo steady-state value closer to the E_{corr} of SS (about –0.15 V_{SCE}).

The changes in the electrode potential due to galvanic coupling and temperature increase are reflected in the changes in i_{cpl}. The i_{cpl} decreases with time at both 21 °C and 50 °C, but with a higher rate at 21 °C over the test duration. The i_{cpl} at 50 °C is higher than that at 21 °C, by a factor of 3 initially, but by a factor of 10 after 20-h corrosion. The total dissolved Fe over 72 h from the CS-SS couple is also higher at 50 °C than at 21 °C, but by a factor of less than 2.

At 80 °C, the time-dependence of i_{cpl} closely follows the inverse of the time-dependence of E_{cpl}: the sharp decreases in i_{cpl} coincide with the sharp increases in E_{cpl} around 20 h and 40 h. The initial i_{cpl} value in the first 2 h is higher than those at lower temperatures (about 2×10^{-4} A/cm^2). It then gradually decreases but still remains in the order of 10^{-4} A/cm^2, the same value as at 50 °C. At ~20 h, i_{cpl} quickly drops to a value of 10^{-5} A/cm^2 and remains at this level over the next 20 h. At ~40 h, i_{cpl} drops to near zero before it recovers to the final steady-state value of 10^{-7} A/cm^2. At 80 °C, the dissolved Fe in the solution for the CS-SS couple over 72 h is lower than for independent CS corrosion. These results indicate that the rate-determining step (RDS) for the overall metal oxidation switches from oxidation producing soluble ferrous species to that producing insoluble ferric species, and this switch occurs at an earlier time at a higher temperature.

5.3.2 Corrosion currents obtained by different methods

The corrosion currents measured by the DEC method for CS corroding independently ($i_{\text{corr}-\text{CS ind}}$) and while galvanically coupled to SS ($i_{\text{corr}-\text{CS cpl}}$) are presented in Figure 5.4. Also presented in the figure are the corresponding accumulated charges. At 21 °C, the $i_{\text{corr}-\text{CS ind}}$ is nearly constant over 72 h, about 6.4×10^{-5} A/cm^2. The $i_{\text{corr}-\text{CS cpl}}$ changes with time with an average value of 9.1×10^{-5} A/cm^2. The $i_{\text{corr}-\text{CS cpl}}$ and i_{cpl} were measured simultaneously and the values of the i_{cpl} measured in this test and the test whose results are presented in Figure 5.3 are similar, illustrating the reproducibility of the measurement. As described in the introduction, there are currently two ways to correlate the oxidation rate of the more active metal in a galvanic couple ($i_{\text{corr}-\text{CS cpl}}$) with the i_{cpl}. One assumes that the $i_{\text{corr}-\text{CS cpl}}$ is equal to the i_{cpl}. However, the DEC results show that $i_{\text{corr}-\text{CS cpl}}$ is much higher than the i_{cpl}. The other interpretation of i_{cpl} assumes that the $i_{\text{corr}-\text{CS cpl}}$ is the sum of the i_{cpl} and the oxidation rate of the more active metal while it corrodes independently ($i_{\text{corr}-\text{CS ind}}$). In this work, both the potentiodynamic polarization technique (PD) and the DEC measurement were used to obtain $i_{\text{corr}-\text{CS ind}}$. Note that the PD scans for independent CS corrosion at pH 6.0 for various durations were presented in Chapter 4 and hence are not shown as a separate figure here. The $i_{\text{corr}-\text{CS cpl}}$ results obtained from different methods are compared in Figure 5.5.

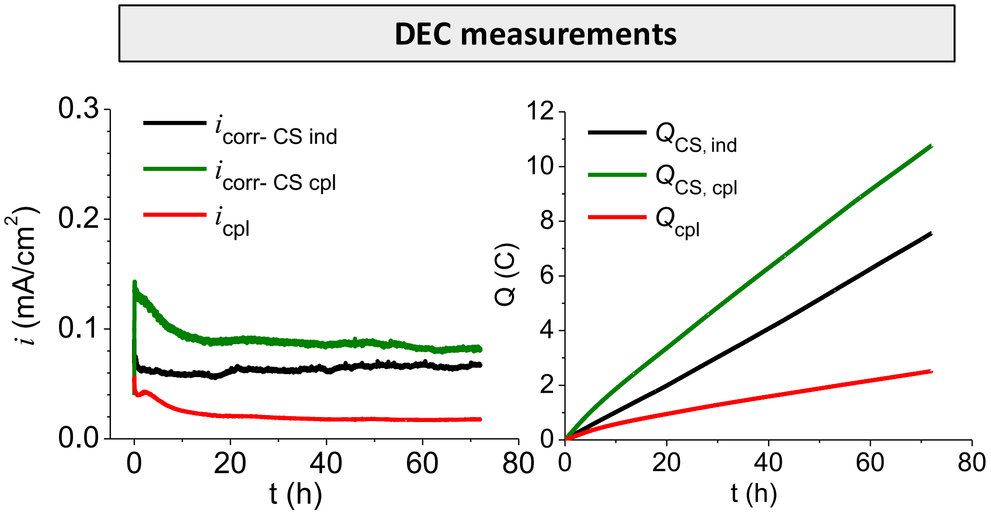

Figure 5.4 The polarization currents and the corresponding accumulated charges of CS during independent corrosion ($i_{\mathrm{corr-CS\ ind}}$, $Q_{\mathrm{CS,ind}}$) and galvanic coupling to SS ($i_{\mathrm{corr-CS\ cpl}}$, $Q_{\mathrm{CS,cpl}}$) and the galvanic currents between CS and SS (i_{cpl}, Q_{cpl}) measured using the DEC set-up at 21 °C.

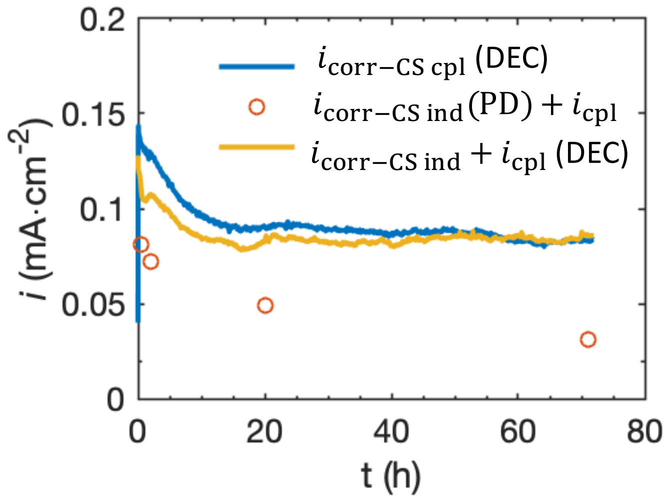

Figure 5.5 Comparison of $i_{\mathrm{corr-CS\ cpl}}$ obtained from different methods.

As observed in this figure, the $i_{\text{corr}-\text{CS cpl}}$ values determined by the sum of $i_{\text{corr}-\text{CS ind}}$ determined from the PD scans and i_{cpl} (labelled as $i_{\text{corr}-\text{CS ind}}(\text{PD}) + i_{\text{cpl}}$) are lower than those obtained from the DEC method. The $i_{\text{corr}-\text{CS cpl}}$ monitored by the DEC method is the highest and is close to the sum of $i_{\text{corr}-\text{CS ind}}$ measured by DEC and i_{cpl} (labelled as $i_{\text{corr}-\text{CS ind}}(\text{DEC}) + i_{\text{cpl}}$).

The amount of oxidized Fe calculated from the $i_{\text{corr}-\text{CS ind}}$ measured by the DEC method was compared with the dissolved metal amount during the independent corrosion of CS by ICP-OES in Chapter 4. The results showed a good correlation of the $i_{\text{corr}-\text{CS ind}}$ with the dissolved Fe amounts at pH 6.0. In this chapter's work, a similar comparison was performed on the CS-SS couple and the results are presented in Figure 5.6. The total amounts of oxidized metal were again calculated based on the accumulated charge over time ($Q = \int i_{\text{corr}-\text{CS cpl}} \cdot \text{d}t$) using Faraday's law. In order to carry out this conversion, an assumption was made that i_{corr} represented the total metal oxidation current and that oxidation involved only ($Fe^0 \rightleftharpoons Fe^{2+}{}_{(aq)}$). The surface morphology of the corresponding CS corroded while galvanically coupled to SS was imaged by SEM and optical microscope and the results are presented in Figure 5.7.

The metal oxidation products consist of not only metal cations dissolved in solution, but also metal oxides deposited on the metal surface. Therefore, the total oxidized amount should always be equal to or larger than the dissolved amount in solution. The oxidized amounts calculated using either i_{cpl} or ($i_{\text{corr}-\text{CS ind}}(\text{PD}) + i_{\text{cpl}}$) are always smaller than the dissolved amount. However, the ones calculated based on the DEC results are equal to or larger than the dissolved amount at all studied times. The difference between the results from the DEC method and the solution analysis can be explained by the formation of oxides on the CS surface. The SEM and optical images further support this.

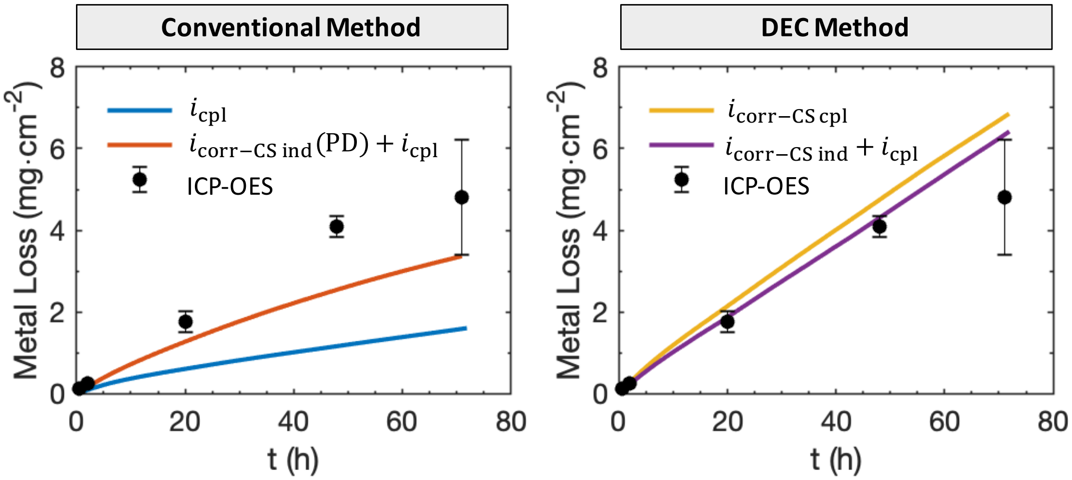

Figure 5.6 Comparison of the dissolved Fe amount from the CS-SS couple detected by ICP-OES (circle symbols) and the amount of oxidized Fe calculated from different methods.

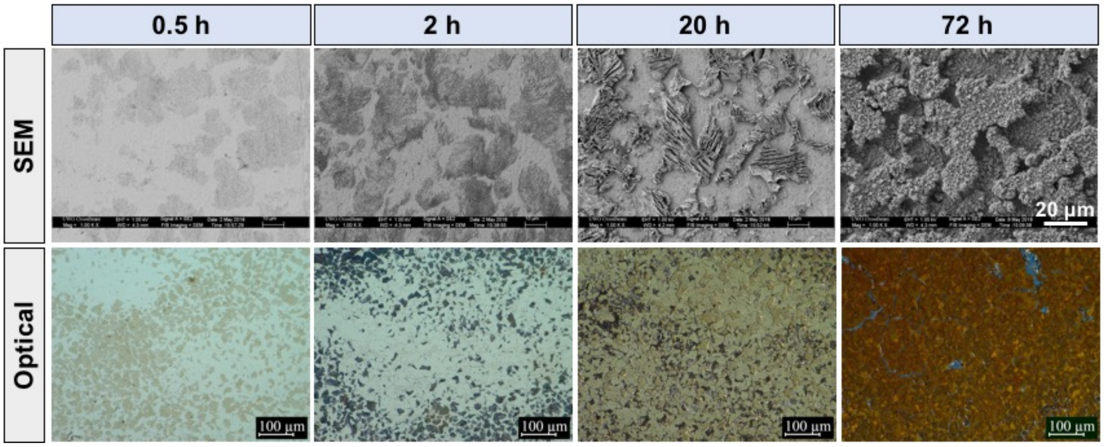

Figure 5.7 The SEM and optical micrographs of CS surfaces corroded while galvanically coupled to SS in aerated solutions at pH 6.0 for different durations.

The solubility of ferrous species at pH 6.0 is high and hence the corrosion pathway for short durations (≤ 2 h), for CS galvanically coupled to SS, is the oxidation of Fe^0 to Fe^{2+} at the surface and the transport of Fe^{2+} from the surface to the bulk solution. As the corrosion time increases from 0.5 h to 2 h, the pearlite phase becomes more noticeable in the SEM images indicating continuous Fe dissolution from the surface of the α-Fe phase. The greenish and black areas in the optical images are the surfaces of α-Fe and the cementite layers, respectively. The oxidized amount determined by the DEC method over this short duration corresponds very well with the dissolved amount from the CS-SS couple.

At longer times (≥ 20 h), the oxidized amount calculated from the $i_{\mathrm{corr-CS\ cpl}}$ measured by DEC is higher than the dissolved amount, indicating the formation of oxides on the surface. The difference between these two values increases with increasing corrosion time, which suggests more oxides have formed on the CS surface at later times. When corroded for 20 h, a uniform brownish yellow hydroxide layer is observed on the CS surface. Although the SEM image shows no significant presence of granular oxide deposits on the CS surface, the gaps between the cementite layers are partially filled with granular oxides. After 72-h corrosion, the gaps between the cementite layers are extensively filled with granular oxides. The optical image shows that the whole CS surface is covered by reddish and orange oxide layers. The oxidized amount calculated from ($i_{\mathrm{corr-CS\ ind}}$ (DEC) + i_{cpl}), however, is higher than the dissolved amount until after 48 h.

Hence, it can be concluded that the DEC method provides more accurate corrosion rate information for CS in a galvanic corrosion system. When the more active metal in a galvanic couple is polarized, but not far from its natural independent corroding state, i_{cpl} cannot be used to represent $i_{\mathrm{corr-CS\ cpl}}$. The reason for this is that the reduction current on the electrode is not negligible. In this case, $i_{\mathrm{corr-CS\ cpl}}$ can be estimated by the sum of i_{cpl} and $i_{\mathrm{corr-CS\ ind}}$. However, as discussed in Chapter 4, accurate measurement of $i_{\mathrm{corr-CS\ ind}}$ using conventional electrochemical techniques may be challenging. The DEC method is particularly useful for cases where both assumptions based on i_{cpl} do not apply, since $i_{\mathrm{corr-CS\ cpl}}$ can be measured directly and continuously.

5.3.3 Corrosion currents of individual CS, SS and galvanically coupled CS-SS

The corrosion current for independent SS corrosion ($i_{\mathrm{corr-SS\ ind}}$) or SS galvanically coupled to CS ($i_{\mathrm{corr-SS\ cpl}}$) were measured using the DEC method and the results are shown in Figure 5.8. In less than 1 min after the 5-min cathodic cleaning at -1.1 V_{SCE}, both $i_{\mathrm{corr-SS\ ind}}$ and $i_{\mathrm{corr-SS\ cpl}}$ reach their maximum values, in the order of 10^{-5} A/cm^2, similar to $i_{\mathrm{corr-CS\ ind}}$. However, after 3 min the values of $i_{\mathrm{corr-SS\ ind}}$ and $i_{\mathrm{corr-SS\ cpl}}$ quickly drop to 10^{-6} A/cm^2, followed by a gradual decrease in $i_{\mathrm{corr-SS\ ind}}$ and $i_{\mathrm{corr-SS\ cpl}}$ before reaching the steady-state value of 10^{-8} A/cm^2 after 10 min. Usually, a metal is considered to be passive when its oxidation rate is below 10^{-6} A/cm^2. The DEC results suggest that SS acts as a passive metal under our studied conditions. Therefore, the oxidation rate of SS whether when it corrodes independently or when galvanically coupled to CS is negligible compared to the high oxidation rate of CS, which is consistent with the potentiodynamic polarization results shown in Chapter 4 and the solution analysis results presented in Figure 5.3.

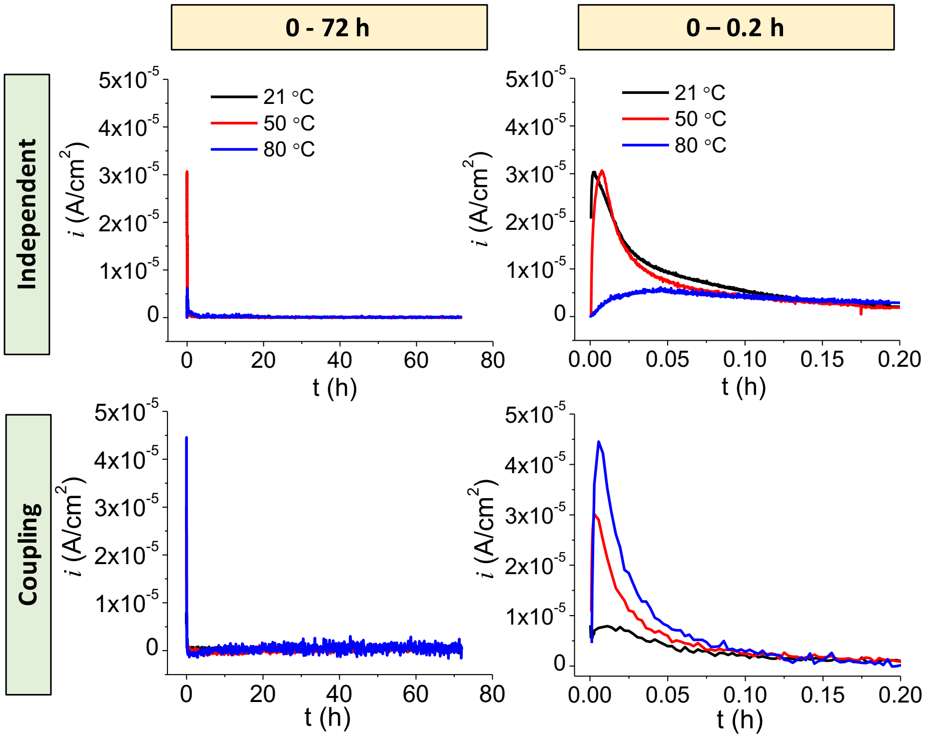

Figure 5.8 The polarization currents of SS during its independent corrosion ($i_{\mathrm{corr-SS\ ind}}$) and when galvanically coupled to CS ($i_{\mathrm{corr-SS\ cpl}}$), measured using the DEC set-up at varying temperatures.

The corrosion currents and the corresponding accumulated charges (Q) for CS at higher temperatures using the DEC method are shown in Figure 5.9. At 21 °C, $i_{\mathrm{corr-CS\ ind}}$ is near constant and the average current over 72 h is about 6.4×10^{-5} A/cm^2. At 50 °C, $i_{\mathrm{corr-CS\ ind}}$ oscillates with time with an average of 1.2×10^{-4} A/cm^2. At these temperatures $i_{\mathrm{corr-CS\ cpl}}$ is initially a factor of 2 or 3 higher than the $i_{\mathrm{corr-CS\ ind}}$ value. But $i_{\mathrm{corr-CS\ cpl}}$ decreases with time, and after 20 h is only 1.2 to 1.5 times higher than $i_{\mathrm{corr-CS\ ind}}$. At 50 °C, i_{cpl} is much lower than $i_{\mathrm{corr-CS\ cpl}}$ over 72 h, further confirming that i_{cpl} is not the CS oxidation current, because the solution reduction current on CS is not negligible.

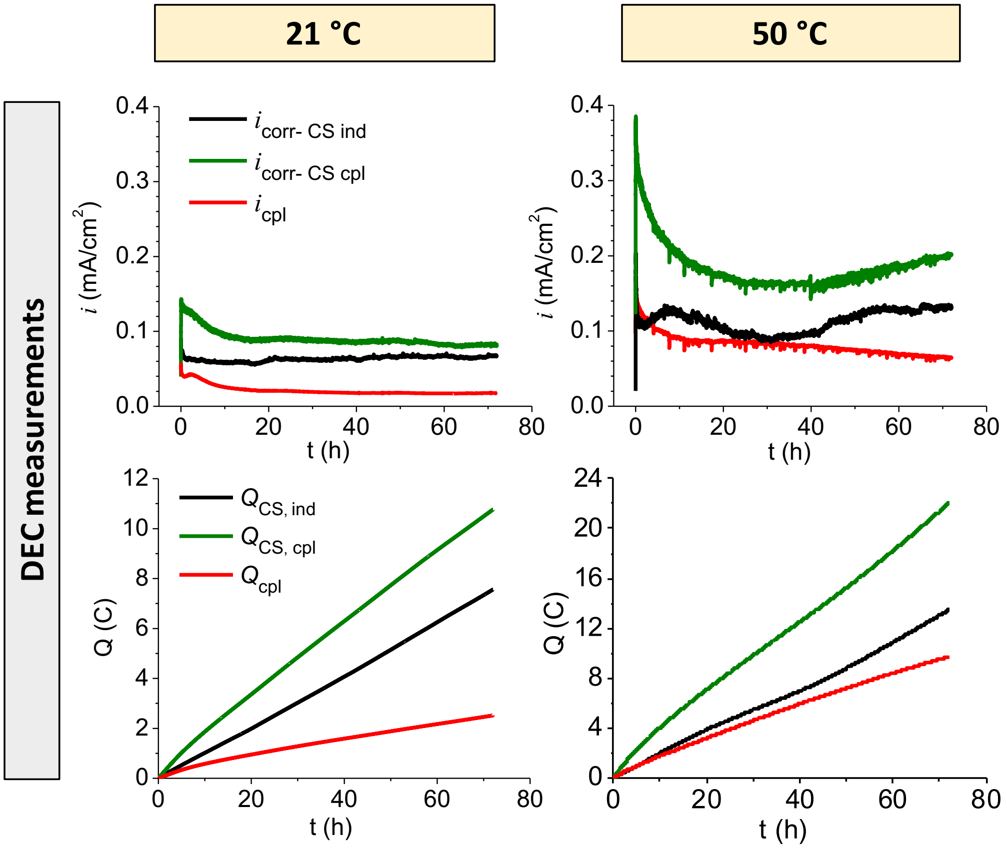

Figure 5.9 The polarization currents and the corresponding accumulated charges for CS during independent corrosion ($i_{\mathrm{corr-CS\ ind}}$, $Q_{\mathrm{CS,ind}}$) and when galvanically coupled to SS ($i_{\mathrm{corr-CS\ cpl}}$, $Q_{\mathrm{CS,cpl}}$) and galvanic currents between CS and SS (i_{cpl}) measured using the DEC set-up at 21 °C and 50 °C.

Based on the accumulated charges the equivalent metal loss was calculated using Faraday's law and the results are listed in Table 5.1. For the metal loss calculation, the assumption remains the same as stated in 5.3.2 – that all dissolved species is Fe^{2+}. The difference between the calculated value and the actual detected amount of Fe species in the solution is the amount of Fe involved in oxide formation on the electrode surfaces (this will be discussed later). In galvanic corrosion studies, the galvanic effect γ is referred to as the ratio of the corrosion rate of an active metal with coupling to that without coupling [2,8]:

$$\gamma = \frac{i_{\mathrm{corr-CS\ cpl}}}{i_{\mathrm{corr-CS\ ind}}} \tag{5.1}$$

The galvanic effects calculated from the integrated Q at 21 °C (γ_{Q1}) and 50 °C (γ_{Q2}) over 72 h are higher than 1, suggesting that the oxidation rates of CS were accelerated due to coupling to SS. The polarization currents with/without coupling is higher at 50 °C than at 21 °C, which is consistent with the solution analysis shown in Figure 5.3. γ_{Q1} is smaller than γ_{Q2} indicating that the galvanic effect is larger at a higher temperature. As stated earlier, the difference between E_{cpl} and E_{corr} (shown in Figure 5.3) is greater at 50 °C than at 21°C. The larger galvanic effect at a higher temperature is consistent with the fact that CS was polarized more positively toward a higher potential at a higher temperature. This higher electrode potential indicates a higher overpotential for metal oxidation ($\mathrm{Fe}^0 \rightleftharpoons \mathrm{Fe}^{2+}{}_{(aq)}$) on CS and thereby a larger oxidation current at 50 °C than at 21 °C. At both temperatures, however, the oxidation rate after coupling is less than twice the independent corrosion rate ($\gamma_{\mathrm{Q1}}, \gamma_{\mathrm{Q2}} < 2$).

Table 5.1 The equivalent amount of dissolved Fe calculated from the polarization current compared to the dissolved Fe in solution using ICP-OES over 72 h.

Metal loss	**21 °C**		**50 °C**	
(mg/cm^2)	ICP-OES	Q	ICP-OES	Q
CS	3.05	4.77	3.59	8.50
CS-SS	4.07	6.79	6.28	13.91
γ	γ_{S1} (1.33)	γ_{Q1} (1.42)	γ_{S2} (1.75)	γ_{Q2} (1.64)

The galvanic effect based on the dissolved Fe amounts in solution (γ_S) is also calculated and its expression is shown below:

$$\gamma_S = \frac{m_{solution-CS\ cpl}}{m_{solution-CS\ ind}} \tag{5.2}$$

The galvanic effect calculated from the dissolved Fe amounts at 21 °C (γ_{S1}) is smaller than at 50 °C (γ_{S2}), which is the same as the behaviour of γ_Q with increasing temperature. Note that there are only two forms of metal corrosion products. One is oxides formed on the metal surface and the other is metal cations dissolved in the solution. At 21 °C, γ_{S1} is smaller than γ_{Q1} suggesting that after coupling to SS there is a higher fraction of oxide formation on the CS surface than dissolved Fe species in the solution. This is opposite to the case at 50 °C where γ_{S1} is larger than γ_{Q1} indicating that dissolved Fe species are more significant than oxide formation on CS after coupling. This can be explained by the effect of temperature on processes such as metal dissolution, metal oxide precipitation and phase transformation [11]. The diffusion rate of Fe species from the metal surface to the bulk solution is higher at 50 °C than at 21 °C [12]. As a result, saturation of Fe^{II} in the vicinity of the electrode takes longer to achieve, and oxide formation starts at a later time at 50 °C than at 21 °C, which results in more dissolved Fe species at a higher temperature. However, oxide formation and phase transformation are also faster at a higher temperature. Ultimately, although oxide formation starts earlier at 21 °C, there is eventually more oxide formed at 50 °C, as indicated in Table 5.1.

The values of γ_S and γ_Q over different test durations were calculated, and their time-dependent behaviours are shown in Figure 5.10. It can be observed that the overall trend for both γ_S and γ_Q is to decrease with time. Up to 20 h, the values of γ_S and γ_Q are similar. However, as corrosion progresses, these two values deviate from each other with γ_Q becoming higher than γ_S. This indicates that oxide formation on CS coupled to SS becomes more dominant at longer times.

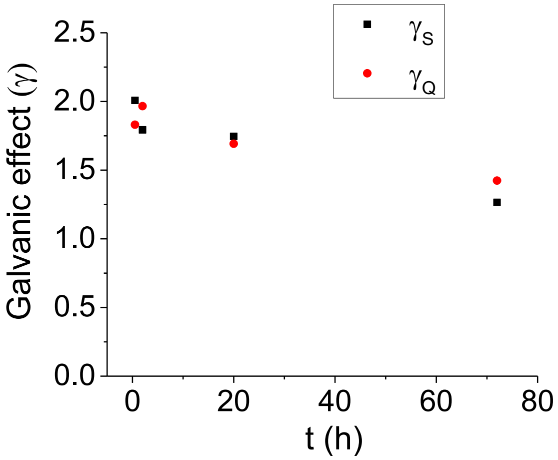

Figure 5.10 The evolution of the galvanic effect calculated based on the dissolved Fe in the solution (γ_S) and the integrated charge (γ_Q), as a function of time at 21 °C.

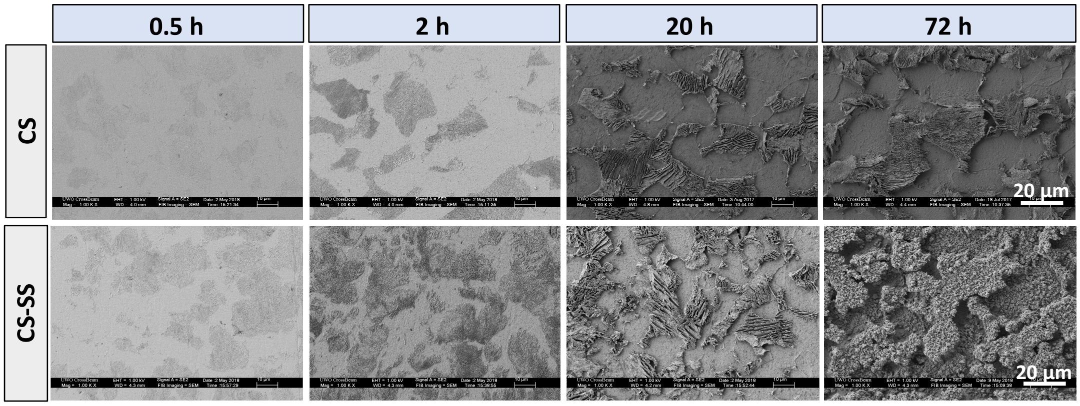

Figure 5.11 The evolution of the surface morphologies of CS with/without coupling to SS as a function of time at 21 °C.

The change in CS surface morphology revealed by SEM presented in Figure 5.11 further supports the assertion that the metal oxidation kinetics evolve with time. At an early stage (up to 2 h), metal oxidation primarily leads to Fe dissolution. With coupling, the cementite structures are more evident than during independent corrosion, which indicates that the metal oxidation rate is higher with coupling than without. The surface analysis result is consistent with the solution analysis result (Figure 5.12), which shows a higher amount of dissolved Fe for the coupled case than for the independent case. Up to 20 h, no significant granular oxides are present on both (coupled/uncoupled) CS surfaces and the difference in the surface morphology of CS between the independent and coupled cases is not significant. As shown in Figure 5.12, the amount of dissolved Fe over 20 h is higher when CS is coupled to SS than when it corrodes independently. Therefore, the main corrosion pathway of CS up to this time scale is still Fe dissolution. The amount of dissolved Fe over 72 h is also higher when CS is coupled to SS than when it corrodes independently. However, the surface of the CS corroded with coupling to SS is extensively covered with granular oxides. The results suggest that the main corrosion pathway of the overall metal oxidation process is gradually switching from metal dissolution to oxide formation. Overall, coupling to SS accelerates the oxidation rate of CS initially but this also leads to faster formation of oxides on the CS surface at the longer times, resulting in a decrease in the overall galvanic effect.

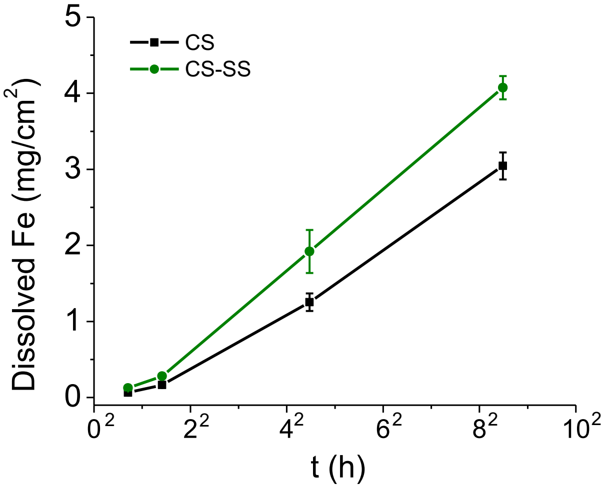

Figure 5.12 Time-dependent dissolved Fe amounts from CS with and without coupling to SS at 21 °C.

As discussed earlier in 5.3.1, different E_{cpl} values are observed at 80 °C over the 72-h test duration. The electrode potential is a good indication of the changes in an electrode surface. To understand the key controlling redox reactions at different dynamic stages the E_{cpl} obtained at 80 °C was compared to the equilibrium potentials (E_{eq}) of the different redox reactions that can occur on carbon steel (Figure 5.13) [13,14].

The chemical compositions of the oxide deposits on the CS electrode after 72-h coupling to SS at 80 °C were characterized by Raman spectroscopy. The Raman spectra of the corroded CS, recorded at two different locations on the same electrode surface, are compared with the reference spectra of standard powdered iron oxide samples in Figure 5.14. Spectrum #1 shows three major peaks at 240, 670 and 1300 cm^{-1} along with a small peak at 520 cm^{-1} that correspond to the main peaks of lepidocrocite (γ-FeOOH). However, the relative intensity of the peak at 670 cm^{-1} is higher than that of the one at 520 cm^{-1} which is opposite to what is seen in the standard spectrum of γ-FeOOH. We attribute the higher intensity at 670 cm^{-1} to the presence of magnetite (Fe_3O_4). Spectrum #1 also contains two major peaks at 310 and 420 cm^{-1} which are assigned as the presence of α-FeOOH. Spectrum #2 shows major peaks at 360, 500, 700 and 1400 cm^{-1} and a small peak at 200 cm^{-1}, which are attributed to the presence of γ-Fe_2O_3.

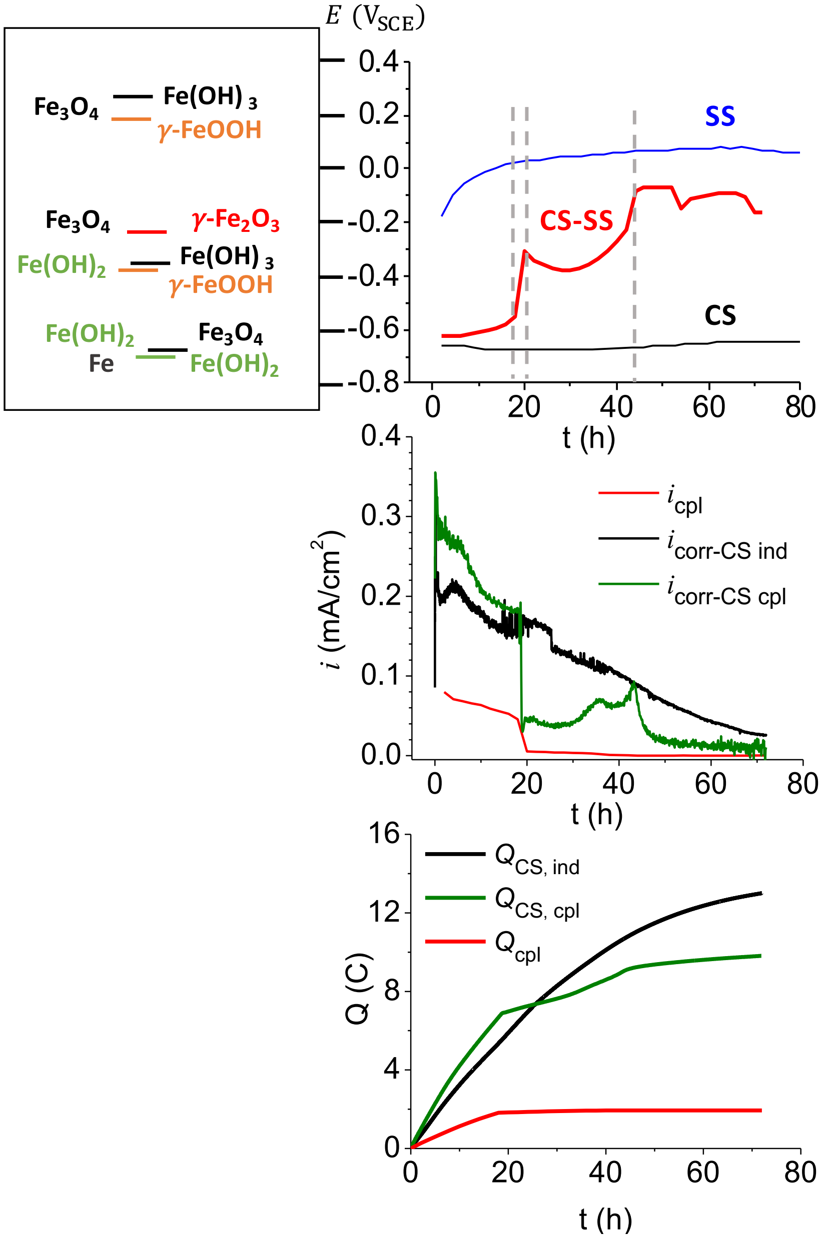

Figure 5.13 Time-dependent E_{cpl} and the corresponding $i_{\mathrm{corr-CS\ cpl}}$ measured using the DEC method at 80 °C and at pH 6.0 with the E_{eq} diagram listing different redox reactions that can occur on CS. The dashed grey lines are used to separate the E_{cpl} values into different regions.

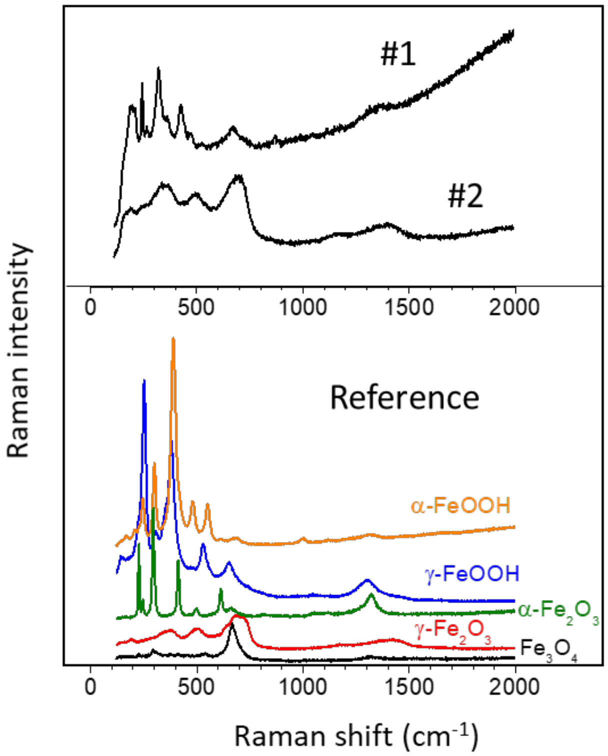

Figure 5.14 Raman spectra of the surface of the CS electrode after 72-h galvanic coupling to SS in pH 6.0 borate buffer solution at 80 °C. #1 and #2 are the spectra recorded at two different locations on the same electrode surface.

Considering the electrochemical tests results in combination with the Raman results, the following analysis of the CS corrosion dynamics was performed. As shown in Figure 5.13, four distinct stages/regions based on the change in E_{cpl} values can be observed, and they are separated by the dashed grey lines. At the first stage (up to 18 h), E_{cpl} is higher than $E_{\mathrm{eq}}(\mathrm{Fe}^0 \rightleftharpoons \mathrm{Fe(OH)_2})$ and $E_{\mathrm{eq}}(\mathrm{Fe(OH)_2} \rightleftharpoons \mathrm{Fe_3O_4})$ indicating the formation of $Fe(OH)_2$ and Fe_3O_4 on the CS surface. The formation of the Fe_3O_4 layer occurs at a relatively low rate at this pH as the solubility of $\mathrm{Fe^{II}}$ species is high at pH 6.0. Therefore, the gradual increase in E_{cpl} and decrease in $i_{\mathrm{corr-CS\ cpl}}$ is due to the accumulation of the $Fe(OH)_2$ on the surface. The second stage is a short transition stage (18-20 h) and is assigned as the rapid formation of Fe_3O_4. At the end of the first stage, enough $Fe(OH)_2$ has accumulated and it undergoes the Schikorr reaction [15,16] (a thermal condensation reaction of $Fe(OH)_2$ to Fe_3O_4). Fe_3O_4, as a semiconductor, does not inhibit electron transfer, but is, however, a major barrier to metal cations transferring from the metal oxide phase to the solution phase [17,18]. The drastic decrease in $i_{\mathrm{corr-CS\ cpl}}$ indicates that overall metal oxidation at this stage is limited by metal cation transfer instead of electron transfer. Upon reaching the third stage (20-44 h), the value of E_{cpl} is above E_{eq}($Fe(OH)_2 \rightleftharpoons \gamma$-FeOOH) or E_{eq}($Fe(OH)_2 \rightleftharpoons Fe(OH)_3$) indicating the formation of γ-FeOOH and/or $Fe(OH)_3$ is thermodynamically possible. E_{cpl} then decreases gradually, reaching its minimum value in the first 10 h before increasing again. The corresponding $i_{\mathrm{corr-CS\ cpl}}$ oscillates with time but with an overall increasing trend. Such behavior can be explained by the reversible reaction $Fe(OH)_2 \rightleftharpoons Fe(OH)_3$. However, the forward reaction (the formation of Fe^{3+}) dominates as time progresses due to the presence of O_2. The conversion of $Fe(OH)_2$ to Fe_3O_4 may still proceed, as E_{cpl} is far above E_{eq}($Fe(OH)_2 \rightleftharpoons Fe_3O_4$).

At longer times, when Fe_3O_4 has accumulated on the surface, further conversion from Fe_3O_4 to γ-Fe_2O_3 is possible. During the fourth stage (after 44 h), the change in E_{cpl} is relatively small, indicating that formation of γ-Fe_2O_3 from Fe_3O_4 is still the controlling redox reaction. The electrode surface remains relatively stable during this stage since γ-Fe_2O_3 is insoluble in water. γ-Fe_2O_3 is an oxide that can be found on steel alloys [19] and is passivating, since it can greatly hinder the charge transfer (metal cations and electrons) from the metal phase to the solution phase. Therefore, $i_{\mathrm{corr-CS\ cpl}}$ decreases to a level close to 0. It can be observed that the values of $i_{\mathrm{corr-CS\ cpl}}$ and i_{cpl} measured are similar only during this stage. Therefore, i_{cpl} can be used to represent $i_{\mathrm{corr-CS\,cpl}}$ only when the solution reduction current on the CS is negligible. Otherwise, $i_{\mathrm{corr-CS\,cpl}}$ can be greatly underestimated.

During the first stage, $i_{\mathrm{corr-CS\,cpl}}$ is larger than $i_{\mathrm{corr-CS\,ind}}$, which is similar to the observations at lower temperatures that coupling to SS increases the oxidation rate of CS. However, a value of $i_{\mathrm{corr-CS\,cpl}}$ lower than $i_{\mathrm{corr-CS\,ind}}$ is measured in the following assigned stages. The overall accumulated charge over 72 h for the oxidation of CS when it is coupled to SS is lower than when it is independently corroded (Figure 5.13). The dissolved Fe in solution for the CS-SS couple at 80 °C is also lower than that observed at lower temperatures and during the independent corrosion of CS, as shown in Figure 5.3. These observations indicate that the effect of galvanic coupling to SS on the corrosion rate of CS has a strong time-dependence. Initially, the corrosion rate of CS is accelerated when coupled to SS. However, this also leads to much faster oxide formation and growth on CS, resulting in a suppression of the subsequent oxidation rate or Fe dissolution at longer times. Increasing temperature further accelerates the progression of corrosion on CS and therefore such behaviors are observed much earlier.

5.4 Conclusions

The galvanic corrosion of carbon steel (CS) and stainless steel (SS 309) was investigated in different aqueous environments (pH 6.0, 21 °C, 50 °C and 80 °C). The corrosion currents of CS when galvanically coupled to SS were measured using both conventional methods and the DEC method. Conventionally, coupling current is taken to represent the corrosion rate or the increase in corrosion rate of the more active metal (CS) in a galvanic couple. However, such interpretations are restricted by the underlying assumptions that either the reduction current on the more active metal is negligible or remains the same as during independent corrosion. The limitations of conventional methods can be addressed by the use of the DEC method which allows the direct and more accurate measurement of the corrosion rates for both independent corrosion and galvanic corrosion systems. The corrosion rate of SS is negligible compared to that of CS under all studied conditions. With the DEC results, the evolution of the galvanic effect can be observed and understood better. The evolution of the surface morphologies of the corroded CS coupons, and the dissolved Fe amounts in the solution over different durations, were also investigated to complement the electrochemical results. Overall, the galvanic effect has a strong time-dependence. Initially, coupling to SS and/or increasing temperature accelerates the oxidation rate of CS. However, they also accelerate the formation and growth of oxides on CS, suppressing the subsequent oxidation of CS. As a result, the increase in the CS corrosion rate due to galvanic coupling diminishes with time.

5.5 References

[1] R. Francis, Galvanic Corrosion: A Practical Guide for Engineers, 2nd ed., NACE International, 2017.

[2] C.F. Dong, K. Xiao, X.G. Li, Y.F. Cheng, J. Mater. Eng. Perform., 20 (2011) 1631–1637.

[3] C.F. Dong, K. Xiao, X.G. Li, Y.F. Cheng, Wear, 270 (2010) 39–45.

[4] J. Soltis, K.A. Lichti, Corros. Sci., 68 (2013) 162–167.

[5] T.E. Standish, L.J. Braithwaite, D.W. Shoesmith, J.J. Noël, J. Electrochem. Soc.,

166 (2019) C3448–C3455.

[6] X. Feng, J. Liu, C. Hang, Z. Lu, Y. Jiang, Y. Xu, D. Chen, Int. J. Electrochem. Sci., 11 (2016) 5226–5233.

[7] C.M. Abreu, M.J. Cristóbal, M.F. Montemor, X.R. Nóvoa, G. Pena, M.C. Pérez, Electrochim. Acta, 47 (2002) 2271–2279.

[8] F. Mansfeld, CORROSION, 29 (1973) 403–405.

[9] S. Qian, D. Qu, J. Appl. Electrochem., 40 (2010) 247–256.

[10] M. Li, D. Guo, J.M. Joseph, O. Yong, J.C. Wren, Galvanic Corrosion of Carbon Steel and Stainless Steel Couples: Effects of γ-Radiation and Solution Environment, in: WM2020 Conference, Phoenix, AZ, 2020.

[11] K. Daub, X. Zhang, L. Wang, Z. Qin, J.J. Noël, J.C. Wren, Electrochim. Acta, 56 (2011) 6661–6672.

[12] A.J. Bard, L.R. Faulkner, Electrochemical Methods Fundamentals and Applications, 2nd ed., John Wiley & Sons, Inc., 2001.

[13] A.Y. Musa, J.C. Wren, Corros. Sci., 109 (2016) 1–12.

[14] M. Pourbaix, Atlas of Electrochemical Equilibria in Aqueous Solutions, 1st ed., Pergamon Press, Oxford, 1966.

[15] M. Booy, T.W. Swaddle, Can. J. Chem., 56 (1978) 402–403.

[16] R.O. Rihan, S. Nešić, Corros. Sci., 48 (2006) 2633–2659.

[17] K. Daub, X. Zhang, J.J. Noël, J.C. Wren, Corros. Sci., 53 (2011) 11–16.

[18] W. Xu, K. Daub, X. Zhang, J.J. Noel, D.W. Shoesmith, J.C. Wren, Electrochim. Acta, 54 (2009) 5727–5738.

[19] R.M. Cornell, U. Schwertmann, The Iron Oxides Structure: Properties, Reactions,

Occurrences and Uses, 2nd ed., Weinheim, New York, 2003.

Chapter 6. Effect of Gamma-Radiolysis on the Corrosion Dynamics of Galvanically Coupled Dissimilar Metals

6.1 Introduction

The annular air gap in the nuclear reactor is exposed to a continuous flux of ionizing radiation, since it is in the vicinity of the reactor core. When ionizing radiation is present, water decomposes, resulting in the production of strong oxidants such as H_2O_2 and •OH [1] which can change the solution redox properties and subsequently affect the corrosion behaviour of the weld region of interest. Among the three types of ionizing radiation, γ-radiation is of particular concern due to its higher penetration depth compared to α-radiation and β-radiation [1]. Although steel corrosion has been studied for a long time (throughout the 20th and 21st centuries), research on radiation-induced corrosion is very limited. Moreover, until now no relevant work has been performed to study the galvanic corrosion of dissimilar steels in a radiation field.

In this chapter, the corrosion dynamics in the presence of γ-radiation of individual carbon steel (CS) and stainless steel (SS 304 and SS 309), and the galvanic corrosion of a CS-SS 309 couple were investigated by performing electrochemical measurements. This was augmented by post-analyses of solutions and surfaces.

6.2 Experimental

6.2.1 Electrode and electrolyte preparation

The electrochemical tests carried out in this study employ a three-compartment cell which consists of a reference electrode, a Pt mesh counter electrode and a metal working electrode. The working electrode is either a CS/SS 304/SS 309 electrode or a CS-SS 309 couple not welded together (not even in physical contact), but electrically connected using a potentiostat. The composition of the materials is tabulated in Chapter 4 and hence not repeated here. The exposed surface areas of each CS/SS 304 and SS 309 working electrode were limited to 0.455 cm^2 and 1.267 cm^2 respectively by covering the surrounding areas with Teflon or Parafilm (when radiation present). A saturated calomel electrode (SCE) (Fisher Scientific) was used for experiments performed in the absence of radiation, while an Hg/HgO reference electrode was used for tests in the presence of radiation. The solutions used in this study were either pH 6.0 or 10.6 sodium borate buffer, and the solution volume was 0.5 L. All experiments were carried out at 21 °C.

6.2.2 Coupling potential and coupling current measurements

The coupling potential (E_{cpl}) and coupling current (i_{cpl}) of the CS-SS couple in the absence of radiation were simultaneously measured using two channels of a potentiostat. The details of this set-up are the same as described in Chapter 5. Due to the complexity of using two channels under irradiated conditions, the measurements of E_{cpl} and i_{cpl} in the presence of radiation were carried out in two separate tests.

6.2.3 Irradiation tests

Irradiation tests were carried out in a ^{60}Co gamma cell. The electrochemical cells were placed in a loading chamber which descended into the irradiation chamber via a vertical lift. A digital timer was programmed to terminate the radiation exposure by returning the loading chamber to its raised position after the set time-point was reached. Electrochemical measurements beyond 20 h in the presence of radiation were not performed due to the unavailability of a reference electrode that is stable under these conditions. Over the timeframe of the experiments documented in this chapter, the dose rate was 2.8 kGy/h (1 Gy = 1 J/kg).

6.2.4 Dual-electrochemical cell measurement

A simplified dual-electrochemical cell (DEC) set-up, presented in Figure 6.1, was used for the corrosion current measurements in this study. The electrochemical cell was purged with Ar gas and measurements were carried out in the absence of radiation. The CS or SS working electrode in the cell was polarized to the E_{corr} or E_{cpl} profile that had previously been recorded in the presence of radiation. This was achieved by directly applying the electrode potential using a step function to approximate the actual potential profile.

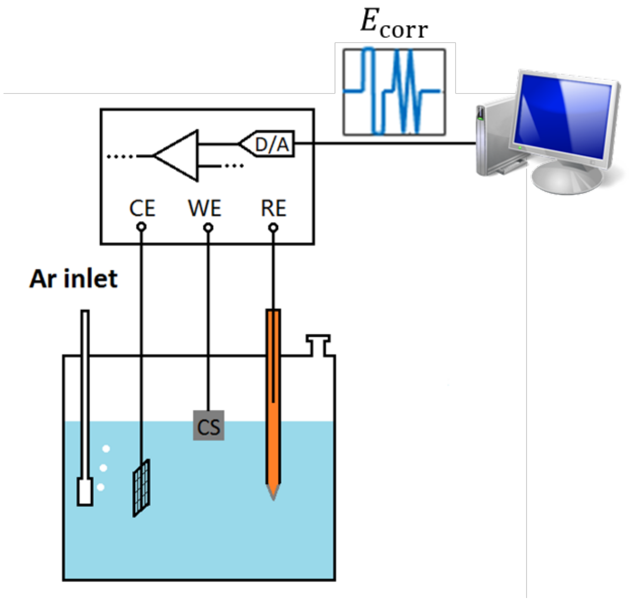

Figure 6.1 Schematic illustration of the simplified DEC set-up.

6.2.5 Corrosion tests

The set-up of the corrosion tests is the same as for the electrochemical tests. After 5-min cathodic cleaning at −1.1 V_{SCE}, coupons were left under open circuit conditions. Due to the space restrictions of the gamma cell chamber, corrosion tests in the presence of radiation were investigated only at 21 °C.

6.2.6 Surface characterization and solution analysis

After the individual CS, SS 304, SS 309 electrodes and the galvanically coupled CS-SS had corroded for different durations, they were dried with Ar. The surfaces were then analyzed by optical microscopy and scanning electron microscopy (SEM). Optical microscopy was performed using a Leica DVM6. The electrode surface morphology and cross sections were examined using a LEO (Zeiss) 1540XB SEM equipped with a focused ion beam (FIB). The dissolved iron concentration in the solution after each test was analyzed using a Perkin Elmer Avio 200 inductively coupled plasma optical emission spectrometer (ICP-OES). Prior to the solution analysis the samples were digested using nitric acid (trace analytical grade, Fisher Scientific) to dissolve any colloidal particles present in the test solutions. Therefore, the measured dissolved iron concentration may include any colloid particles, if present.

6.3 Results and Discussion

6.3.1 Effect of γ-radiation on the microgalvanic corrosion of CS

The metallurgical structure of CS consists of a pure α-Fe phase, and a pearlite phase consisting of alternating cementite (mainly comprises Fe_3C) and α-Fe layers. Cementite is less active than α-Fe so there is a concern that the presence of cementite will accelerate the dissolution of α-Fe in the pearlite phase, resulting in more Fe dissolution from the pearlite phase than from the pure α-Fe phase [2]. This phenomenon caused by microstructural differences is known as microgalvanic corrosion and is often observed on Mg alloys [3–5]. To investigate the possibility of microgalvanic corrosion on CS, we imaged cross-sections of the surface produced using a focused ion beam (FIB), after it had been corroded independently in the presence and absence of radiation. It can be observed from Figure 6.2 that the pure α-Fe phase and α-Fe layers in the pearlite phase are at the same height for both the non-irradiated and irradiated cases. The SEM images show many different orientations of the cementite layers on the surface; however, the dissolution fronts of the α-Fe (whether in the pure α-Fe phase or in the pearlite phase), move at the same rate. That is, no preferential Fe dissolution from the pearlite phase can be observed, indicating negligible microgalvanic effect on the CS itself.

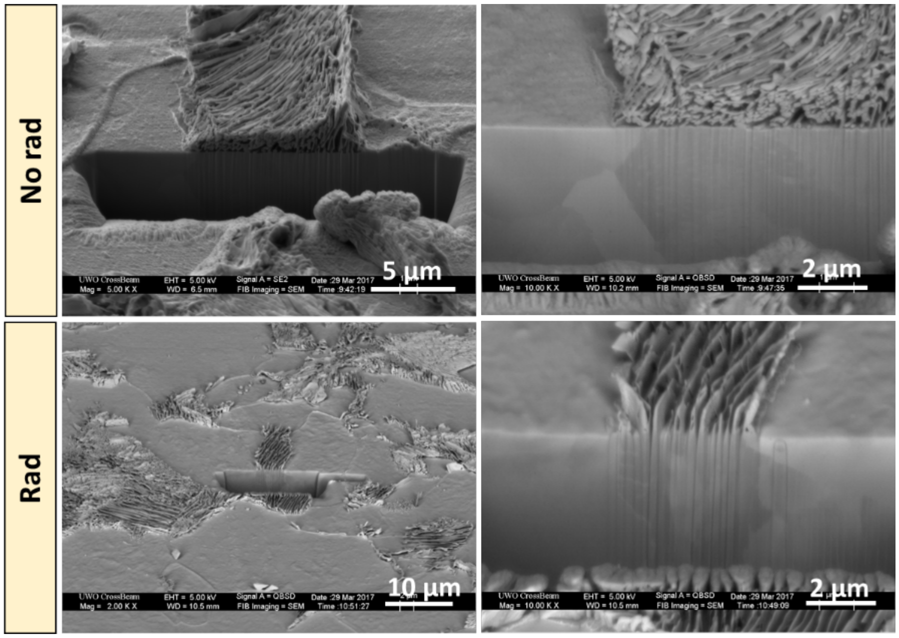

Figure 6.2 The FIB cross-section images of CS over 24-h corrosion at pH 6.0 in the absence of radiation and over 72-h corrosion in the presence of radiation.

6.3.2 Effect of γ-radiation on the independent corrosion of individual alloys

The effect of γ-radiation on the independent corrosion of CS, SS 304 and SS 309 was investigated by monitoring the E_{corr} for 20 h at 21 °C in the presence of radiation (Figure 6.3).

For each individual alloy at both pHs, the E_{corr} value increases. This can be attributed to the radiolytic decomposition of water to form strong oxidizing species, particularly H_2O_2 which is considered to be the key radiolytically produced oxidant at room temperature [1,6]. This increase in E_{corr} with γ-irradiation has been observed for many different alloys, but the degree of increase varies considerably depending on the alloy and solution pH [6–12]. For SS 304 and SS 309 at both pHs, and CS at pH 10.6, the E_{corr}

values at 20 h in the presence of radiation are about 200±20 mV higher than those obtained at the same time but in the absence of radiation. After 18-h exposure to γ-radiation, the E_{corr} profiles of SS 304 and SS 309 at pH 6.0 and the E_{corr} profiles of CS, SS 304 and SS 309 at pH 10.6 have almost converged. Rather than showing a great difference between the irradiated and non-irradiated conditions, the E_{corr} value obtained on CS at pH 6.0 with radiation present is only slightly higher than in the absence of radiation (about 20 mV).

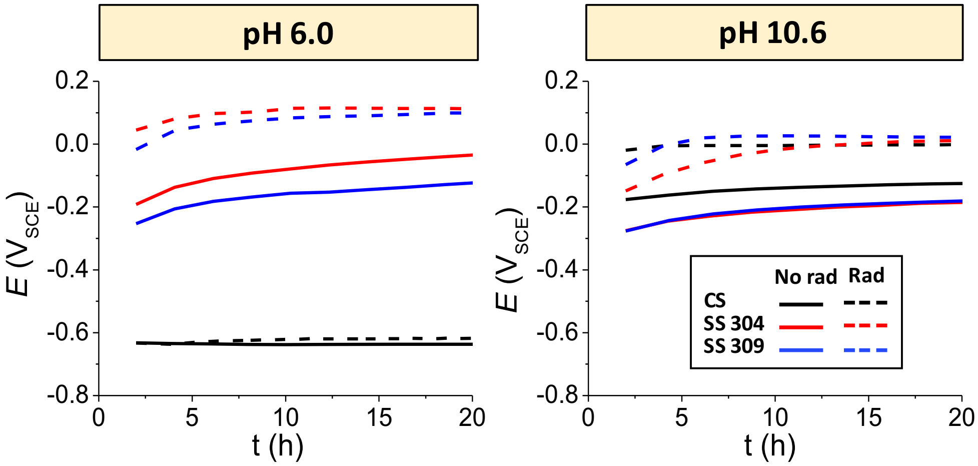

Figure 6.3 E_{corr} of CS (black), SS 304 (red) and SS 309 (blue) in pH 6.0 and pH 10.6 buffer solutions at 21 °C in the absence of radiation (solid lines) and in the presence of radiation (dashed lines).

After 20-h immersion, the coupons were taken out and their corroded surfaces were characterized by SEM, and the results are shown in Figure 6.4. The surfaces of SS 304 and SS 309 at both pHs are similar and hence only the surfaces of SS 309 are presented here. When radiation is present, polishing scratches are observed on the surfaces of SS 309 at both pHs, and CS at pH 10.6, indicating a minimal extent of corrosion. This is consistent with the low amount of dissolved Fe in the solutions analyzed by ICP-OES (shown in Figure 6.5). For CS at pH 6.0 and under radiation, the cementite skeleton and grain boundary were again observed, indicating the high dissolution rate of Fe. This is further confirmed by the solution analysis which shows that the dissolved Fe amount from CS at pH 6.0 is much higher than for the other studied cases. However, no significant difference can be observed by SEM between the irradiated and non-irradiated surfaces of CS at pH 6.0. The corrosion dynamics of CS at this pH were further investigated by imaging its surface using the optical microscope (see discussion later).

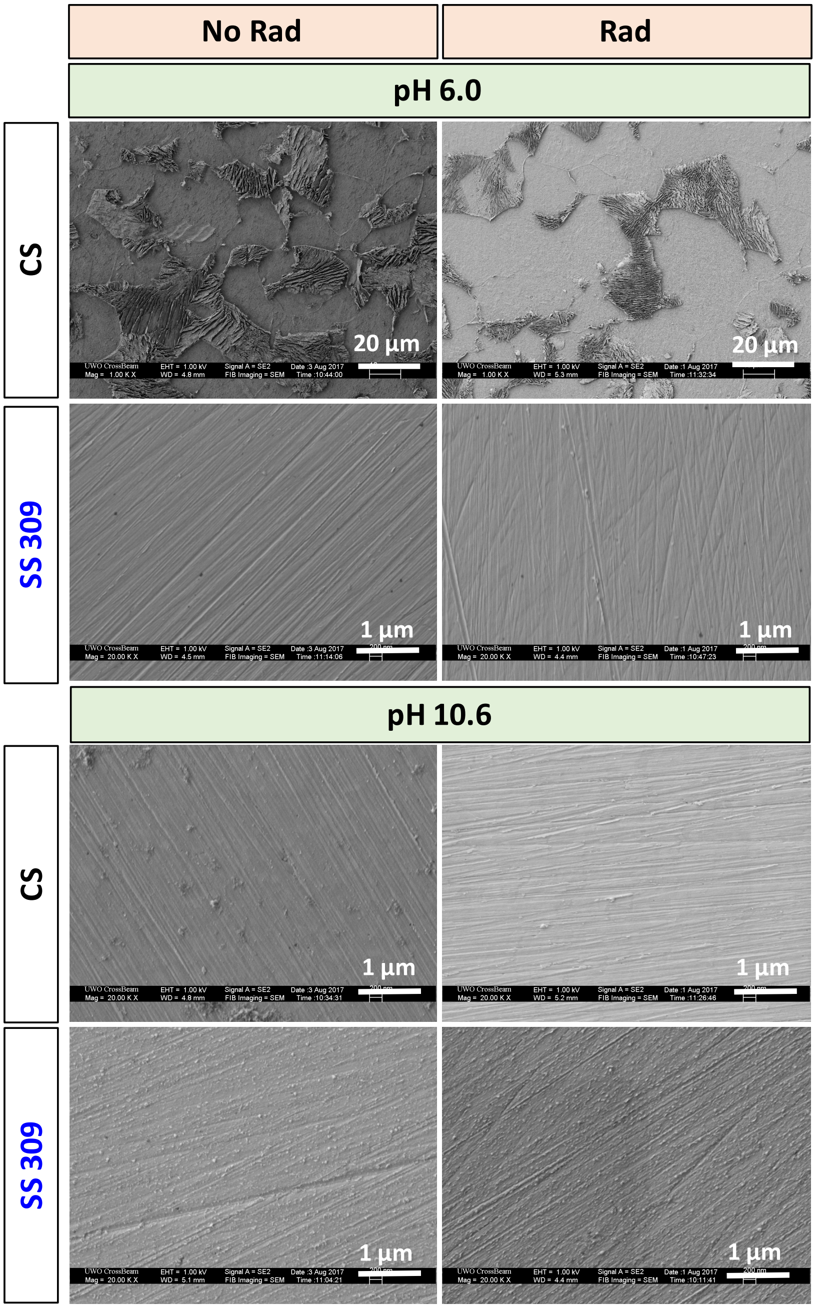

Figure 6.4 SEM micrographs of CS and SS 309 surfaces after 20 h corrosion in pH 6.0 and 10.6 borate buffer solutions at 21 °C in the absence and presence of radiation.

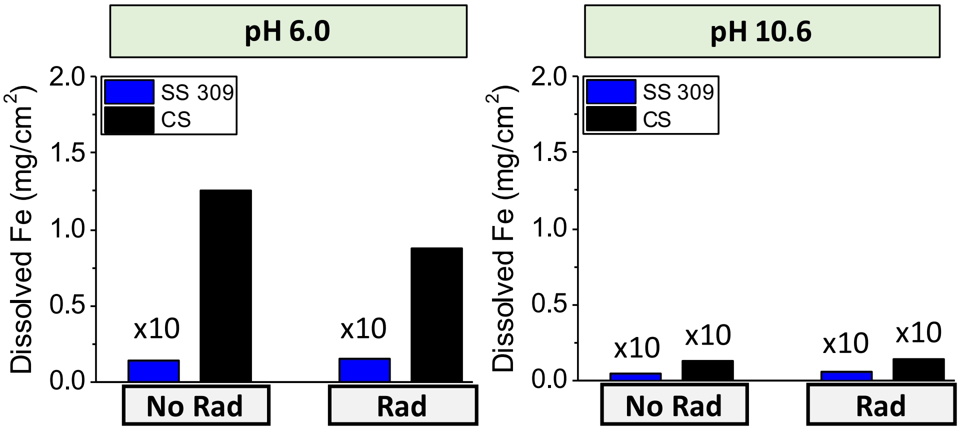

Figure 6.5 Dissolved Fe amounts in the solutions after 20-h independent corrosion of CS and SS 309 in the absence and presence of radiation. The values presented here for SS 309 at both pHs and CS at pH 10.6 are magnified by 10 times.

In summary, the electrochemical tests, surface analysis and solution analysis results all indicate that the variations in the independent corrosion behaviours between the two types of stainless steel (SS 304 and SS 309) and between CS and SS 309 are not significant. Therefore, galvanic corrosion of the SS 304-SS 309 couple at both pHs, and of the CS-SS 309 couple at pH 10.6 will be negligible, even in the presence of radiation. The subsequent studies on radiation-assisted galvanic corrosion concentrated on the CS-SS 309 couple (referred to as CS-SS hereafter) at pH 6.0 due to the large observed difference between the independent corrosion behaviours of these two alloys at this pH.

6.3.3 Effect of γ-radiation on the galvanic corrosion of the CS-SS couple

The effect of γ-radiation on the galvanic corrosion of the CS-SS couple was investigated by monitoring the coupling potential (E_{cpl}) and the coupling current (i_{cpl}) in the presence of radiation. The results over 20-h corrosion, together with the dissolved Fe amounts in the solutions, are presented in Figure 6.6. Corrosion rate measurement of CS using the DEC method was also performed and the results are shown in Figure 6.7.

The E_{cpl} value of the CS-SS couple is higher in the presence of γ-radiation than in the absence of radiation. This is due to the presence of highly oxidizing species such as H_2O_2 produced from water radiolysis. As discussed earlier, the surface of the SS remains clean in the presence of radiation and the amount of Fe dissolved from the SS over 20-h corrosion is negligible compared to that from CS at pH 6.0. Therefore, the total dissolved Fe amounts from the CS-SS couple presented in Figure 6.6 were normalized to the surface area of CS.

At pH 6.0, the E_{cpl} of the CS-SS couple is slightly higher (about 30 mV) than the E_{corr} of CS with and without radiation present. Both values vary with time in the presence of radiation, decreasing slightly initially and then increasing at later times, similar to the behaviour observed at 50 °C in the absence of radiation (discussed in Chapter 5). The i_{cpl} remains nearly constant with time in the presence of radiation (increasing slightly over the first 5 h before reaching a steady state value). The i_{cpl} value in the presence of radiation is the same as in the absence of radiation at 2 h, but about two or three times higher after 10 h. In both the absence and presence of radiation, the dissolved Fe amount from the CS-SS couple is higher than from the independently corroded CS indicating a higher Fe dissolution rate for the CS-SS couple. However, the overall dissolved Fe amount for the CS-SS couple after 20-h corrosion is lower in the presence of radiation than in its absence. This phenomenon was also observed for the independently corroded CS. As stated earlier in Chapter 5, most research tends to use coupling current to represent the dissolution rate of the more active metal (CS in our case). However, the solution analysis results presented here indicate that such a correlation does not work for the galvanic corrosion of CS-SS in the presence of radiation.

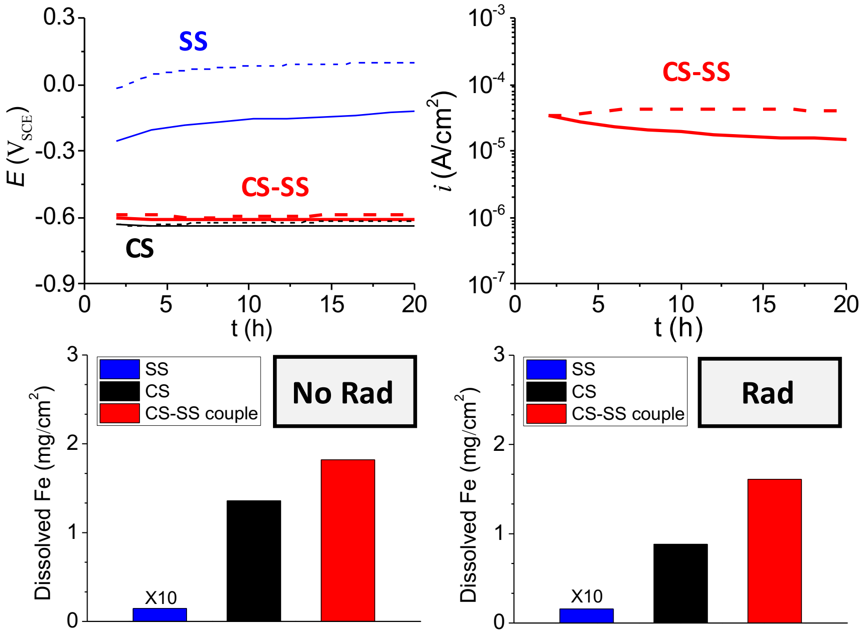

Figure 6.6 Evolution of E_{corr}, E_{cpl} and i_{cpl} with time during corrosion of independent CS, SS and the CS-SS couple in the presence (dashed line) and absence of radiation (solid line) and their total dissolved Fe in pH 6.0 solutions after 20-h corrosion.

The corrosion currents for CS in the presence of radiation were measured using the DEC method and the results are presented in Figure 6.7. Though the value of E_{cpl} is only slightly higher than the E_{corr} of CS under both non-irradiated and irradiated conditions (Figure 6.6), $i_{\mathrm{corr-CS\ cpl}}$ is about two times higher than $i_{\mathrm{corr-CS\ ind}}$ (Figure 6.7), indicating that active dissolution of CS is taking place.

The time-dependence of the corrosion current closely follows the time-dependence of the electrode potential. The presence of γ-radiation has a negligible effect on the corrosion current of CS corroding independently ($i_{\text{corr}-\text{CS ind}}$) at early times (< 5 h). However, $i_{\text{corr}-\text{CS ind}}$ starts increasing with time in the presence of radiation while it remains constant with time in the absence of radiation. For the CS coupled to SS, γ-radiation also has a negligible effect on its corrosion rate ($i_{\text{corr}-\text{CS cpl}}$) initially (< 10 h). At longer times $i_{\text{corr}-\text{CS cpl}}$ increases in the presence of radiation while it remains constant in the absence of radiation. The observed effect of γ-radiation on $i_{\text{corr}-\text{CS cpl}}$ is opposite to that for i_{cpl}. Furthermore, i_{cpl} is lower than $i_{\text{corr}-\text{CS cpl}}$ by a factor of two to four whether radiation is present or not. These observations further support our previous statement that i_{cpl} does not necessarily represent the oxidation (or corrosion) current of CS.

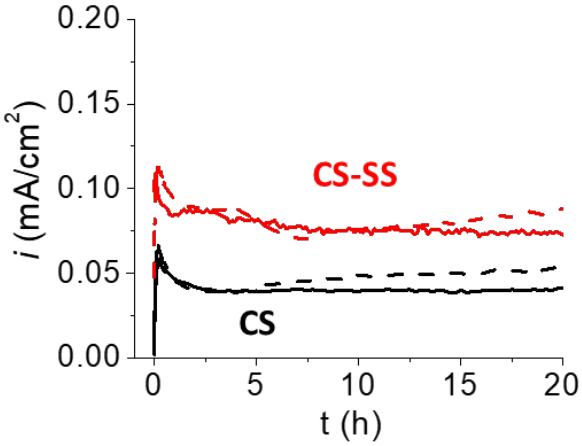

Figure 6.7 The corrosion currents of CS measured using the DEC method during its independent corrosion ($i_{\text{corr}-\text{CS ind}}$, black lines) and galvanic corrosion while coupled to SS ($i_{\text{corr}-\text{CS cpl}}$, red lines) in the presence of radiation (dashed lines) and absence of radiation (solid lines).

6.3.4 Corrosion progression on CS

Time-dependent corrosion tests on CS were carried out with/without the presence of radiation. The surface morphologies of CS were imaged using SEM and are presented in Figure 6.8. At any given time during corrosion, dissolution of the α-Fe phase is occurring, as indicated by the presence of the cementite structure on the surface. At an early stage (up to 2 h), there is more exposure of cementite layers on the surface for CS coupled to SS, indicating the dissolution rate is faster with coupling than without. Minimal changes can be observed between the irradiated case and the non-irradiated one, indicating that the effect of radiation is not significant at this stage. These observations are consistent with the DEC results which show that galvanic coupling to SS is more effective in increasing the dissolution rate of CS than radiation at this stage. At longer times (up to 72 h), the skeleton of cementite is more clearly visible indicating a greater extent of Fe dissolution. However, no significant variation among the different cases can be observed from the SEM images. Iron oxides have distinct colours; for example, Fe_3O_4 is black, γ-FeOOH is orange and α-Fe_2O_3 is red [13]. Therefore, optical images of coupons after 20-h and 72-h corrosion were taken to observe any oxide colour differences and the results are presented in Figure 6.9. Note that the optical images were taken after the samples had been washed with deionized water and dried with argon gas. During this process, some of the oxides that were originally uniformly distributed on the CS surfaces were removed, resulting in the non-uniform distribution of oxides observed.

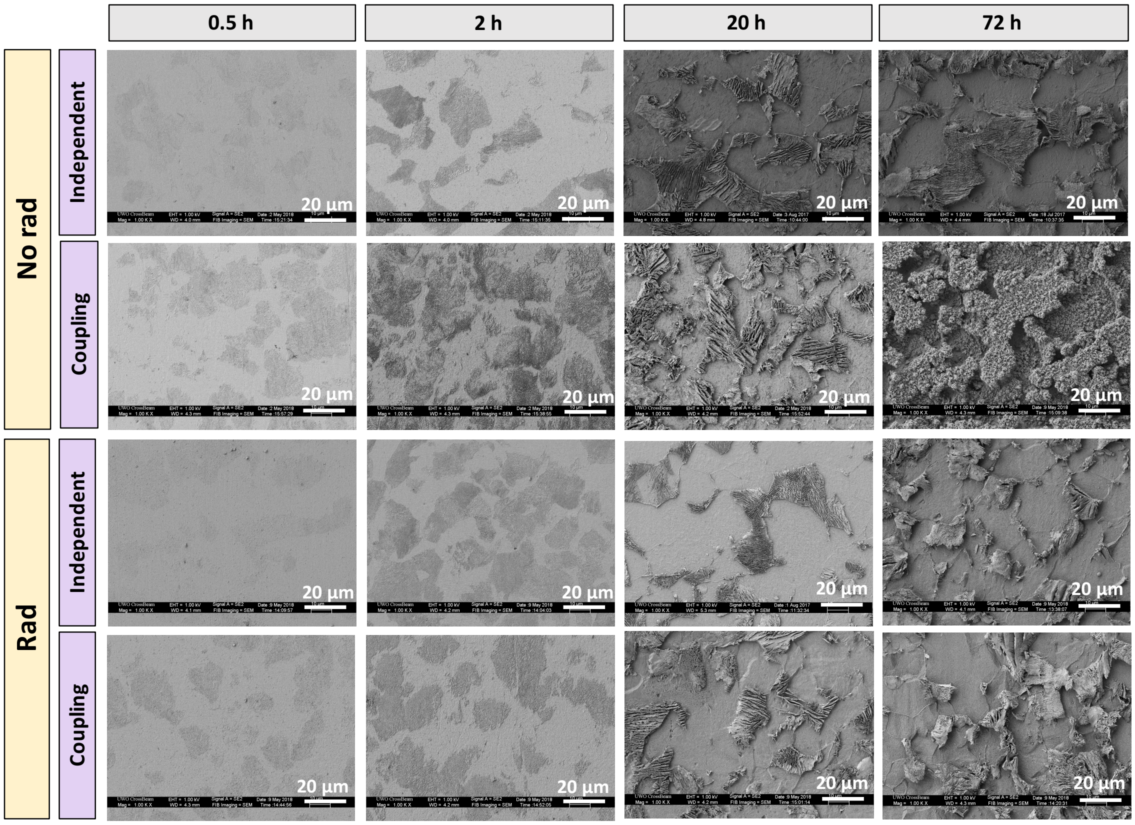

Figure 6.8 Evolution of surface morphologies of CS with and without coupling to SS in the presence and absence of radiation.

Oxide formation starts earlier on CS in the presence of radiation, subsequently suppressing its overall oxidation. At 20 h, some remaining yellowish oxides (γ-FeOOH) can be observed on the edge of the irradiated CS surface while no noticeable yellowish oxides can be observed for the non-irradiated case. A similar phenomenon was also observed on CS galvanically coupled to SS. This can be explained by the participation of radiation in both the interfacial electrochemical redox reactions and chemical reactions (see further discussion later). The E_{corr} values for CS and the E_{cpl} values lie slightly higher than E_{eq}($Fe(OH)_2 \rightleftharpoons Fe_3O_4$) (shown in Figure 6.10) indicating the formation of Fe_3O_4 on the CS surface, which is consistent with the underlying black oxides observed from the optical images. The E_{corr} values for CS and the E_{cpl} values obtained when radiation is present are lower than E_{eq}($Fe(OH)_2 \rightleftharpoons \gamma$-FeOOH), indicating that the formation of γ-FeOOH is not thermodynamically favored. However, chemical reactions other than electrochemical ones can occur during the corrosion process. When metal oxidation occurs at the metal-solution interface and produces $Fe^{2+}_{(aq)}$, $Fe(OH)_2$ hydrogel produced via hydrolysis can deposit on the surface. •OH and H_2O_2, as the most oxidizing water radiolysis products, can quickly oxidize $Fe(OH)_2$ into $Fe(OH)_3$. The $Fe(OH)_3$ on the metal surface can then undergo dehydration forming γ-FeOOH (yellow oxides) [11]. Such chemical reactions involving oxidation of Fe^{II} to Fe^{III} can also occur by reaction with dissolved O_2 in solution. However, the oxidation by O_2 is much slower than by •OH and H_2O_2 [1,14]. Moreover, as shown in Figure 6.7, the overall oxidation rate of CS in the presence of radiation is higher than in its absence. The higher oxidation rate, or a higher concentration of $Fe^{2+}_{(aq)}$ near the metal surface, can further accelerate the chemical processes described above. Therefore, earlier oxide formation is observed for the irradiated cases. After 20-h corrosion in the presence of radiation, the higher amounts of oxides on the surface (shown in Figure 6.9) and lower dissolved Fe in the solution (shown in Figure 6.11) suggest that radiation contributes more to oxide formation on CS than to dissolved Fe in solution. When radiation is present, more yellowish oxides remain on the surface for the coupled case than for the independent one, suggesting a thicker or more adhered oxide layer on the CS surface due to coupling. This could be explained by the contribution of galvanic coupling to the acceleration of the chemical processes, since the oxidation rate of CS is higher with coupling to SS than without. Meanwhile, solution analysis detected a greater amount of dissolved Fe for the coupled case. These two observations indicate that for CS coupled to SS, the oxides formed after this duration are not sufficiently protective to prevent the acceleration of the oxidation rate.

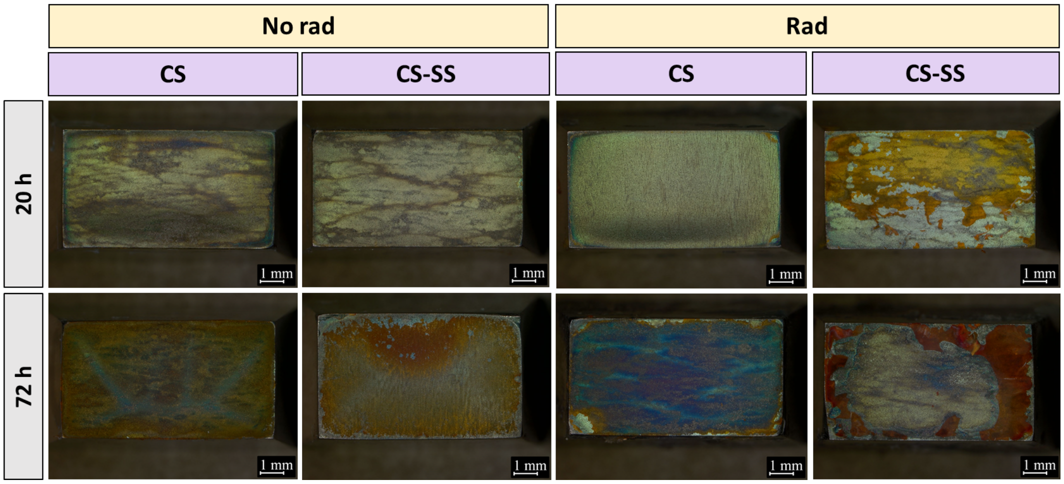

Figure 6.9 Optical images of CS after 20-h and 72-h corrosion with and without coupling to SS and in the presence and absence of radiation.

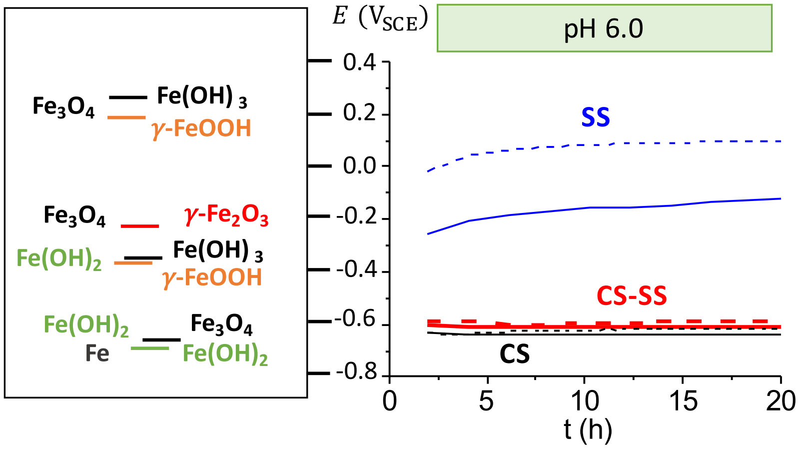

Figure 6.10 Comparison between the E_{corr}, E_{cpl} values at 21 °C in the presence (dashed line) and absence of radiation (solid line) and the electrochemical equilibrium potentials of different redox reactions that can occur on steel alloys.

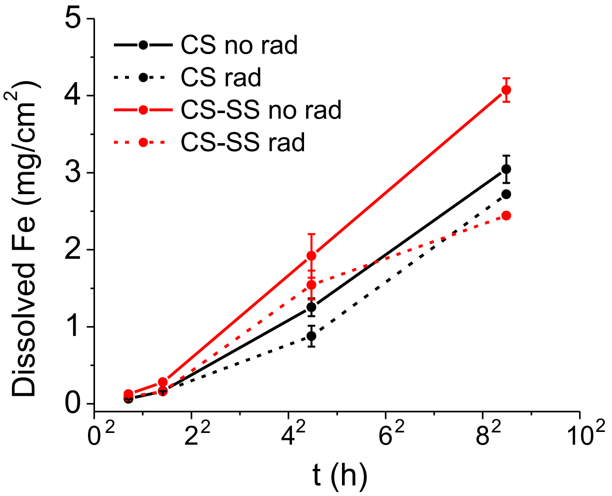

Figure 6.11 Time-dependent amounts of Fe dissolved from CS with and without coupling to SS in the presence and absence of radiation.

At 72 h, the entire surface of CS is covered with oxides whose colours are more reddish than yellowish, particularly for the irradiated cases. As discussed earlier, α-Fe_2O_3 is red which matches our observations. However, α-Fe_2O_3 is usually only formed at high temperatures [15]. Therefore, the reddish oxides in our cases are assigned as γ-FeOOH but with a greater film thickness. For all four cases, the amount of total dissolved Fe increases as corrosion progresses indicating the absence of any uniformly distributed passive oxides. As mentioned earlier, the dissolved Fe amount over 20 h for both independent CS and galvanically coupled CS-SS is lower in the presence of radiation than in its absence. This phenomenon is again observed at this longer time period (shown in Figure 6.11). After 72 h in the presence of radiation, however, the dissolved Fe amount from the CS coupled to SS is lower than without coupling, which is opposite to the case at 20 h. Based on the surface and solution analyses, it can be concluded that irradiation and coupling to SS initially increase the oxidation rate of CS the most. However, this does not persist, as irradiation and coupling also lead to earlier and faster formation of oxides on the electrode surface. After more protective or less-soluble oxide layers have formed on CS over longer time periods, further Fe dissolution is suppressed.

6.4 Conclusions

The effect of radiation on the galvanic corrosion of carbon steel-stainless steel welds was investigated by studying the corrosion behaviors of individual alloys (CS, SS 304 and SS 309) and galvanically coupled CS-SS (Type 309) in different aqueous environments (pH 6.0 and 10.6, 21 °C, with/without irradiation). A combination of coupon immersion tests and electrochemical experiments was performed. The time-dependent surface morphologies of the corroded CS, and the dissolved Fe amounts in the solutions were also examined to complement the electrochemical results.

The FIB cut cross-section images of CS show that micro-galvanic corrosion of CS is not significant both in the absence and presence of radiation. In the presence of γ-radiation, the E_{corr} values of all three alloys increase and this increase varies depending on the alloy and the pH. The corrosion behaviours of SS 304 and SS 309 are similar at both pHs, indicating negligible galvanic corrosion of the SS 304-SS 309 couple. For the CS-SS couple, however, the galvanic effect varies with the solution pH. Generally, in a basic environment (pH 10.6), galvanic corrosion of the CS-SS couple is not significant even in the presence of strong oxidants (radiolysis products). In an acidic to near neutral environment (pH 6.0), the galvanic effect is more pronounced. Coupling to SS and irradiation at this pH work synergistically in affecting the corrosion progression of CS and their effects vary with time. Over a short time period (up to 2 h), the effect of radiation on accelerating the rate of CS corrosion (($Fe^0 \rightleftharpoons Fe^{2+}_{(aq)}$) is not significant, whereas the effect of galvanic coupling is more pronounced. As corrosion progresses (up to 20 h) and $Fe(OH)_2$ gel forms on the metal surface, radiation can accelerate the formation of ferric species on the surface via chemical oxidation of $Fe(OH)_2$ and highly oxidizing species (•OH and H_2O_2) in the solution. In comparison, galvanic coupling mainly increases the oxidation rate of CS, leading to more dissolved Fe in the solution. However, the higher oxidation rate of CS due to galvanic coupling can also contribute to the acceleration of the chemical reaction processes. Over longer time periods (up to 72 h), as more oxide layers mainly consisting of insoluble ferric species form on the surface, further metal oxidation of CS is suppressed. Among the four studied cases, the combination of irradiation and coupling to SS accelerate the progression of corrosion on CS the most. Initially, irradiation and coupling to SS increase the corrosion rate of CS. However, they also lead to much faster oxide formation and growth on CS after the saturation limits of metal cations near the surface are reached, resulting in the suppression of subsequent Fe dissolution at longer times.

6.5 References

[1] J.W.T. Spinks, R.J. Woods, An Introduction to Radiation Chemistry, John Wiley & Sons, Inc., New York, 1990.

[2] W.D. Callister, Jr., D.G. Rethwisch, Materials Science and Engineering: An Introduction, 8th ed., John Wiley & Sons, Inc., New York, 2009.

[3] M. Zhao, M. Liu, G. Song, A. Atrens, Corros. Sci., 50 (2008) 1939–1953.

[4] R.M. Asmussen, The Influence of Microstructure on the Corrosion of Magnesium

Alloys, The University of Western Ontario, London, ON, 2014.

[5] L.J. Liu, M. Schlesinger, Corros. Sci., 51 (2009) 1733–1737.

[6] K. Daub, X. Zhang, J.J. Noël, J.C. Wren, Electrochim. Acta, 55 (2010) 2767–2776.

[7] K. Daub, X. Zhang, J.J. Noël, J.C. Wren, Corros. Sci., 53 (2011) 11–16.

[8] Q.W. Knapp, J.C. Wren, Electrochim. Acta, 80 (2012) 90–99.

[9] M. Behazin, M.C. Biesinger, J.J. Noël, J.C. Wren, Corros. Sci., 63 (2012) 40–50.

[10] A.Y. Musa, J.C. Wren, Corros. Sci., 109 (2016) 1–12.

[11] D. Guo, Corrosion Dynamics of Carbon Steel in Used Fuel Container Environments, The University of Western Ontario, London, ON, 2018.

[12] M. Momeni, Gamma-Radiation Induced Corrosion of Alloy 800, The University of Western Ontario, London, ON, 2017.

[13] R.M. Cornell, U. Schwertmann, The Iron Oxides Structure: Properties, Reactions, Occurrences and Uses, 2nd ed., Weinheim, New York, 2003.

[14] T.I. Sutherland, C.J. Sparks, J.M. Joseph, Z. Wang, G. Whitaker, T.K. Sham, J.C. Wren, Phys. Chem. Chem. Phys., 19 (2017) 695–708.

[15] L. Wu, D. Guo, M. Li, J.M. Joseph, J.J. Noël, P.G. Keech, J.C. Wren, J. Electrochem. Soc., 164 (2017) C539–C553.

Chapter 7. Effect of Surface Area Ratio on the Corrosion Dynamics of Galvanically Coupled Carbon Steel and Stainless Steel in Different Solution Environments

7.1 Introduction

Many uncertainties about the solution environments in the annular air gap exist because access to the weld zone is limited. For instance, the pH, temperature and redox properties of the solution could vary, and the effects of these factors were investigated in detail in Chapters 4, 5 and 6. What has not yet been considered is that the solution volume at the local weld region could vary, which would result in different surface area coverages of the CS and the filler material SS. Many researchers have investigated the effect of cathode to anode (cathode:anode) surface area ratio in galvanic corrosion studies and a linear increase in coupling current (I_{cpl}) with increasing cathode:anode area ratio was often observed [1–8]. As discussed in Chapter 2, this linear relationship exists only under certain ideal conditions such as: the rates of both metals in a galvanic couple following the Tafel equation and the solution reduction reaction (typically oxygen reduction reaction (ORR)) being under diffusion control. However, our previous studies, including the ones presented in Chapter 4 and 5, have found that the corrosion of CS evolves through different dynamic stages as a result of the coupling between elementary steps (e.g. interfacial electrochemical reactions, solution reactions, corrosion product deposition, mass transport processes) [9–11]. Therefore, as the elementary steps that predominate continue to evolve with time, a linear relationship between I_{cpl} and the cathode:anode area ratio cannot always be relied upon. Moreover, the measurement of I_{cpl} does not necessarily give corrosion rate information for the anode of interest. To address this issue, the effect of the SS:CS area ratio on the corrosion dynamics of CS galvanically coupled to SS was investigated. The evolution of the reduction currents on both CS and SS was studied. The anodic i-E relationship for a CS electrode was also obtained.

7.2 Experimental

7.2.1 Electrode and electrolyte preparation

A three-electrode cell, consisting of a reference electrode, a Pt mesh counter electrode and a metal working electrode, was used for the electrochemical studies. The working electrode was a carbon steel (CS, SA36)-stainless steel (SS, Type 309) couple which was not physically welded together but electrically connected using a potentiostat. A saturated calomel electrode (SCE) (Fisher Scientific) was used for experiments carried out at 21 °C and 50 °C, whereas an Ag/AgCl electrode was employed for experiments conducted at 80 °C due to its stability at elevated temperatures. An Hg/HgO reference electrode was used for tests performed in the presence of radiation. The electrochemical cell was heated by the circulation of heat-controlled water through the dual-walled cell body.

Prior to each test, the coupon was abraded successively with 1200 and 2500 grit SiC paper followed by polishing on a Texmet microcloth (Buehler) with a 1 μm MetaDi Supreme diamond paste suspension (Buehler) to reach a mirror-like surface. The exposed surface areas of each CS and SS working electrode were limited to 0.455 cm^2 and 1.267 cm^2 respectively by covering the surrounding areas with Teflon or Parafilm (when radiation was present). The effect of the SS:CS area ratio on galvanic corrosion was investigated by coupling one CS electrode to various numbers of SS electrode (1 to 3), which are denoted CS-SS, CS-2SS and CS-3SS, respectively in this chapter. All exposed surfaces of coupons were immersed in 0.01 M Borate buffer solutions exposed to air, made using reagent grade $Na_2B_4O_7 \cdot 10H_2O$ (EMD Millipore Corporation). The solution pH was adjusted to 6.0 by adding reagent grade H_3BO_3 (Caledon Laboratories Ltd.) to the borate solutions. Solutions were prepared with purified water made using a NANOpure Diamond UV ultra-pure water system (Barnstead International) to give a resistivity of 18.2 MΩ·cm.

7.2.2 Coupling potential and coupling current measurements

The coupling potential (E_{cpl}) and coupling current (I_{cpl}) of the CS-SS couple in a given environment were simultaneously measured using two channels of a potentiostat. The details of this set-up are the same as described in Chapter 5. For the cases where CS was coupled to more than one SS electrode, all SS electrodes were electrically connected using copper wires. Due to the complexity of using two channels under irradiated conditions, the measurements of E_{cpl} and I_{cpl} were carried out in two separate electrochemical cells.

7.2.3 Dual-electrochemical cell measurement

The simplified dual-electrochemical cell (DEC) set-up described in Chapter 6 was used for the corrosion current measurements in this study. Generally, the corrosion currents were continuously measured while the CS working electrode in an electrochemical cell purged with Ar was polarized to previously recorded E_{cpl} values. This was performed by directly applying the electrode potential with a step function used as an approximation of the E_{cpl} profiles.

7.2.4 Cyclic voltammetry measurement

The cyclic voltammetry (CV) tests in this study were performed in Ar-purged solutions and were preceded by 5-min cathodic cleaning at −1.1 V_{SCE}. For each set of solution conditions studied, two potential scan ranges were used: the lower scan limit was always −1.1 V_{SCE} while the upper scan limit was −0.4 V_{SCE} or 0.0 V_{SCE}. Each of the two ranges were cycled through five times with a scan rate of 1 mV/s. For the CV test results presented in this chapter the electrode potential was corrected for solution resistance (R_{s}) using $E = E_{\mathrm{appl}} - iR_{\mathrm{s}}$. E_{appl} represents the applied potential. R_{s} was determined prior to each CV scan using the impedance method at 1 kHz. The value of R_{s} was about 180~400 Ω, depending on the temperature.

7.2.5 Irradiation tests

Irradiation tests were carried out in a ^{60}Co gamma cell. The electrochemical cells were placed in a loading chamber which descends into the irradiation chamber via a vertical lift. A digital timer is programmed to terminate the radiation exposure by returning the loading chamber to its raised position after the set time-point has been reached. Over the timeframe of the experiments documented in this paper, the dose rate was 2.8 kGy/h (1 Gy = 1 J/kg).

7.3 Results and discussion

7.3.1 Galvanic corrosion of CS-SS: Effect of temperature

The E_{cpl} and i_{cpl} (normalized to the surface area of CS) of the galvanically coupled CS-SS were measured for 72 h at three different temperatures, and the results are presented in Figure 7.1. Also in the figure are the corrosion currents for CS coupled to SS ($i_{\mathrm{corr-CS\ cpl}}$) measured using the DEC method.

At both 21 °C and 50 °C, E_{cpl} and i_{cpl} increase with increasing SS:CS area ratio and the E_{cpl} values are in the range −0.55±0.1 $\mathrm{V_{SCE}}$. At 21 °C, the time-dependent behaviors of E_{cpl}, i_{cpl} and $i_{\mathrm{corr-CS\ cpl}}$ for CS-SS and CS-2SS are similar, as they both decrease slowly with time and eventually reach a steady-state value. The E_{cpl} for CS-2SS is about 35 mV higher than for CS-SS over 72 h. The i_{cpl} for CS-2SS is higher than for CS-SS, within a factor of 3. The $i_{\mathrm{corr-CS\ cpl}}$ for the CS-2SS couple is also higher than for the CS-SS couple, however, by a factor of less than 2 over 72 h. The E_{cpl} value of the CS-3SS further increases by 35 mV initially, then gradually increases over 20 h and reaches a steady-state value of −0.52 $\mathrm{V_{SCE}}$, at which it stays for the remainder of the test duration. Although the E_{cpl} value of CS-3SS after 20 h can be considered to be constant, some oscillations with small amplitude can still be observed. The time-dependence of the $i_{\mathrm{corr-CS\ cpl}}$ of CS-3SS closely follows the time-dependence of its E_{cpl} and they oscillate in phase. The $i_{\mathrm{corr-CS\ cpl}}$ for CS-3SS is initially 1.5 times as high as that of CS-2SS, but then increases to 2.5 times as high. The i_{cpl} and E_{cpl} of CS-3SS also oscillate in phase. However, the overall time-dependence of i_{cpl} does not follow that of E_{cpl} as the i_{cpl} remains stable at a value of 0.1 mA/cm^2 over the first 40 h and increases slightly with time at later times.

The i_{cpl} of CS-3SS is also higher than that of CS-2SS, by a factor of 2 initially, which increases to 3 at later times.

At 50 °C, the change in E_{cpl} with increasing surface area of SS is also reflected in the change in i_{cpl} and $i_{\mathrm{corr-CS\ cpl}}$, as they both increase with increasing SS:CS area ratio. This is similar to our observations at 21 °C. The initial E_{cpl} values for the CS-SS couple with varying surface area of SS (CS-SS/2SS/3SS) at 50 °C are the same as at 21 °C, but at 50 °C they all decrease with time initially and then increase at later times. This decrease in E_{cpl} is also observed at 21 °C but occurs more rapidly at 50 °C. Upon reaching the minimum value (lower than the minimum E_{cpl} obtained at 21 °C), it increases at a nearly linear rate which continues for the rest of the test duration. The time for E_{cpl} to reach this minimum value is lower for higher values of the SS:CS area ratio. The E_{cpl} values over 72 h at both 21 °C and 50 °C are in between E_{eq}($Fe(OH)_2 \rightleftharpoons Fe_3O_4$) and E_{eq}($Fe(OH)_2 \rightleftharpoons \gamma$-FeOOH). The lower E_{cpl} for the CS-SS/2SS/3SS couple over the first 40 h at 50 °C than that at 21 °C indicates a lower overpotential for the corresponding redox reactions of $Fe(OH)_2 \rightleftharpoons Fe_3O_4$, and thus lower oxidation currents are expected at 50 °C. However, this is opposite to the measured DEC results which show that $i_{\mathrm{corr-CS\ cpl}}$ is higher at 50 °C than at 21 °C. The lower E_{cpl} values but higher oxidation currents obtained at 50 °C are likely due to a higher exchange current density (i_{ox}^{0}) at a higher temperature and a higher transport rate of metal cations from the metal surface to the bulk solution [12].

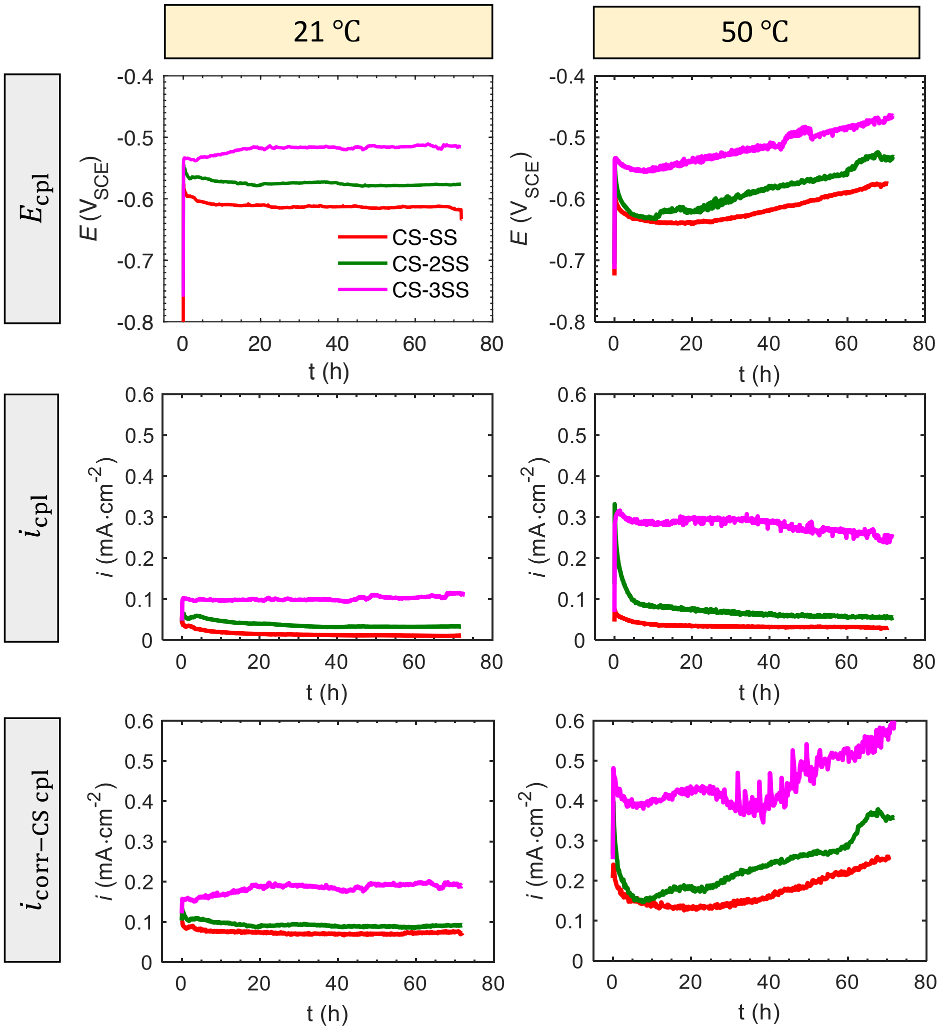

Figure 7.1 Evolution of E_{cpl}, i_{cpl} and $i_{\text{corr-CS cpl}}$ with time during galvanic corrosion of a CS-SS couple with varying SS surface area at 21 °C and 50 °C.

The E_{cpl} value for CS-2SS is slightly higher than for CS-SS in the first 10 h at 50 °C. This difference then increases to 40 mV as time progresses. This is opposite to the time-dependent behavior of i_{cpl} in which the difference between the i_{cpl} values of CS-SS and CS-2SS decreases with time. The time-dependence of the $i_{\text{corr-CS cpl}}$ for CS-SS/2SS again closely follows the time-dependence of their E_{cpl} at 50 °C. The E_{cpl} value for CS-3SS is about 75±5 mV higher than for CS-2SS. However, the time-dependence of i_{cpl} and $i_{\mathrm{corr-CS\ cpl}}$ of CS-3SS does not always follow that of the corresponding E_{cpl}. Instead, i_{cpl} decreases slowly while $i_{\mathrm{corr-CS\ cpl}}$ oscillates with time, as the E_{cpl} continues to increase with time after 20 h.

The initial E_{cpl} values for the CS-SS/2SS/3SS couple in the first few hours at 80 °C (Figure 7.2) are also lower than those obtained at 21 °C. The lower E_{cpl} is accompanied by a higher $i_{\mathrm{corr-CS\ cpl}}$, similar to the observations at 50 °C. This is also due to a higher i_{ox}^{0} at 80 °C. The rates of metal oxidation, mass transport and oxide formation are higher at 80 °C than at 50 °C, hence corrosion progression is faster at 80 °C and it takes less time for E_{cpl} at 80 °C than at 50 °C to increase to a value higher than E_{cpl} at 21 °C.

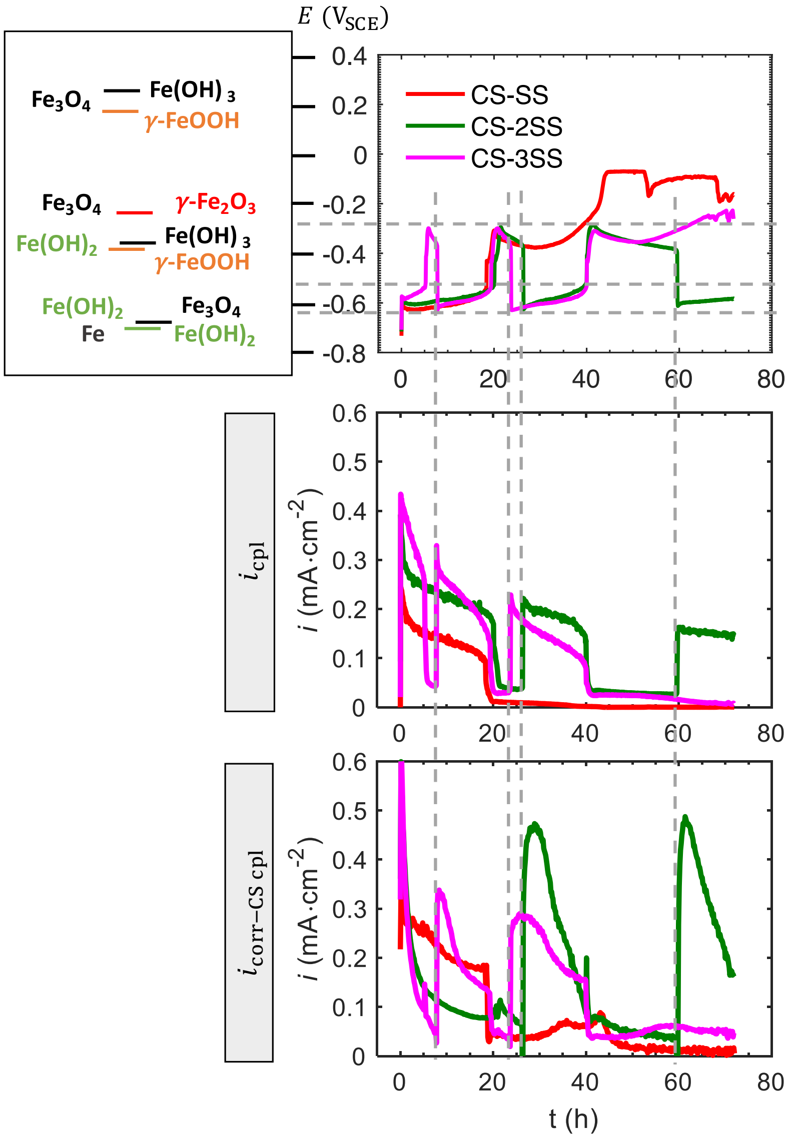

Figure 7.2 Evolution of E_{cpl}, i_{cpl} and $i_{\mathrm{corr-CS\ cpl}}$ with time during galvanic corrosion of a CS-SS couple at 80 °C, with the equilibrium potentials diagram on the left.

At 80 °C, the E_{cpl} values of the CS-SS/2SS/3SS couple oscillate with time. The frequency of such oscillation behaviour increases with increasing SS:CS area ratio, indicating faster corrosion progression for CS coupled to SS with a larger surface area. At first glance the temporal profile of E_{cpl} looks chaotic and erratic. However, some key features can still be discerned.

The minimum and maximum E_{cpl} values of the oscillation are about −0.65 V_{SCE} and −0.3 V_{SCE}, corresponding to E_{eq}($Fe(OH)_2 \rightleftharpoons Fe_3O_4$) and E_{eq}($Fe(OH)_2 \rightleftharpoons Fe(OH)_3$), respectively. Before reaching the maximum E_{cpl} after departing from the minimum value, an intermediate region (−0.65 V_{SCE} ~ −0.55 V_{SCE}) exists. The gradual increase in E_{cpl} and decrease in i_{cpl} in this region is also observed for the CS-SS couple and is assigned as the accumulation of $Fe(OH)_2$ and Fe_3O_4 on the CS surface, as discussed in Chapter 5.

After enough $Fe(OH)_2$ has accumulated on the CS surface, a fast transition from the intermediate E_{cpl} of −0.55 V_{SCE} to the maximum E_{cpl} (−0.3 V_{SCE}) occurs. This could be explained by the fast thermal reaction of $Fe(OH)_2$ to Fe_3O_4 [13,14]. The Fe_3O_4 layers or the mixed $Fe(OH)_2$ and Fe_3O_4 oxides formed on the surface act as a potential barrier for charge transfer, slowing down further metal oxidation. To meet the law of charge balance, the total reduction current on the galvanic couple decreases with time during this stage, resulting in the increase in E_{cpl}. This hypothesis is supported by the decrease in i_{cpl} and $i_{\mathrm{corr-CS\ cpl}}$ shown in Figure 7.2. The conversion of $Fe(OH)_2$ to γ-FeOOH/$Fe(OH)_3$ could also contribute to the increase in E_{cpl} at later times when E_{cpl} is higher than E_{eq}($Fe(OH)_2 \rightleftharpoons$ γ-FeOOH) or E_{eq}($Fe(OH)_2 \rightleftharpoons Fe(OH)_3$).

A gradual decrease in E_{cpl} after reaching the maximum value is also observed for the CS-2SS/3SS couple (unlike for the CS-SS couple), but it occurs at a much earlier time for the CS-3SS couple than for the CS-SS/2SS couple. As discussed in Chapter 5, this gradual decrease in E_{cpl}, i_{cpl} and $i_{\mathrm{corr-CS\ cpl}}$ is assigned as the reduction of $Fe(OH)_3$ to

$Fe(OH)_2$. Instead of increasing again after this gradual decrease, as observed for the CS-SS couple, the E_{cpl} of the CS-2SS/3SS continues to decrease with time. This decrease occurs very rapidly, similar to the fast transition stage ($Fe(OH)_2 \rightleftharpoons Fe_3O_4$) described earlier. However, this decrease is not likely due to the reverse reaction of $Fe(OH)_2 \rightleftharpoons Fe_3O_4$, since Fe_3O_4 is a more stable corrosion product and the value of E_{cpl} is still above $E_{\mathrm{eq}}(Fe(OH)_2 \rightleftharpoons Fe_3O_4)$. Therefore, the reduction of Fe_3O_4 to $Fe(OH)_2$ can be excluded in this potential region.

Oscillation in electrode potential was also observed on CS during its independent corrosion at pH 7.5 and 21 °C [10]. This oscillation is attributed to the solution redox reaction $Fe(OH)_2 \leftrightarrows Fe(OH)_3$ since the E_{corr} value oscillates between $E_{\mathrm{eq}}(Fe^0 \leftrightarrows Fe(OH)_2)$ and $E_{\mathrm{eq}}(Fe(OH)_2 \leftrightarrows Fe(OH)_3)$. At pH 7.5, the measured E_{corr} and i_{corr} oscillate in phase and they both increase or decrease at the same time. However, this is the inverse of what occurs at pH 6.0 and 80 °C. Although the measured E_{cpl} and $i_{\mathrm{corr-CS\ cpl}}$ oscillate in phase, their time-dependence is inverted. During the experiments, we observed some orange oxide particles falling off the electrode surface and collecting at the bottom of the electrochemical cell. The rapid decrease in E_{cpl} and increase in i_{cpl} and $i_{\mathrm{corr-CS\ cpl}}$ could be associated with the formation and subsequent loss from the surface of these oxide particles. The orange oxide particles are γ-FeOOH, which were formed via chemical reactions, so the layer of γ-FeOOH is unlikely to be firmly attached to the surface of the CS electrode. While these particles accumulate on the surface they could also fall off into solution. Subsequently, the sites which were originally covered by the oxides become more active, resulting in higher oxidation current on the CS and hence higher reduction current on the CS-SS couple. As a result, a lower E_{cpl} value is achieved. As corrosion continues, the active sites are again covered by oxides, resulting in the higher E_{cpl} and lower i_{cpl} and $i_{\mathrm{corr-CS\ cpl}}$ we measured at later times.

In summary, increasing SS:CS surface area and/or increasing temperature accelerate the progression of corrosion of CS, and their effects on the oxidation rate of CS have a strong time-dependence. Initially, the oxidation rate of CS increases with increased SS:CS surface area ratio and/or increased temperature. At longer times, however, these factors lead to earlier and faster oxide formation on CS. Due to the strong coupling between each elementary step (such as metal oxidation, oxide formation/dissolution, and mass transport), oscillation behaviour can be observed, further confirming the non-linear corrosion dynamics of CS when coupled to SS. Hence, simple linear extrapolation of the corrosion rate from low temperatures to high temperatures [4] may not work.

7.3.2 Galvanic corrosion of CS-SS: Effect of γ-radiation

The effect of γ-radiation on the galvanic corrosion of CS-SS couples with varying SS:CS area ratios was investigated by monitoring the E_{cpl}, i_{cpl} and $i_{\mathrm{corr-CS\ cpl}}$ over 20 h. As shown in Figure 7.3, γ-radiation increases the E_{cpl} of the CS-SS/2SS/3SS couple, similar to our previous observations on the independent corrosion of CS and SS. As discussed earlier, the increase in E_{cpl} is due to the presence of the strong oxidants produced from water radiolysis (eg. H_2O_2, O_2) [15,16]. The amount of increase in E_{cpl} varies with the SS:CS area ratio and time.

In the presence of radiation, E_{cpl}, i_{cpl} and $i_{\mathrm{corr-CS\ cpl}}$ for the CS-SS/2SS/3SS couple are higher than in the absence of radiation (except for the i_{cpl} of CS-3SS). These values all increase with increasing SS:CS area ratio, which is similar to our observations in the absence of radiation. The amount of increase of E_{cpl} for the CS-2SS couple due to the presence of radiation is initially 20 mV, which increases to 60 mV at 20 h. In comparison, the amount of increase of E_{cpl} for the CS-3SS couple is about 35 mV, and remains relatively stable over 20 h. The time-dependence of the $i_{\mathrm{corr-CS\,cpl}}$ of CS-SS/2SS/3SS couple closely follows the time-dependence of its E_{cpl}. In the presence of radiation, the $i_{\mathrm{corr-CS\,cpl}}$ is observed higher than i_{cpl} by a factor of 2~3, again indicating the non-negligible solution reduction current on CS.

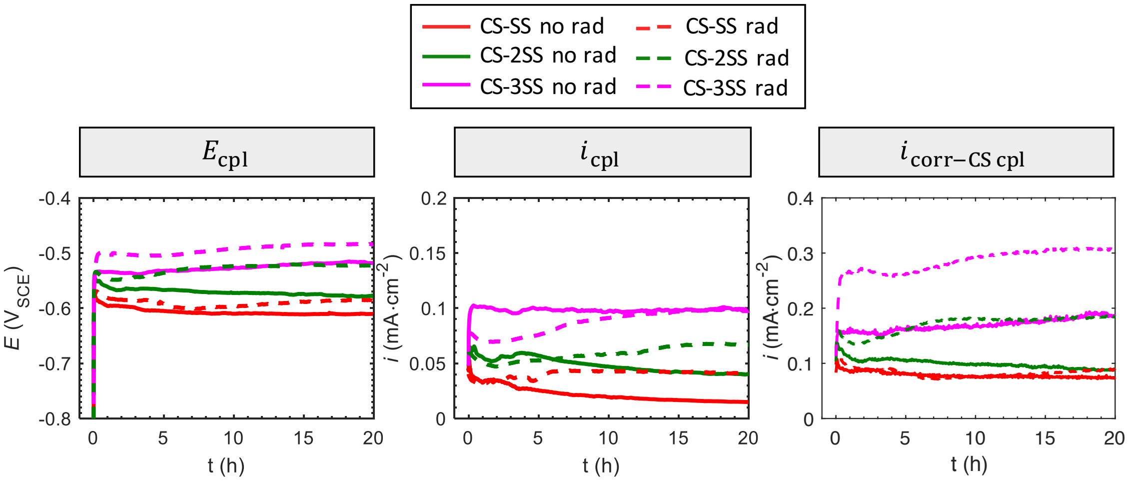

Figure 7.3 Evolution of E_{cpl}, i_{cpl} and $i_{\mathrm{corr-CS\,cpl}}$ with time during galvanic corrosion of the CS-SS couple in the presence (dashed line) and absence (solid line) of radiation at 21 °C.

7.3.3 Evolution of the reduction current

For any galvanic couple the net currents on CS and SS are equal to I_{cpl}, which can be expressed as follows:

$$I_{\mathrm{cpl}} = I_{\mathrm{ox-CS\,cpl}} - \left|I_{\mathrm{red-CS\,cpl}}\right| = \left|I_{\mathrm{red-SS\,cpl}}\right| - I_{\mathrm{ox-SS\,cpl}} \quad (7.1)$$

where $I_{\mathrm{ox-CS\,cpl}}$ is the total oxidation current on CS after coupling, $I_{\mathrm{red-CS\,cpl}}$ is the total reduction current on CS after coupling, $I_{\mathrm{red-SS\,cpl}}$ is the total reduction current on SS after coupling and $I_{\mathrm{ox-SS\,cpl}}$ is the total oxidation current on SS after coupling.

As discussed earlier in Chapter 5, $I_{\mathrm{ox-SS\,cpl}}$ at both 21 °C and 50 °C is negligible compared to $I_{\mathrm{ox-CS\,cpl}}$ or I_{cpl} after a few minutes. Therefore, the above equation can be written as:

$$I_{\mathrm{cpl}} = I_{\mathrm{ox-CS\,cpl}} - \left|I_{\mathrm{red-CS\,cpl}}\right| = \left|I_{\mathrm{red-SS\,cpl}}\right| \quad (7.2)$$

I_{cpl} can be measured directly using a zero resistance ammeter (ZRA) while $I_{\mathrm{ox-CS\,cpl}}$ can be represented by $I_{\mathrm{corr-CS\,cpl}}$, measured using the DEC method. Therefore, the reduction current density on CS after coupling ($|i_{\mathrm{red-CS\,cpl}}|$) and that on SS after coupling ($|i_{\mathrm{red-SS\,cpl}}|$) can be easily calculated.

As shown in Figure 7.4, both $|i_{\mathrm{red-CS\,cpl}}|$ and $|i_{\mathrm{red-SS\,cpl}}|$ increase when the temperature increases from 21 °C to 50 °C, by a factor of 2~3, depending on the time and the SS:CS surface area ratio. The overall time-dependence of $|i_{\mathrm{red-CS\,cpl}}|$ closely follows that of E_{cpl} whereas the time-dependence of $|i_{\mathrm{red-SS\,cpl}}|$ does not always follow that of E_{cpl}, particularly at 50 °C. At both temperatures, $|i_{\mathrm{red-CS\,cpl}}|$ is always higher than $|i_{\mathrm{red-SS\,cpl}}|$, by a factor of 5~10 depending on the time and the SS:CS surface area ratio. One possible reason for this observation is a higher ORR activity on the CS than on the SS, which has also been previously reported [17,18]. Another reason could be related to the change in surface area for the ORR on CS. As corrosion progresses, oxide formation is possible and there are always gaps or void spaces between the metal substrate and the oxide layers [10]. Other than the metal substrate, the ORR could also occur on the oxide layers as long as the oxide is conductive. Therefore, the actual area for the ORR is potentially larger than the surface area of the metal. However, the $|i_{\mathrm{red-CS\ cpl}}|$ presented in Figure 7.4 is normalized to a constant value of the surface area of CS.

As shown earlier in Figure 7.1, both E_{cpl} and $i_{\mathrm{corr-CS\ cpl}}$ measured at 21 °C and 50 °C increase with increasing SS:CS surface area ratio. However, $|i_{\mathrm{red-CS\ cpl}}|$ does not show strong dependence on the SS:CS surface area ratio, particularly for the case at 50 °C where the values of $|i_{\mathrm{red-CS\ cpl}}|$ over 72 h are very close, nearly independent of the SS:CS surface area ratio. However, the values of $|i_{\mathrm{red-CS\ cpl}}|$ are generally higher than the reduction current on the independently corroded CS ($|i_{\mathrm{red-CS\ ind}}|$).

The $|i_{\mathrm{red-SS\ cpl}}|$ for the CS-2SS couple is slightly higher than for the CS-SS couple at 21 °C, but they almost coincide at 50 °C. The near constant $|i_{\mathrm{red-SS\ cpl}}|$ or linearly increasing I_{cpl} with increasing SS:CS surface area ratio is observed in many galvanic corrosion studies. This is often interpreted as the rate of the anodic reactions being under cathodic control (i.e., the corrosion rate of CS is limited by the rate at which O_2 can be reduced on CS), as the increasing surface area of the cathode can provide more sites for the O_2 reduction reaction [8,18,19]. However, when the SS:CS area ratio further increases, the $|i_{\mathrm{red-SS\ cpl}}|$ for the CS-3SS couple at both temperatures is higher than that of the CS-2SS couple, by a factor of 2~4. The above observations confirm that the assumption of near constant $|i_{\mathrm{red-SS\ cpl}}|$ or linearly increasing I_{cpl} with increasing SS:CS surface area ratio is not always valid. The increasing $|i_{\mathrm{red-CS\ cpl}}|$ and $|i_{\mathrm{red-SS\ cpl}}|$ with increasing E_{cpl} or SS:CS surface area ratio can be attributed to additional reduction reactions, e.g., the reduction of

Fe^{III} corrosion products, which is also observed with the rust layers of iron during its atmospheric corrosion [20].

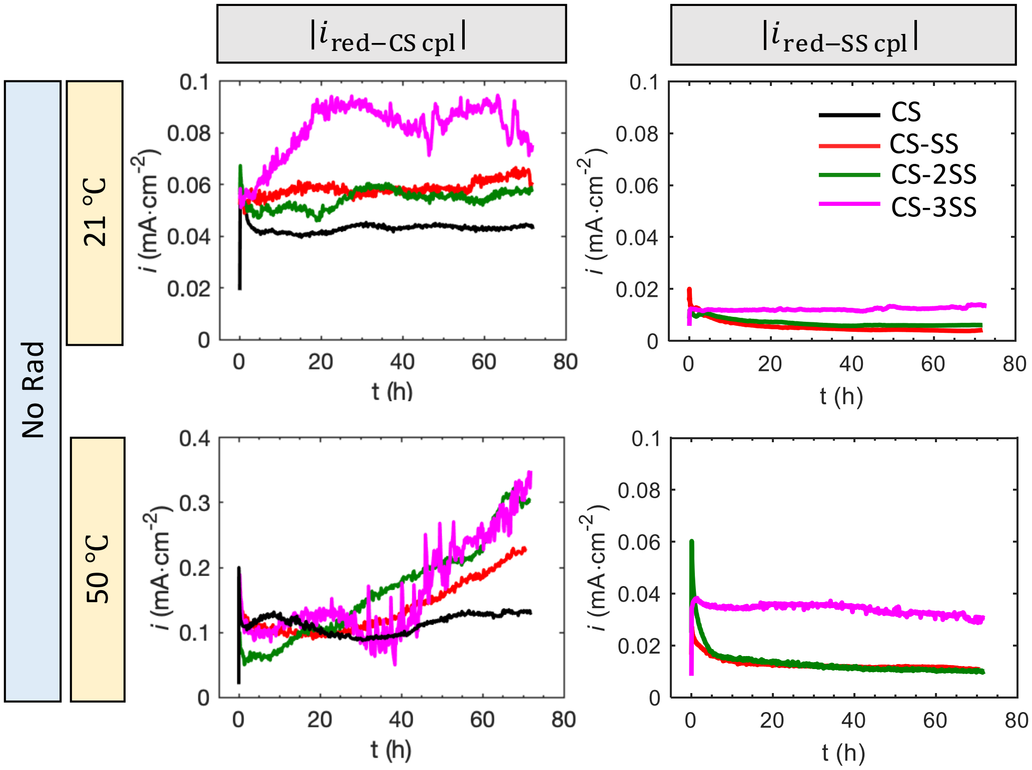

Figure 7.4 The reduction current density on independently corroded CS ($|i_{\text{red-CS cpl}}|$) and SS ($|i_{\text{red-SS cpl}}|$) in the absence of radiation.

The reduction current density results for the irradiated cases are presented in Figure 7.5. In the presence of radiation, the values of $|i_{\text{red-CS cpl}}|$ are again observed to be much higher than the $|i_{\text{red-SS cpl}}|$ for all CS-SS/2SS/3SS couples, indicating a higher reduction reaction activity on CS than on SS. The $|i_{\text{red-CS cpl}}|$ of CS-SS in the presence of radiation does not vary as much as in the absence of radiation, and it remains close to $|i_{\text{red-CS ind}}|$.

However, the $|i_{\mathrm{red-CS\ cpl}}|$ of the CS-2SS/3SS couples increases by a factor of 2~4 when exposed to radiation. In comparison, $|i_{\mathrm{red-SS\ cpl}}|$ does not show any clear dependence on the SS:CS area ratio in the presence of radiation and the values are all within a factor of 2. When exposed to a continuous flux of radiation, the oxidants (O_2, H_2O_2) are homogeneously distributed in the solution, and are constantly replenished via water radiolysis [15,21]. Therefore, the oxidation rate of CS in the presence of radiation is unlikely to be limited by solution reduction reactions. Even though the value of $|i_{\mathrm{red-SS\ cpl}}|$ with various SS:CS area ratio is nearly constant, this does not necessarily indicate that the CS corrosion rate is under cathodic control. In the presence of radiation, the values of $|i_{\mathrm{red-CS\ cpl}}|$ and $|i_{\mathrm{red-SS\ cpl}}|$ are generally higher. This could also be attributed to additional reduction reactions (reduction of Fe^{III} and/or H_2O_2) on the surfaces of CS and SS.

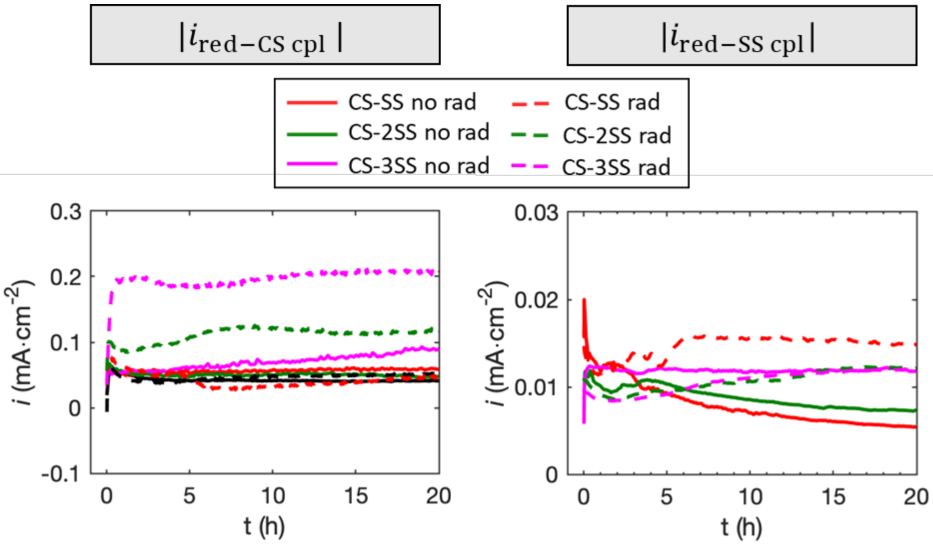

Figure 7.5 Comparison between $|i_{\mathrm{red-CS\ cpl}}|$ and $|i_{\mathrm{red-SS\ cpl}}|$ in the presence (dashed line) and absence of radiation (solid line) at 21 °C.

7.3.4 Cyclic voltammetry of CS in Ar-purged solutions

CV was performed to identify the electrochemical reactions that could be occurring on a CS electrode in Ar-purged pH 6.0 solution. As mentioned in the experimental section, two different upper scan limits were used in this study: −0.4 V_{SCE} and 0.0 V_{SCE}. These upper vertex potentials (E_{upp}) were chosen as they represent the upper limits of the E_{cpl} values observed in aerated pH 6.0 solutions (shown in Figure 7.1 and Figure 7.2). Figure 7.6 shows the first cycle CVs obtained for CS electrodes at varying temperatures. Two types of plots are presented in the figure: i versus E and E versus log $|i|$. Also shown in these figures is the E_{corr} value (Ar-E_{corr}) of CS observed in the same solution environment, which remains stable at −0.70 V_{SCE} throughout the 40-h test duration [10]. The E_{eq} values of different redox reactions of iron species are provided for comparison.

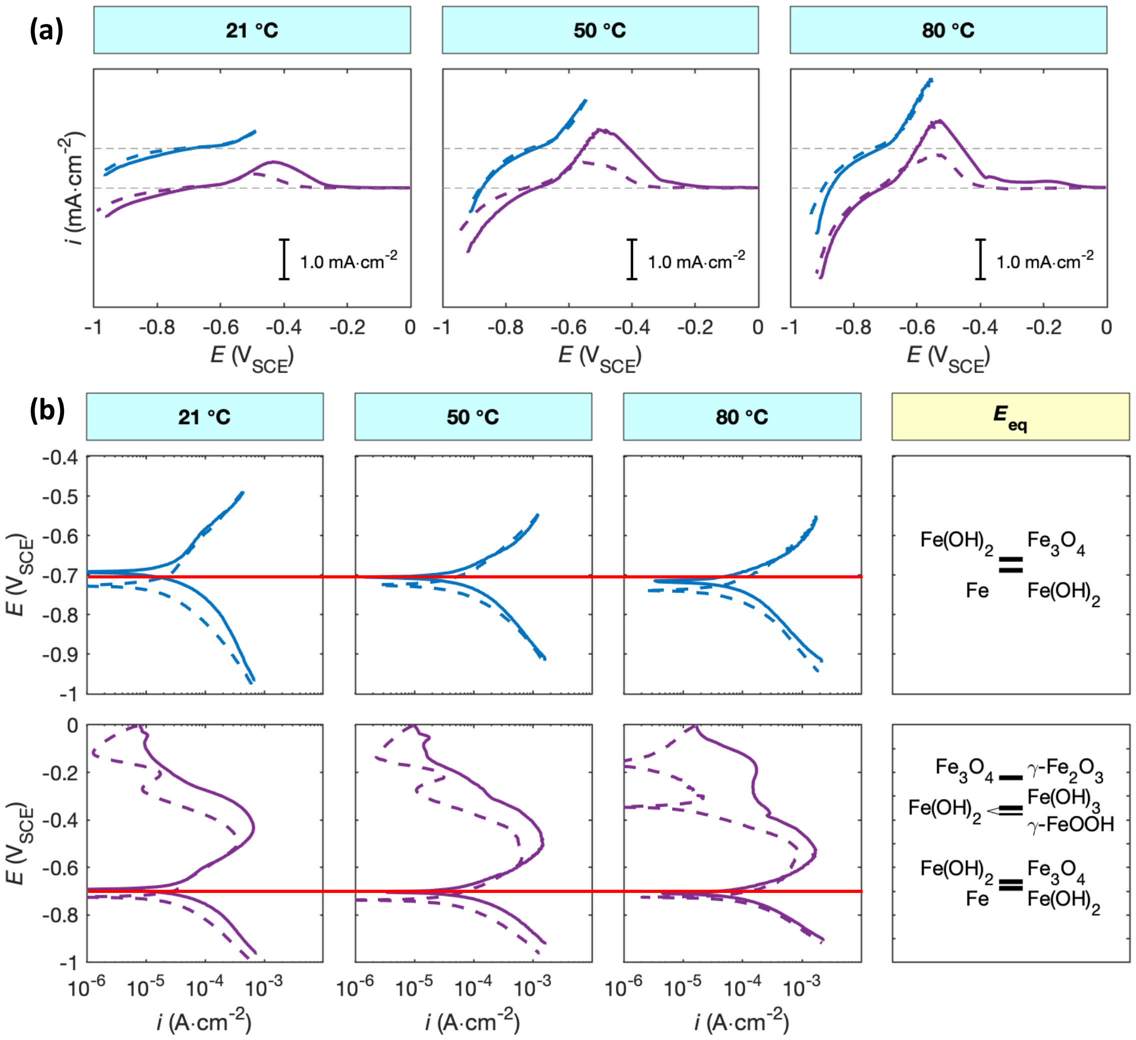

Figure 7.6 The first CV cycle for CS in Ar-purged pH 6.0 borate solutions: (a) plot of i versus E; (b) plot of E versus log $|i|$ with Ar-E_{corr} (red lines) and the E_{eq} values of different redox reactions of iron species; solid lines represent forward scans and dashed lines represent reverse scans.

The forward scans of the first CV cycle for CS with two different upper limits are presented in Figure 7.7. The results show very good reproducibility; at a given temperature the difference in the CV during forward scans obtained with two different upper limits is negligible. The electrode potential at which the polarization current is zero ($E_{i=0}$) is close to $E_{\mathrm{eq}}(\mathrm{Fe}^0 \rightleftharpoons \mathrm{Fe(OH)_2})$ and it almost coincides with the Ar-E_{corr} value.

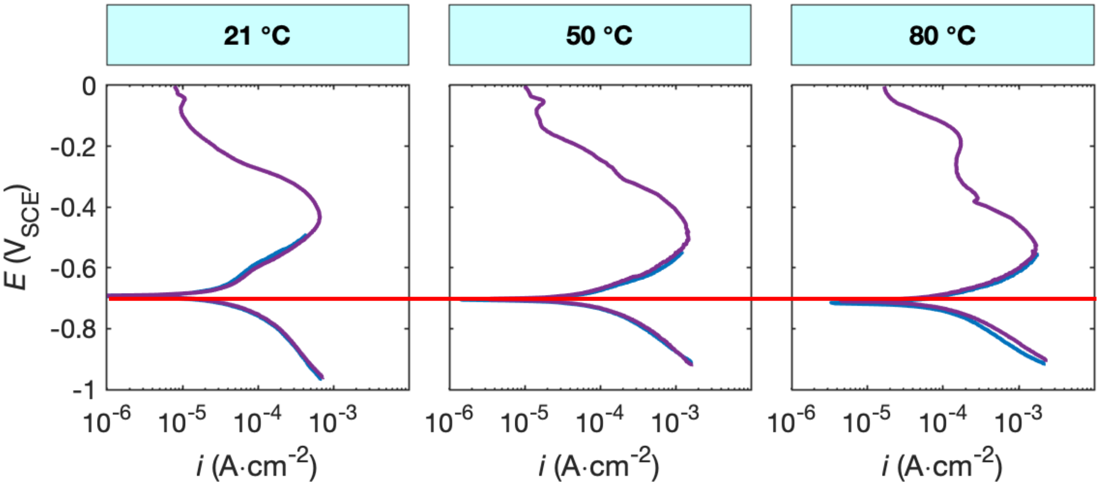

Figure 7.7 Forward scans of the first CV cycle for CS with two different upper limits in Ar-purged pH 6.0 borate solutions. The red line indicates the Ar-E_{corr}.

During the forward scan from −1.1 $\mathrm{V_{SCE}}$, the cathodic current decreases exponentially with E_{appl} in a potential range lower than −0.8 $\mathrm{V_{SCE}}$. The average cathodic Tafel slopes (b_{c}) at 21 °C, 50 °C and 80 °C obtained in this potential range from the E versus log $|i|$ plots are 294, 200 and 154 mV/dec, respectively (Table 7.1). In Ar-purged solutions the hydrogen evolution reaction (HER) is the only solution reduction reaction occurring and the ORR is negligible. The HER is a 2-electron process, the ideal Tafel slope for which should be 60 mV/dec. However, it is generally considered as comprising three elementary steps: the Volmer reaction (1-electron process), the Heyrovsky reaction (1-electron process) and the Tafel reaction (non-electrochemical) [22]. The Tafel slope for HER would be 120 mV/dec if the Volmer reaction was the rate-determining step (RDS)

[22]. Previous potentiostatic polarization studies on CS corrosion at neutral pHs found that the oxidation rate of CS ($Fe^0 \rightleftharpoons Fe^{2+}{}_{(aq)}$) can be very large even when E_{appl} is far below the steady-state E_{corr}. Therefore, the large b_{c} obtained in this study could be due to the contribution of metal oxidation current to the cathodic region. That is, the cathodic region we usually define does not necessarily involve only HER, but could also involve metal oxidation current, resulting in the non-typical b_{c} values.

Table 7.1 Summary of parameters obtained in the forward scan of the first CV cycle for CS in Ar-purged pH 6.0 solutions.

Temperature		21 °C	50 °C	80 °C
b_{c} (mV/dec)	$E_{\text{upp}} = -0.4\ \text{V}_{\text{SCE}}$	300	182	149
	$E_{\text{upp}} = 0.0\ \text{V}_{\text{SCE}}$	288	217	158
Average b_{c} (mV/dec)		294	200	154
R_{p} ($\Omega \cdot \text{cm}^2$)		233	91	75

As the E_{appl} moves to a more positive value than $E_{i=0}$, the anodic polarization current increases exponentially over a narrow potential range depending on the temperature (< 60 mV). This is followed by a region of linear increase over a potential range of ~100 mV. This linear region can be better appreciated from the i versus E plots shown in Figure 7.6 (a). The initially exponential and later linear i-E relationship were also observed for CS corroded at higher pHs [10]. The reciprocal of the slope of this linear region, also known as the polarization resistance (R_{p}), was calculated and summarized in Table 7.1. As temperature increases, the value of R_{p} decreases, which is consistent with the LPR results presented in Chapter 4. The potential range of the linear i-E region is slightly shifted to a lower value when the temperature increases.

Increasing E_{appl} to values beyond (more positive than) the linear region causes the current to increase again, reaching a maximum (i_{max1}), before it starts to decrease with E_{appl} (for the case where E_{upp} is 0.0 V_{SCE} shown in Figure 7.6 (b)). The i_{max1} increases and occurs at a lower potential ($E_{i=i_{\mathrm{max1}}}$) when temperature increases. A similar peak is also observed on the reverse scan, but with lower current density (i'_{max1}). The potential at which i'_{max1} is reached ($E_{i=i'_{\mathrm{max1}}}$) shifts to a more negative value than $E_{i=i_{\mathrm{max1}}}$, particularly at a lower temperature. However, both $E_{i=i_{\mathrm{max1}}}$ and $E_{i=i'_{\mathrm{max1}}}$ are in between $E_{\mathrm{eq}}(\mathrm{Fe(OH)_2} \rightleftharpoons \mathrm{Fe_3O_4})$ and $E_{\mathrm{eq}}(\mathrm{Fe(OH)_2} \rightleftharpoons \gamma\text{-}\mathrm{FeOOH})$. The second peak ($i_{\mathrm{max2}}$) in the forward scan is observed at potentials higher than −0.2 V_{SCE} and is close to $E_{\mathrm{eq}}(\mathrm{Fe_3O_4} \rightleftharpoons \gamma\text{-}\mathrm{Fe_2O_3})$. This peak is much broader and occurs at a much lower potential ($E_{i=i_{\mathrm{max2}}}$) with higher temperatures. It is also observed on the reverse scan but with lower current density (i'_{max2}). At the potential region where $E_{\mathrm{appl}} > E_{i=i_{\mathrm{max2}}}$, the measured anodic currents should represent the total metal oxidation current, since HER is negligible. The lower anodic current measured in the reverse scan than in the forward scan indicates that changes in the CS surface are significantly influencing its metal oxidation rate. When the CS electrode is polarized to a high potential (e.g. 0.0 V_{SCE}) where the formation of insoluble ferric oxide (γ-$\mathrm{Fe_2O_3}$) can occur, its subsequent metal oxidation rate will be reduced, even at the same E_{appl}.

As shown in Figure 7.8, $E_{i=i_{\mathrm{max1}}}$, $E_{i=i'_{\mathrm{max1}}}$, $E_{i=i_{\mathrm{max2}}}$ and $E_{i=i'_{\mathrm{max2}}}$ all coincide with the characteristic E_{cpl} observed at 80 °C. This further indicates that the characteristic E_{cpl}

values observed at 80 °C are not the result of random variation. Instead, they are a good indication of the dominant redox reactions on the electrode surface. It should be noted that the corresponding polarization currents at these peak potentials in the forward CV scan are always higher than those measured by the DEC method (Figure 7.2). This can also be explained by the different surface conditions for CS (e.g. thickness of different oxides) between the CV scans and the DEC measurement. The CVs after the first cycle are the same shape with similar current density and therefore not shown here.

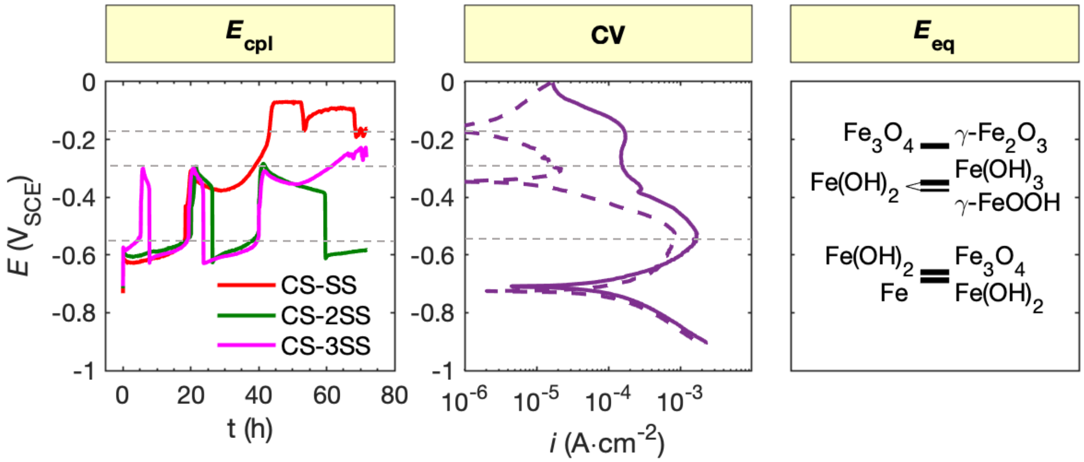

Figure 7.8 Comparison between the E_{cpl} obtained in aerated solutions and the first CV cycle in Ar-purged solution at 80 °C.

7.3.5 Anodic i-E relationship for CS in aerated solutions

The anodic i-E relationships for CS electrodes coupled to different SS surface areas using the DEC method are presented in Figure 7.9. Earlier we showed that the values of E_{corr}, E_{cpl} and the corresponding i_{corr} values for CS are generally higher in the presence of radiation than in its absence; however, the E-log i curves observed in both cases are almost the same, with an anodic Tafel slope (b_a) of ~160 mV/dec. The shapes of the E-log i curves at 50 °C are also similar to that at 21 °C (except for the region where $E < -0.65$ V_{SCE}) but the i values are shifted to more positive values at 50 °C. The value of b_a at 50 °C is also close to 160 mV/dec. Theoretically, a Tafel slope of 120 mV/dec should be observed if the RDS is a 1-electron process [12]. The b_a of ~160 mV/dec observed at both temperatures indicates that the metal oxidation is partially under mass transport control. When the concentration of the metal cations near the CS surface has reached saturation, further metal oxidation will depend on how fast the metal cations can diffuse from the surface to the bulk solution. Hence, further metal oxidation can no longer increase exponentially with increasing electrode potential, resulting in the non-typical Tafel slope we observe.

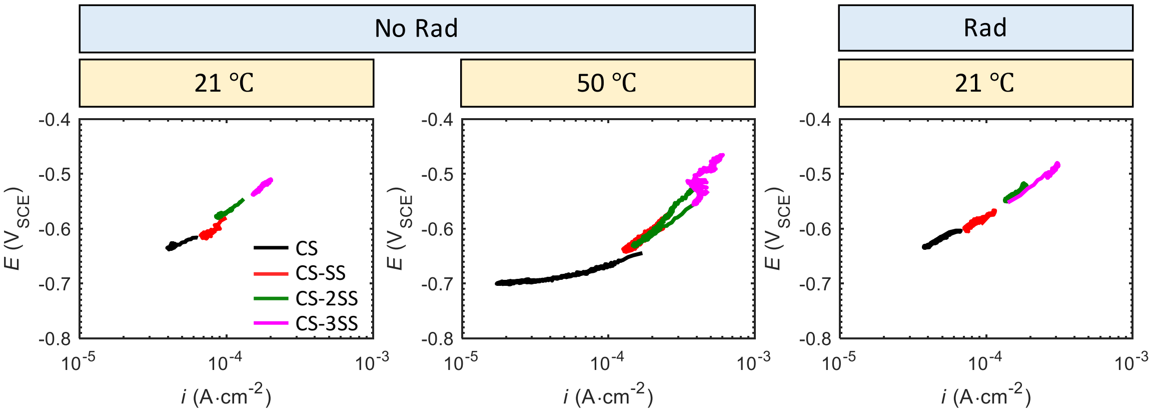

Figure 7.9 The i-E relationships for the anodic reactions for CS galvanically coupled to SS, based on the DEC measurements.

Figure 7.10 compares the i-E curves obtained by the DEC experiment and the first CV cycle with an upper scan limit of –0.4 V_{SCE}. The DEC results correlate well with the

CV cycle in the potential region close to $E_{i=0}$ at 50 °C. At higher potentials, however, the values of b_a obtained from the DEC results are much larger than those obtained from the CV curves. A relatively high scan rate was used for the CV scans (1 mV/s) so the corrosion system is not likely to reach a steady state. For the DEC measurement, however, the CS electrode potential was always maintained at its naturally corroding value (whether during its independent corrosion or galvanic corrosion). Hence the i-E relationship obtained from the DEC method is a more accurate measure of the actual CS corrosion rate.

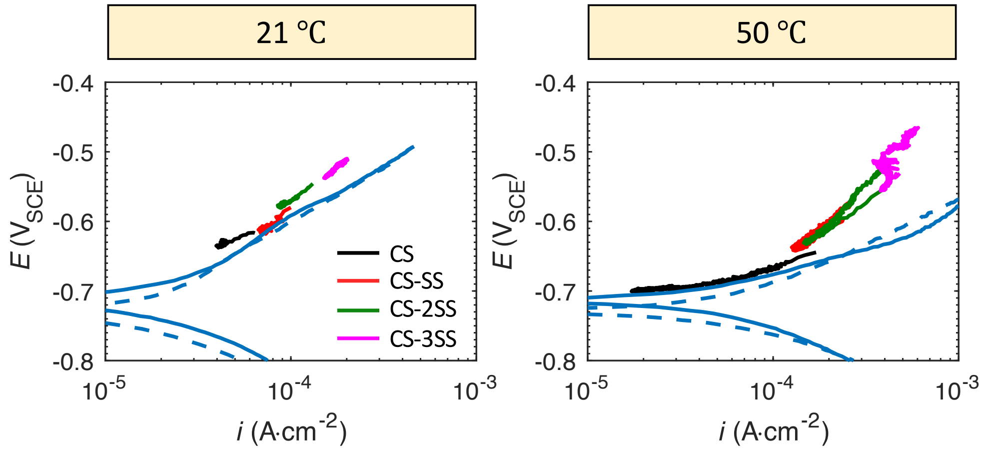

Figure 7.10 Comparison between the i-E relationship obtained using the DEC method and the first CV cycle (upper scan limit of −0.4 V_{SCE}).

Due to the mass transport component involved in the kinetics of Fe oxidation, the i-E relationships obtained using the DEC method are formulated using the Koutecky-Levich (K-L) equation [10,23,24]:

$$\frac{1}{i_{\text{ox}}} = \frac{1}{i_{\text{ox}}^{0} \exp\left(\frac{2.303\eta}{b_{\text{a}}}\right)} + \frac{1}{i_{\text{trans}}} \tag{7.3}$$

where i_{ox} is the oxidation current, for which we can use the i_{corr} measured using the DEC method, i_{ox}^{0} is the exchange current, η is the overpotential, which is defined as $(E_{\mathrm{appl}} - E_{\mathrm{eq}})$, b_{a} is the anodic Tafel slope and i_{trans} is the limiting current for the mass transport of $\mathrm{Fe^{II}}_{\mathrm{(aq)}}$. Rearranging the above equation yields:

$$i_{\mathrm{ox}} = \frac{1}{\frac{1}{i_{\mathrm{ox}}^{0}} \exp\left(-\frac{2.303\eta}{b_{\mathrm{a}}}\right) + \frac{1}{i_{\mathrm{trans}}}} \qquad (7.4)$$

The general form of this equation is $y = \frac{1}{a\,exp(-bx)+c}$ (a, b, $c > 0$), which was then used to fit the i-E data shown in Figure 7.9. In the fitting, the $E_{\mathrm{eq}}(\mathrm{Fe^0} \rightleftharpoons \mathrm{Fe(OH)_2})$ value of −0.688 $\mathrm{V_{SCE}}$ was used, assuming that all metal oxidation involves the reaction $\mathrm{Fe^0} \rightleftharpoons \mathrm{Fe(OH)_2}$. The fitted curves are presented in Figure 7.11 and the obtained values of i_{ox}^{0}, b_{a} and i_{trans} are summarized in Table 7.2.

As discussed earlier, similar E-log i curves are observed for both irradiated and non-irradiated cases. Therefore, the fitting results should also be close in both cases. At 21 °C, the fitted values of i_{ox}^{0} and b_{a} in the presence and absence of radiation are very similar. However, the values of i_{trans} in these two cases differ by a factor of 3. This difference in i_{trans} could be attributed to the uncertainties involved in curve fitting, since both E-log i curves do not show a distinct plateau corresponding to the mass-transport control region. The i_{ox}^{0} obtained for 50 °C is higher than for 21 °C, which is consistent with our earlier conclusion that higher temperatures result in higher i_{ox}^{0} values (7.3.1). The fitted parameters will be used for future model development.

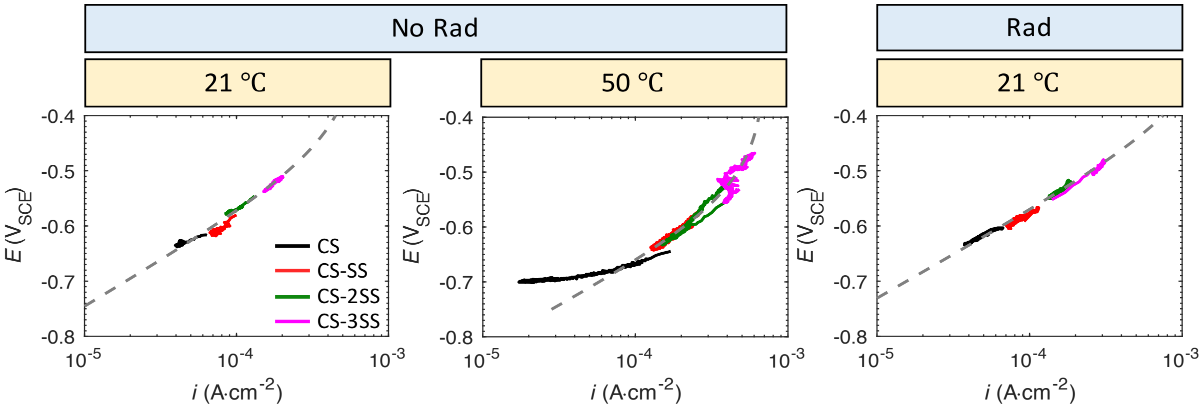

Figure 7.11 The i-E relationship of the anodic reactions for CS with the curves fitted using the Koutecky-Levich equation (dashed line).

Table 7.2 Summary of the fitted results using the Koutecky-Levich equation.

Conditions		i_{ox}^0 (A/cm^2)	b_a (mV/dec)	i_{trans} (A/cm^2)
No Rad	21 °C	2.27×10^{-5}	163	6.81×10^{-4}
	50 °C	7.56×10^{-5}	151	7.21×10^{-4}
Rad	21 °C	1.88×10^{-5}	158	1.8×10^{-3}

7.4 Conclusions

In this chapter, the effect of the SS:CS surface area ratio on the galvanic corrosion of a CS-SS couple under various solution conditions (three different temperatures and the presence and absence of radiation) was investigated. Coupling to SS accelerates the progression of the corrosion of CS. Higher SS:CS area ratios, higher temperatures or the presence of radiation further accelerate the progression of the corrosion of CS, and their effects on the oxidation rate of CS vary with time. Initially, the oxidation rate of CS is higher with a higher SS:CS surface area ratio, higher temperature or the presence of radiation. At longer times, however, the evidence indicates that these factors lead to earlier and faster oxide formation on CS, suppressing its subsequent oxidation rate.

The reduction reaction behaviours of CS and SS were also examined in this study and it was found that the relationship between I_{cpl} and the SS:CS area ratio is not always linear. Even when this relationship is linear, this does not necessarily mean the corrosion rate of CS is limited by the diffusion of O_2, because reduction reactions other than ORR could be involved in the corrosion process (e.g. $Fe^{3+} \rightarrow Fe^{2+}$). CV was also performed in deaerated solutions to study the metal oxidation in a less complicated environment. We found the anodic peaks of CV scan to coincide with the characteristic E_{cpl} obtained at 80 °C, indicating similar CS redox processes under two different sets of conditions. The CVs and the anodic i-E curves plotted based on the DEC results were compared and the DEC results were fitted using a K-L equation. The fitted parameters obtained will be used for future model development.

7.5 References

[1] F. Mansfeld, CORROSION, 27 (1971) 436–442.

[2] R. Francis, Galvanic Corrosion: A Practical Guide for Engineers, 2nd ed., NACE International, 2017.

[3] C.F. Dong, K. Xiao, X.G. Li, Y.F. Cheng, J. Mater. Eng. Perform., 20 (2011) 1631–1637.

[4] J. Soltis, K.A. Lichti, Corros. Sci., 68 (2013) 162–167.

[5] F. Mansfeld, J. V Kenkel, Corros. Sci., 15 (1975) 239–250.

[6] C.F. Dong, K. Xiao, X.G. Li, Y.F. Cheng, Wear, 270 (2010) 39–45.

[7] Z.F. Yin, M.L. Yan, Z.Q. Bai, W.Z. Zhao, W.J. Zhou, Electrochim. Acta, 53 (2008) 6285–6292.

[8] T.E. Standish, Galvanic corrosion of copper-coated carbon steel for used nuclear fuel containers, The University of Western Ontario, London, ON, 2019.

[9] L. Wu, D. Guo, M. Li, J.M. Joseph, J.J. Noël, P.G. Keech, J.C. Wren, J. Electrochem. Soc., 164 (2017) C539–C553.

[10] D. Guo, Corrosion Dynamics of Carbon Steel in Used Fuel Container Environments, The University of Western Ontario, London, ON, 2018.

[11] J.C. Wren, D. Guo, M. Li, R. Morco, J.M. Joseph, M. Behazin, P.G. Keech, Y.G. Shin, Corrosion of carbon steel inside used nuclear fuel containers, in: WM2019 Conference, Phoenix, AZ, 2019.

[12] A.J. Bard, L.R. Faulkner, Electrochemical Methods Fundamentals and Applications, 2nd ed., John Wiley & Sons, Inc., 2001.

[13] M. Booy, T.W. Swaddle, Can. J. Chem., 56 (1978) 402–403.

[14] R.O. Rihan, S. Nešić, Corros. Sci., 48 (2006) 2633–2659.

[15] J.W.T. Spinks, R.J. Woods, An Introduction to Radiation Chemistry, John Wiley & Sons, Inc., New York, 1990.

[16] K. Daub, X. Zhang, J.J. Noël, J.C. Wren, Electrochim. Acta, 55 (2010) 2767–2776.

[17] C.M. Abreu, M.J. Cristóbal, M.F. Montemor, X.R. Nóvoa, G. Pena, M.C. Pérez, Electrochim. Acta, 47 (2002) 2271–2279.

[18] S. Qian, D. Qu, G. Coates, Can. Metall. Q., 45 (2006) 475–483.

[19] S. Qian, D. Qu, J. Appl. Electrochem., 40 (2010) 247–256.

[20] M. Stratmann, K. Bohnenkamp, H.-J. Engell, Corros. Sci., 23 (1983) 969–985.

[21] J.M. Joseph, B. Seon Choi, P. Yakabuskie, J. Clara Wren, Radiat. Phys. Chem., 77 (2008) 1009–1020.

[22] T. Shinagawa, A.T. Garcia-Esparza, K. Takanabe, Sci. Rep., 5 (2015) 13801.

[23] T. Shinagawa, A.T. Garcia-Esparza, K. Takanabe, ChemElectroChem, 1 (2014) 1497–1507.

[24] U.A. Paulus, T.J. Schmidt, H.A. Gasteiger, R.J. Behm, J. Electroanal. Chem., 495 (2001) 134–145.

Chapter 8. Summary and Future Work

8.1 Summary

In this thesis, the effects of physical and chemical solution parameters on the corrosion of galvanically coupled dissimilar carbon steel-stainless steel (CS-SS) welds were investigated, with the aim of developing a corrosion dynamics model that can be used to assess the long-term integrity of CANDU nuclear reactor structural materials with confidence. The parameters studied in this thesis project were pH, temperature, the presence or absence of γ-radiation and the cathode:anode surface area ratio.

In Chapter 4, the effect of solution pH and temperature on the independent corrosion of individual CS (Type SA 36), stainless steel (SS 304) and the stainless steel filler material (SS 309) was investigated. A qualitative understanding of the individual corrosion behaviour of CS, SS 304 and SS 309 was achieved in this chapter. Generally, SS 304 and SS 309 show similar corrosion behaviours and their corrosion rates remain low at both pH 6.0 and 10.6 due to the presence of protective oxide layers on the surface. Within the test duration, the major corrosion pathway for CS at pH 6.0 is metal dissolution whereas at pH 10.6 it is oxide formation due to the much lower solubility of Fe^{II} at this pH. These results imply that that galvanic corrosion of an SS 304-SS 309 couple (under all studied conditions) and of the CS-SS 309 couple at pH 10.6, would be negligible. Therefore, the subsequent galvanic corrosion studies concentrated on the CS-SS 309 couple at pH 6.0. This chapter also introduced a dual-electrochemical cell (DEC) method for continuous measurement of corrosion rates. The corrosion rate results for CS corroded in pH 6.0 solutions using the DEC method were presented and compared with conventional electrochemical techniques such as linear polarization resistance (LPR) and potentiodynamic polarization (PD). The results demonstrated that the DEC method provides more accurate corrosion rate information than these conventional polarization techniques.

In Chapter 5, galvanic corrosion of the CS-SS (Type 309) couple was investigated in different aqueous environments (pH 6.0 combined with 21 °C, 50 °C and 80 °C). The corrosion currents of CS galvanically coupled to SS were measured using both conventional methods and the DEC method. Conventionally, the coupling current is taken to represent either the corrosion rate or the increase in the corrosion rate of the more active metal (CS in this project) in a galvanic couple. However, such correlations cannot be applied indiscriminately. In this chapter, we showed that the limitations of conventional methods can be addressed by the DEC method, which allows us to measure the corrosion rates directly and more accurately for both independent corrosion and galvanic corrosion systems. The DEC results showed that the corrosion rate of SS is negligible compared to that of CS under all studied conditions. An integrated analysis of the electrochemical and surface and solution analysis results revealed that the galvanic effect has a strong time-dependence. Initially, coupling to SS and/or increasing temperature accelerates the CS oxidation rate. However, it also accelerates the formation and growth of oxides on CS, suppressing the subsequent oxidation of CS. As a result, the increase in the CS corrosion rate due to galvanic coupling diminishes with time.

In Chapter 6, the effect of γ-radiation on the independent corrosion behavior of individual CS, SS 304 and SS 309 and on the galvanic corrosion of the CS-SS (Type 309) couple was investigated. The FIB cut cross-section of the corroded CS surface showed that micro-galvanic corrosion of CS is not significant in both the absence and presence of radiation. In the presence of γ-radiation, the E_{corr} values of the three alloys increase and this increase varies depending on the alloy and the pH. The corrosion behaviours of SS 304 and SS 309 are similar at both pHs, indicating negligible galvanic corrosion of the SS 304-SS 309 couple. For the CS-SS couple, however, the galvanic effect varies with the solution pH. Generally, in a basic environment (pH 10.6), galvanic corrosion of the CS-SS couple is not significant even in the presence of strong oxidants (radiolysis products). In an acidic to near neutral environment (pH 6.0), the galvanic effect is more pronounced. Coupling to SS and irradiation work synergistically at this pH in accelerating the progression of CS corrosion and their combined effects vary with time. Over a short time period (up to 2 h), the effect of galvanic coupling on increasing the corrosion rate of CS is more pronounced than the effect of radiation. As corrosion progresses (up to 20 h), radiation contributes more to the oxide formation due to the involvement of •OH and H_2O_2 in the solution reactions, whereas galvanic coupling contributes more to Fe dissolution. The higher oxidation rate due to galvanic coupling can also accelerate the chemical reaction processes. Over longer time periods (up to 72 h), after more significant oxide layers (consisting mostly of less soluble ferric species) have formed on the electrode surface, the subsequent oxidation of CS can be impeded. Of the four studied cases, the combination of irradiation and coupling to SS cause the most significant acceleration of the progression of CS corrosion.

In Chapter 7, the effects of the SS:CS surface area ratio on the galvanic corrosion of the CS-SS couple under various solution conditions (three different temperatures, the presence and absence of radiation) were investigated. Coupling to SS accelerates the progression of CS corrosion. A higher SS:CS area ratio, higher temperature or the presence of radiation further accelerate the progression of CS corrosion, and their effects on the CS oxidation rate vary with time. Initially, higher SS:CS surface area ratio, higher temperature and the presence of radiation increases the CS oxidation rate. At longer times, however, these factors lead to earlier and faster oxide formation and growth on CS, reducing its subsequent oxidation rate.

We also examined the reduction reaction behaviour for CS and SS and found that the relationship between I_{cpl} and the SS:CS area ratio is not always linear. Even when it is linear, this does not necessarily mean the corrosion dynamics of CS are under cathodic control, as reduction reactions other than oxygen reduction could be involved in the corrosion process (e.g. $Fe^{3+} \rightarrow Fe^{2+}$). CV was also performed in deaerated solutions to study the metal oxidation in a less complicated environment. We found that the anodic peaks of the CV scan coincided with characteristic E_{cpl} values obtained at 80 °C, indicating similar redox process of CS under two different sets of conditions. The CVs and the anodic i-E curves plotted based on the DEC results were compared and the DEC results were fitted using a Koutecky-Levich equation. The fitted parameters obtained will be used for future model development.

8.2 Future Work

The objective of this thesis project was to develop a mechanistic understanding of the aqueous corrosion of the different steels used in the end shield tank assembly and supporting structures in the presence of a continuous flux of γ-radiation. The work presented in this thesis focused mostly on a pH range of near neutral to lightly basic. However, the local pH may be lower than these studied pHs due to the presence of nitric acid produced via humid air radiolysis. Additional studies in a more acidic solution environment are needed. Other factors such as the dissolved oxygen concentration and ionic strength that might be present at the weld region are also worthy of investigation.

The coupons used for galvanic corrosion studies were an electrically connected CS-SS couple which were not in physical contact. In the actual End Shield Cooling assembly, CS is in physical contact with the filler material SS 309. During the welding process, the filler material experiences high temperatures, which often leads to a change in its microstructure, forming a fusion zone and heat-affected zone (HAZ). This would influence the corrosion process in the vicinity of the weld. Therefore, it will also be necessary to test a similarly welded coupon to understand how heat-induced microstructural changes affect the galvanic corrosion of CS and SS.

The long-term goal of this continuing project is to develop a high-fidelity corrosion dynamic model for the independent and galvanically coupled corrosion of steels. The results presented in this thesis will eventually be incorporated into this dynamic model, which is still under development. To achieve this, it will be necessary to formulate individual processes as a function of solution parameters, such as the interfacial electrochemical reactions and mass transport processes.

Appendix A. Curriculum Vitae

Mi Li

Education

PhD Candidate, Chemistry
2015/09-present
The University of Western Ontario, London, Ontario, Canada

B.Sc., Chemistry
2011/09-2015/06
Xiangtan University, Xiangtan, Hunan, China

Work Experience

Research Assistant
2015/09-present
Department of Chemistry, The University of Western Ontario

First-year Laboratory/ Tutorial Teaching Assistant
2015/09-present
Department of Chemistry, The University of Western Ontario

Awards

- The 2020 Roy G. Post Scholarship, Roy G. Post Foundation, Phoenix, Mar. 2020.
- CAMBR Trainee Travel Award, Centre for Advanced Materials and Biomaterials Research (CAMBR), The University of Western Ontario, Dec. 2019.
- The Best Poster Presentation Award-2nd place, NACE SOSS 9th Annual Symposium, The University of Western Ontario, July. 25-26, 2019.
- Graduate Student Book Award by NACE International Foundation, Mar. 2019.
- The Best Oral Presentation Award-1st place, NACE SOSS 7th Annual Symposium, McMaster Automotive Research Centre, July. 19-20, 2017.
- The 1st Place Poster Award, 2016 UNENE R&D Workshop, Waterloo, Dec. 13-14, 2016.

Publications

- D. Guo, **M. Li**, J.M. Joseph, J.C. Wren, A new method for corrosion current measurement: the dual-electrochemical cell (DEC), J. Electrochem. Soc., 167 (2020) 111505.
- **M. Li**, D. Guo, J.M. Joseph, J.C. Wren, Galvanic corrosion of carbon steel and stainless steel couples: effects of γ-radiation and solution environment, WM2020 Conference, Mar. 8-12, 2020, Phoenix, Arizona, USA.
- J.C. Wren, D. Guo, Y. Shin, **M. Li**, Corrosion of carbon steel inside used nuclear fuel containers, WM2019 Conference, Mar 3-7, 2019, Phoenix, Arizona, USA.

- L. Wu, D. Guo, **M. Li**, J.M. Joseph, J.J. Noël, P.G. Keech, J.C. Wren, Inverse crevice corrosion of carbon steel: effect of solution volume to surface area, J. Electrochem. Soc., 164 (2017) C539-C553.
- L. Li, **M. Li**, X. Wang, Q. Wang. Density functional theory study on the "Molecular Taekwondo" process of pyrene-armed calix[4]azacrowns. Comput. Theor. Chem, 1031 (2014) 40.
- Q. Wang, **M. Li**, X.Wang, L. Li. Theoretical study supramolecular chemistry of alkali-metal cations with crown ether derivatized thiophenes. J. Theor. Comput. Chem, 13 (2014) 1450029.

Conference Presentations

- **M. Li**, D. Guo, J.M. Joseph, O. Yong, J.C. Wren, **Talk**, Galvanic Corrosion of Carbon Steel and Stainless Steel Couples: Effects of γ-Radiation and Solution Environment, Waste Management Conference (WM 2020), Phoenix, Arizona, USA, Mar. 8-12, 2020.
- **M. Li**, D. Guo, J.M. Joseph, O. Yong, J.C. Wren, **Poster**, Determination of Corrosion Rate Using Dual Electrochemical Cell Measurement for Galvanic Corrosion System, Waste Management Conference (WM 2020), Phoenix, Arizona, USA, Mar. 8-12, 2020.
- **M. Li**, D. Guo, J.M. Joseph, O. Yong, J.C. Wren, **Talk**, Determination of Corrosion Rate Using Dual Electrochemical Cell Measurement for Galvanic Corrosion System, The University Network of Excellence in Nuclear Engineering (UNENE) R&D Workshop, Toronto, ON, Dec. 16-17, 2019.
- **M. Li**, D. Guo, J.M. Joseph, O. Yong, J.C. Wren, **Poster**, The Dual Electrochemical Cell: A Novel Technique for Corrosion Rate Measurements in Galvanic Systems, The University Network of Excellence in Nuclear Engineering (UNENE) R&D Workshop, Toronto, ON, Dec. 16-17, 2019.
- **M. Li**, D. Guo, J.M. Joseph, O. Yong, J.C. Wren, **Talk**, Determination of Corrosion Rate Using Dual Electrochemical Cell Measurement for Galvanic Corrosion System, NACE SOSS 9th Annual Symposium, the University of Western Ontario, July. 25-26, 2019.
- **M. Li**, D. Guo, J.M. Joseph, O. Yong, J.C. Wren, **Poster**, Determination of Corrosion Rate Using Dual Electrochemical Cell Measurement for Galvanic Corrosion System, NACE SOSS 9th Annual Symposium, the University of Western Ontario, July. 25-26, 2019.
- J.C. Wren, D. Guo, Y. Shin, **M. Li**, **Talk**, Corrosion of Carbon Steel Inside Used Nuclear Fuel Containers, Waste Management Conference (WM 2019), Phoenix, Arizona, USA, Mar. 3-7, 2019.
- D. Guo, Y. Shin, **M. Li**, **Poster**, Non-linear Dynamics of Carbon Steel Corrosion, Waste Management Conference (WM 2019), Phoenix, Arizona, USA, Mar. 3-7, 2019.
- **M. Li**, J.M. Joseph, O. Yong, J.C. Wren, **Poster**, Combined Effects of Solution Parameters and γ-Radiolysis on Corrosion Dynamics of Galvanically-Coupled Dissimilar Metals, The University Network of Excellence in Nuclear Engineering (UNENE) R&D Workshop, Toronto, ON, Jan. 14-15, 2019.
- **M. Li**, J.M. Joseph, O. Yong, J.C. Wren, **Poster**, Combined Effects of Solution

Parameters and γ-Radiolysis on Corrosion Dynamics of Galvanically-Coupled Dissimilar Metals, Gordon Research Conference on Aqueous Corrosion, New London, NH United States, July. 8-13, 2018.

- **M. Li**, J.M. Joseph, O. Yong, J.C. Wren, **Poster**, Combined Effects of Solution Parameters and γ-Radiolysis on Corrosion Dynamics of Galvanically-Coupled Dissimilar Metals, Gordon Research Seminar on Aqueous Corrosion, New London, NH United States, July. 7-8, 2018.
- **M. Li**, J.M. Joseph, O. Yong, J.C. Wren, **Poster**, Galvanic Corrosion of Carbon Steel and Stainless steel, The University Network of Excellence in Nuclear Engineering (UNENE) R&D Workshop, Toronto, ON, Dec. 11-12, 2017.
- **M. Li**, J.M. Joseph, O. Yong, J.C. Wren, **Poster**, The Effect of Radiation on the Kinetics of Corrosion of Carbon Steel-Stainless Steel Welds, NACE SOSS 7th Annual Symposium, McMaster Automotive Research Centre, ON, July. 19-20, 2017.
- **M. Li**, J.M. Joseph, O. Yong, J.C. Wren, **Talk**, The Effect of Radiation on the Kinetics of Corrosion of Carbon Steel-Stainless Steel Welds, NACE SOSS 7th Annual Symposium, McMaster Automotive Research Centre, ON, July. 19-20, 2017.
- **M. Li**, M. Momeni, J.M. Joseph, O. Yong, J.C. Wren, **Talk**, The Effect of Radiation on the Kinetics of Corrosion of Carbon Steel-Stainless Steel Welds, The 100th Canadian Chemistry Conference and Exhibition, Toronto, ON, May. 28-June. 1, 2017.
- **M. Li**, J.M. Joseph, O. Yong, J.C. Wren, **Poster**, The Effect of Radiation on the Kinetics of Corrosion of Dissimilar Metal Welds, The University Network of Excellence in Nuclear Engineering (UNENE) R&D Workshop, Waterloo, ON, Dec. 13-14, 2016.
- **M. Li**, M. Momeni, J.M. Joseph, O. Yong, J.C. Wren, **Poster**, The Effect of Radiation on the Kinetics of Corrosion of Dissimilar Metal Welds, NACE Northern Area Eastern Conference 2016, Toronto, ON, Oct. 30-Nov. 2, 2016.
- **M. Li**, M. Momeni, J.M. Joseph, O. Yong, J.C. Wren, **Poster**, Effect of Environmental Chemistry on the Corrosion of Dissimilar Metal Welds, The 36th Annual CNS Conference and 40th CNS/CNA Student Conference, Toronto, ON, June. 19-22, 2016.
- M. Momeni, R.J. Whyte, **M. Li**, O. Yong and J.C. Wren, **Poster**, Effects of pH and Radiation on Galvanic Corrosion of Stainless Steel-Carbon Steel Welds, The University Network of Excellence in Nuclear Engineering (UNENE) R&D Workshop, Toronto, ON, Dec.15-16, 2015.